

Defect Assessment by Spectral Analysis of Transient Signals

Ph.D. Thesis

Mahabir Prasad

ID No.: 2010REC109



Department of Electronics & Communication Engineering

Malaviya National Institute of Technology, Jaipur

June-2018

Defect Assessment by Spectral Analysis of Transient Signals

Submitted in
fulfillment of the requirements for the degree of
Doctor of Philosophy

by
Mahabir Prasad
ID: 2010REC109

Under supervision of

Dr. P. C. Jha
Scientist, Dept. of Engineering Geophysics, NIRM, KGF, Karnataka

Dr. Shri Gopal Modani
Professor (Retd.), Dept. of ECE, MNIT, Jaipur

Dr. Mool Singh
Professor (Retd.), Dept. of EE, MNIT, Jaipur



**Department of Electronics & Communication Engineering
Malaviya National Institute of Technology, Jaipur
June-2018**

CERTIFICATE

This is to certify that the thesis entitled “*Defect Assessment by Spectral Analysis of Transient Signals*” being submitted by Mahabir Prasad (2010REC109) is a bonafide research work carried out under our supervision and guidance in fulfilment of the requirement for the award of the degree of Doctor of Philosophy in the Department of Electronics & Communication Engineering, Malaviya National Institute of Technology, Jaipur. The matter embodied in this thesis is original and has not been submitted to any other University or Institute for the award of any other degree.

Place: Jaipur

Date:

Dr. Shri Gopal Modani
Professor (Retd.),
Dept. of ECE, MNIT,
Jaipur

Dr. Mool Singh
Professor (Retd.),
Dept. of EE, MNIT,
Jaipur

Dr. P. C. Jha
Scientist, Dept. of
Engineering Geophysics,
NIRM, KGF, Karnataka

DECLARATION

I, Mahabir Prasad, declare that this thesis titled "*Defect Assessment by Spectral Analysis of Transient Signals*" and the work presented in it are my own. I confirm that:

- This work was done wholly or mainly while in candidature for a research degree at this Institute.
- Where any part of this thesis has previously been submitted for a degree or any other qualification at this Institute or any other institution, this has been clearly stated.
- Where I have consulted the published work of others, this is always clearly attributed.
- Where I have quoted from the work of others, the source is always given. With the exception of such quotations, this thesis is entirely my own work.
- I have acknowledged all main sources of help.
- Where the thesis is based on work done by myself jointly with others, I have made clear exactly what was done by others and what I have contributed myself.

Date:

Mahabir Prasad
(2010REC109)

I dedicate this research work to my family for their love, unstinted support and encouragement during the course of this long journey.

To my parents, Shri Bhagwan Singh and late Smt. Surji Devi for their endeavour and inspiration ever since and encouraging me for the pursuit of excellence.

To my Mentors (Gurus) Shri Mohan Godara, Shri Daya Ram Maharia, Sri Ram Saini, Shri Shiv Kumar, Shri Ashok Jhunjunwala, Shri T. N. Ranganathan and Shri P. Radhakrishnan for boosting my morale by motivating me for the sincerity of the work.

ACKNOWLEDGEMENT

My sincere thanks to my wife, Pushpa for her unflinching loyalty, unshakable devotion and encouragement throughout this journey. I also would like to make a mention of my son Aditya and little daughter Tejasvi who cheered my efforts all through and for their tolerance and patience.

I express my sincere gratitude to Professor Shri Gopal Modani and Professor Mool Singh for their willing support during the research work and accepting my candidature to pursue my Doctoral Programme under their aegis and able guidance.

To my conscientious supervisor Dr. P. C. Jha for his creative ideas, guidance, timely encouragement, field visits, sharing of his vast field enriching experience knowledge and technical contributions.

I am grateful to Dr. K. K. Sharma, Dr. Ritu Sharma and Dr. Ghanshyam Singh for their valuable suggestions and review of my research work.

My special thanks go to Assistant Professor Amit Singh for enabling me the use of vibration hardware suit and accompanying me to fruitful field visits.

My thanks also go to Shri Prashant Kulkarni of Microchip and Shri Vinay Thapiyal for their valuable hardware and development tools supports for prototype instrument.

I thankfully acknowledge to fellow research scholars Sanjeev Metya, Sudhir Keshari and Arun Johar for their discussions, reviews of artefacts and unconditional supports.

Special thanks to Shri Rohit Khetan of Bhagwati Marbles, Jaipur and Shri Sankar Singh of Om Srikripa Marbles, Ajmer to allow access in their factories for marble blocks to collect the data.

Special thanks also to Patrick of Swiss Academic Software for providing citations and the reference manager tool “*Citavi*” while preparing the papers and thesis.

To my Guru and Mentor Dr. Ashok Jhunjhunwala for his constant support in my academic pursuit and career, able guidance in and out of the classroom and for the research opportunities he provided me at the Indian Institute of Technology, Madras.

Mahabir Prasad
mahapushpa@yahoo.com

ABSTRACT

One of the major concerns in the dimensional stone industries is the identification of hidden internal defects prior to the processing of the stone block, e.g., cracks, voids, fissures, and joints. The presence of these internal defects results in a low yield of production during slicing and cutting process. These defects generate lots of wastage and eventually ruin the marketing potential of the stone blocks. More often, the stone breaks during slabbing, cladding and polishing operations because of these hidden internal defects. Hence, there is a need to identify such defects in a dimensional stone block, prior to processing so that the yield and quality of production can be improved.

The aim of current research is to develop a simple and easy to use nondestructive testing method to identify internal hidden defects in the dimensional stone blocks prior to slicing and cutting by an ordinary person. The study has focused on the principle of wave propagation through solids in the sonic frequency range to detect the defects in dimensional stone blocks. In the evolved method, a transient stress wave is generated by the impact of a hammer on to the stone block. This sends a transient impulse wave into the stone block. This transmitted signal, after passing through the stone block, is recorded either on adjacent or opposite face. The stone block creates an authentic diagnostic trail on the signal when it passes through the stone block. This diagnostic trail gets reflected in the spectral domain of the recorded signals.

The research is focused on detecting the defects in the stone blocks by experimental methods. The experimental and advanced signal processing techniques were applied on the received transient signals (which passed through stone blocks). In order to make a rigorous detection algorithm, the dimensional stone blocks from different regions were selected for experimental study. Finally, the limitations and validity of various approaches are examined.

First, the role of the impulse hammer's impact and its tip on the spectral characteristic of the received signal studied. It is found that the hammer's impact has minimal or no role in the spectral character of the received signals. Its tip material and diameter play an important role in the band of frequencies injected into a stone block. Based on this study, it is concluded that the response spectrum alone can be used for spectral analysis to determine the intactness of a stone block of 2mX2mX2m size. This made the process of defect identification very simple and cost effective.

For internal defect characterisation, both parametric and nonparametric power spectral density estimation methods were applied to the received transient impulse signals after they passed through the stone blocks. The estimation of power spectral density using Periodogram with rectangular window and Autoregressive Burg methods are found suitable. Further, these power spectral density estimation methods are suitable to implement in the portable low power instruments.

While analysing the power spectral density estimation of response signals, it is observed that there are dispersion and redistribution of energy in the spectral band of the received signal (as compared to the source signal). This redistribution of energy depends on the intactness of the stone block. This information can be used as a potential diagnostic mechanism for defect detection in dimensional stone blocks. This method has an edge over conventional impact-echo and ultrasonic methods on two counts:

- (1) This method has a larger depth of investigation, and
- (2) This does not need the reference measurement from the similar intact material to compare.

By analysis of a large number of data samples on the varieties of dimensional stone blocks, it is observed that reliable signatures of defects in various dimensional stone (marble and granite) blocks are available from 1000 to 3500 Hz in standard block sizes of a cubic meter or more. The spectrum of the transmitted signal is analysed in terms of energy distribution within this range. It is found that whenever, the input impact signal passes through a cracked or defective stone block, the output signal is split in three distinct bands with a conspicuous peak in each of them. By analysis the ratio of energy in these bands, the presence of defect is established by a robust algorithm which is the core of the research outcome. Finally, the accuracy of the proposed method for dimensional stone blocks (marble and granite) is verified.

A proto-type portable battery operated instrument for on-line detection of the presence of defect is developed and used for data collection from the field.

सारांश

संगमरमर पत्थर उद्योग में प्रमुख समस्याओं में से पत्थर के ब्लॉक का उपयोग से पहले छिपे आंतरिक दोषों की पहचान है जैसे दरार, रिक्त स्थान (वोइड्स), छाप (फ्रिसुर्स) और जोड़। इन आंतरिक दोषों की उपस्थिति की वजह से काटने और पटिया बनाने की प्रक्रिया के दौरान उत्पादन कम हो जाता है। इससे बहुत अधिक पत्थर कचरे में परिवर्तित हो जाता है और अंततः पत्थर के ब्लॉकों का बाजार मूल्य कम हो जाता है। अधिकतर, इन छिपे हुए आंतरिक दोषों के कारण पत्थर फर्श (स्लेबिंग), दिवार (क्लेडिंग) पर पटिया लगाने, और इनकी घिशाई (पॉलीशिंग) के दौरान टूटता है। इसलिए, प्रसंस्करण (प्रोसेसिंग) से पहले, संगमरमर पत्थर के ब्लॉक में ऐसे दोषों की पहचान करने की आवश्यकता है ताकि उत्पादन और इसके गुणवत्ता में सुधार किया जा सके।

वर्तमान अनुसंधान का उद्देश्य एक सामान्य व्यक्ति द्वारा काटने और पटिया बनाने से पहले संगमरमर पत्थर के ब्लॉक्स में छिपे आंतरिक दोषों की पहचान करने के लिए एक सरल और आसानी से उपयोग में लेने वाली बिना नुकसान पहुँचाए ब्लॉक्स की परीक्षण विधि का पता लगाना है। संगमरमर पत्थर के ब्लॉक में दोषों का पता लगाने के लिए ध्वनि आवृत्ति रेंज में ठोस पदार्थों के माध्यम से ध्वनिक कंपन संचरित तरंगों के सिद्धांत पर केंद्रित है। विकसित विधि में, पत्थर के ब्लॉक में क्षणिक कंपन तरंग एक हथौड़े की चोट से उत्पन्न करते हैं। यह पत्थर के ब्लॉक में एक क्षणिक कंपन तरंग भेजता है। यह संचरित तरंग पत्थर के ब्लॉक से गुजरने के बाद ब्लॉक के बाजू या विपरीत सतह पर संग्रहित की जाती है। जब कंपन तरंग पत्थर ब्लॉक से गुजरती है तो पत्थर का ब्लॉक एक विश्वसनीय और विशेष नैदानिक लक्षण संचरित कंपन तरंग पर बनाता है। यह नैदानिक लक्षण प्राप्त क्षणिक कंपन तरंगों के आवृत्ति क्षेत्र (स्पेक्ट्रल डोमेन) में परिलक्षित होता है।

यह शोध प्रयोगात्मक विधियों द्वारा पत्थर के ब्लॉक में दोषों का पता लगाने पर केंद्रित है। प्रायोगिक और उन्नत सिग्नल प्रोसेसिंग तकनीकों को प्राप्त क्षणिक कंपन तरंगों पर प्रयुक्त किया गया (जो पत्थर के ब्लॉकों से गुजरने के बाद प्राप्त हुआ)। सटीक पहचान परिशुद्ध विधि (रोबुस्त अल्गोरिथ्म) बनाने के लिए, विभिन्न क्षेत्रों के संगमरमर पत्थर के ब्लॉक

प्रायोगिक अध्ययन के लिए चयन किये। अंत में, विभिन्न तरीकों की सीमाओं और वैधता की जांच की गई।

सबसे पहले, संचरित कंपन संकेत की आवृत्ति स्पेक्ट्रम विशेषताओं पर हथौड़ा और इसके सिर की भूमिका का अध्ययन किया। यह पाया गया है कि प्राप्त कंपन संकेतों के आवृत्ति स्पेक्ट्रम में हथौड़े की भूमिका बहुत कम या बिल्कुल नहीं है। इसके सिर के पदार्थ और आकार पत्थर के ब्लॉक में प्रसारित आवृत्तियों के बैंड में महत्वपूर्ण भूमिका निभाता है। यह निष्कर्ष निकाला है कि पत्थर के ब्लॉक के आंतरिक दोषों की पहचान के लिए अकेले प्राप्त तरंगों के आवृत्ति स्पेक्ट्रम विश्लेषण के लिए इस्तेमाल किया जा सकता है और पत्थर के ब्लॉक की स्थिरता निर्धारित की जा सकती है। इसने दोष पहचान की प्रक्रिया बहुत सरल और कम लागत वाली बना दिया।

आंतरिक दोषों की पहचान के लिए पत्थर के ब्लॉक के अंदर से प्रेषित क्षणिक कंपन संकेतों से प्राप्त संकेतों पर दोनों पैरामेट्रिक और नॉनपारामेट्रिक पावर आवृत्ति घनत्व अनुमान विधियों का इस्तेमाल किया गया। पावर आवृत्ति घनत्व अनुमान पद्धतियाँ “आयताकार विभाजन के साथ पेरीडियोकार्ड” और “ऑटोरेग्रेसिव बर्ग” उपयुक्त पायी गई। इसके अलावा, ये पावर आवृत्ति घनत्व अनुमान पद्धतियाँ पोर्टेबल और कम ऊर्जा वाले उपकरण में अमल में लाने के लिए भी उपयुक्त हैं।

प्राप्त संकेतों की पावर आवृत्ति घनत्व अनुमान का विश्लेषण करते समय यह देखा गया कि प्राप्त संकेतों के आवृत्तियों के बैंड (स्रोत संकेतों की तुलना में) में ऊर्जा का फैलाव-संकुचन और पुनर्वितरण होता है। ऊर्जा का यह फैलाव-संकुचन और पुनर्वितरण पत्थर के ब्लॉक की दोष मुक्त की स्थिति पर निर्भर करता है। संगमरमर पत्थर के ब्लॉक में दोष पहचान के लिए यह जानकारी संभावित नैदानिक तंत्र के रूप में इस्तेमाल की जा सकती है। यह विधि परंपरागत चोट-प्रतिध्वनि और अल्ट्रासोनिक तरीकों से दो मामलों में बेहतर है:

1. यह अधिक गहराई तक जांच कर सकता है, और
2. इसे तुलना करने के लिए समरूप दोष-रहित पत्थर ब्लॉक के संदर्भ माप की आवश्यकता नहीं है।

अंत में, संगमरमर पत्थर के ब्लॉक के लिए प्रस्तावित विधि की सटीकता सत्यापित की गई। संगमरमर पत्थर के ब्लॉकों की विभिन्न किस्मों पर बड़ी संख्या में नमूनों का विश्लेषण करके यह देखा गया कि ब्लॉक में दोषों के विश्वसनीय और विशेष लक्षण क्यूबिक मीटर या अधिक माप के ब्लॉक आकारों में 1000 से 3500 हर्ट्ज तक उपलब्ध हैं।

Table of Contents

CERTIFICATE	i
DECLARATION	iii
ACKNOWLEDGEMENT	vii
ABSTRACT.....	ix
Table of Contents	xv
Table of Figures	xxi
List of Tables	xxv
List of Abbreviations	xxvii
1. Introduction.....	1
1.1 Dimensional Stones	1
1.2 Damage Assessment Needs and Current Status.....	2
1.3 Earlier Research	3
1.4 Gap in Existing Approaches	3
1.5 Research Objectives.....	3
1.6 Innovative Aspects of the Research.....	4
1.7 Restrictions	5
1.8 Outline of the Thesis	5
2. Nondestructive Testing Methods	7
2.1 Visual Inspection	8
2.2 Sounding Bar	9
2.3 Stress Wave Propagation Methods	10
2.3.1 Stress Wave Propagation	11
2.3.1.1 Wave Characteristics.....	12
2.3.1.2 Wave Speed	12
2.3.1.3 Reflection and Refraction	14
2.3.1.4 Attenuation.....	17

2.3.1.5	Diffraction	17
2.3.2	Ultrasonic Pulse Velocity Method	18
2.3.3	Pulse-echo Method	20
2.3.4	Impact-echo Method	21
2.3.4.1	Principle	22
2.3.4.2	Instrumentation.....	24
2.3.4.3	Advantages and Disadvantages of Impact-echo Method	28
2.3.5	Impulse Response Method	30
2.3.5.1	Signal Processing	30
2.3.5.2	Instrumentation.....	31
2.3.6	Resonant Frequency Method.....	31
2.3.6.1	Forced Resonance	31
2.3.6.2	Impact Resonance	33
3.	Transient Signal.....	35
3.1	Introduction	35
3.2	Discrete Fourier Transform.....	35
3.3	Energy of Transient.....	36
3.4	Power Spectral Density Estimation.....	38
3.4.1	Nonparametric Methods.....	38
3.4.1.1	Periodogram Method.....	38
3.4.1.2	Bartlett Method	39
3.4.1.3	Welch Method.....	39
3.4.1.4	Windowing	40
3.4.2	Parametric Methods.....	41
3.4.2.1	Burg Method	41
3.5	The Proposed Method	43
4.	Data Acquisition.....	47

4.1	Introduction.....	47
4.2	Impulse Hammer.....	48
4.3	Piezoelectric Accelerometers.....	51
4.4	Mounting of the Accelerometer.....	54
4.5	Data Acquisition Module.....	55
4.6	Source and Receiver Orientation Setup.....	56
4.7	MATLAB Application ImpulseScope.....	57
4.7.1	Introduction.....	57
4.7.2	Data Acquisition.....	58
4.7.3	Post Processing.....	62
4.7.4	DC Removal and Filtering.....	64
4.7.5	GUI Screens.....	64
4.7.6	Conclusion.....	67
4.8	Prototype Instrument.....	67
4.8.1	Introduction.....	67
4.8.2	Block Diagram of Prototype Instrument.....	67
4.8.3	Control Module.....	69
4.8.4	Acquisition Module.....	69
4.8.5	Storage Module.....	71
4.8.6	Graphical User Interface Module.....	72
4.8.7	Power Module.....	72
4.8.8	Conclusion.....	73
4.9	Data Collection.....	73
4.9.1	Capturing Impulse Response Data.....	74
4.9.2	Measurement of P-wave Velocity.....	75
4.9.3	Measurement of Density.....	78
4.10	Dimensional Stone Details.....	78

4.10.1	Defects in Marble Blocks	79
4.10.2	Sizes of Dimensional Stone Block	80
5.	Data Analysis	81
5.1	Repeatability.....	81
5.2	Signal Duration	83
5.3	Preliminary Spectral Analysis	83
5.3.1	Role of Impulse Hammer in Spectral Analysis	83
5.3.2	Identification of Usable Frequency Band.....	86
5.3.3	Suitable Power Spectral Density Estimation Methods.....	88
5.3.4	Defect Characterization of a Dimensional Stone Block.....	91
5.4	Experimental Results of Various Dimensional Stone Blocks	95
5.4.1	Dimensional Stone Block 1 (Adanga Marble, Banswara)	95
5.4.2	Dimensional Stone Block 2 (Arana Marble, Raj Samand)	98
5.4.3	Dimensional Stone Block 3 (Supreme Black Granite, Thirumalai).....	100
5.4.4	Dimensional Stone Block 4 (Super White Marble, Vietnam).....	102
6.	Conclusions and Future Work.....	105
6.1	Contributions of Dissertation	105
6.2	Future Work and Concluding Remarks.....	106
7.	Annexures.....	107
7.1	Plots of Power Spectral Density Estimation by Burg Method	107
7.1.1	Dimensional Stone Block 1 (Adanga Marble, Banswara)	107
7.1.2	Dimensional Stone Block 2 (Arana Marble, Raj Samand)	111
7.1.3	Dimensional Stone Block 3 (Supreme Black Granite, Thirumalai).....	117
7.1.4	Dimensional Stone Block 4 (Super White Marble, Vietnam).....	119
7.2	Mechanical Systems	123
7.2.1	Single Degree of Freedom System.....	123
7.2.1.1	Transfer Function	123

7.2.1.2	Frequency Response Function	124
7.2.1.3	Determining the Natural Frequency and Damping	126
7.2.2	Mechanical Wave Filter	126
7.2.3	Mechanical Resonance.....	128
8.	References.....	131
	List of Publications	137
	Brief CV	139

Table of Figures

Figure 1: Propagation of stress waves by an impact source on a surface of object	12
Figure 2: The behaviour of P-wave incident on an interface between two dissimilar media.....	15
Figure 3: Schematic diagram of ultrasonic pulse velocity test circuit	19
Figure 4: Pulse velocity measurement configurations	19
Figure 5: A schematic block diagram of pulse-echo and pitch-catch methods.....	21
Figure 6: Principle of the impact-echo method.....	22
Figure 7: Schematic of Impact-echo testing	23
Figure 8: Example of Impact-echo measurement with results.....	23
Figure 9: Impactor kit for the impact-echo method	26
Figure 10: Normalised amplitude spectrum of a force-time function with the shape of a half cycle sine curve	27
Figure 11: ASTM C 1383 for measuring the thickness of slab-like concrete structures	28
Figure 12: Idealised mobility plot for a pile	31
Figure 13: Schematic of the instrument for forced resonance test.....	32
Figure 14: Schematic of apparatus of impact resonance test	33
Figure 15: Typical transient signal from a Dimensional stone block	36
Figure 16: Examples of transient functions and their Fourier transforms	37
Figure 17: Window function's time and frequency domain plots	40
Figure 18: Flowchart of PSD estimation by the Burg method.....	43
Figure 19: schematic diagram of measurement setup with NI 9234.....	47
Figure 20: Photograph of data collection setup from a marble block in the field.....	48
Figure 21: Parameters of impulse hammer with force sensor.....	49
Figure 22: A typical response curve of the accelerometer.....	52
Figure 23: Different mounting methods and their effects on the higher frequency range of an accelerometer	55

Figure 24: Typical pickup sensor and impulse hammer impact points on a dimensional stone block.....	57
Figure 25: Start-up flowchart of MATLAB application.	60
Figure 26: Data capturing flow diagram of MATLAB application.	61
Figure 27: Trigger Mechanism of data capturing from marble blocks.	62
Figure 28: Post processing diagram of data in MATLAB application.	63
Figure 29: Data acquisition parameter setting screen	64
Figure 30: Data session capturing and storing screen	65
Figure 31: Data analysis screen (FFT and PSD)	66
Figure 32: Frequency response function screen.....	66
Figure 33: Block diagram of prototype instrument.....	68
Figure 34: Photograph of prototype instrument	68
Figure 35: Flow chart of single impact data collection.....	71
Figure 36: Acceleration time histories of the impact hammer impulse on dimensional stone blocks.....	75
Figure 37: A schematic diagram for P-wave velocity measurement using direct transmission method.....	77
Figure 38: Time histories and amplitude spectra of instrumented hammer hits.	82
Figure 39: Time histories and amplitude spectra of the receiver with the same source and receiver points.	82
Figure 40: Hammer hit duration on the surface of the marble block with stainless steel tip.....	83
Figure 41: A normalised plot of the source and received signal	84
Figure 42: Frequency response function vs Standard spectral response	85
Figure 43: PSD plots of response signals in different marble blocks	87
Figure 44: Estimation of PSDs of the marble block response signal	91
Figure 45: Frequency and Power spectral density estimation spectrum	92
Figure 46: Face photos, hammer and accelerometer locations for stone block 1 (Adanga marble).....	96

Figure 47: Face photos, hammer and accelerometer locations for stone block 2 (Arana marble).	98
Figure 48: Face photos, hammer and accelerometer location for stone block 3 (Supreme black granite).	101
Figure 49: Face photos, hammer and accelerometer location for stone block 4 (Vietnam marble).	102
Figure 50: PSD plot showing peak locations and crack detection logic for signal 1 to 6 of marble block 1.	107
Figure 51: PSD plot showing peak locations and crack detection logic for signal 7 to 12 of marble block 1	108
Figure 52: PSD plot showing peak locations and crack detection logic for signal 13 to 18 of marble block 1.	109
Figure 53: PSD plot showing peak locations and crack detection logic for signal 19 to 24 of marble block 1.	110
Figure 54: PSD plot showing peak locations and crack detection logic for signal 1 to 6 of marble block 2.	111
Figure 55: PSD plot showing peak locations and crack detection logic for signal 7 to 12 of marble block 2	112
Figure 56: PSD plot showing peak locations and crack detection logic for signal 13 to 18 of marble block 2.	113
Figure 57: PSD plot showing peak locations and crack detection logic for signal 19 to 24 of marble block 2.	114
Figure 58: PSD plot showing peak locations and crack detection logic for signal 25 to 30 of marble block 2.	115
Figure 59: PSD plot showing peak locations and crack detection logic for signal 31 to 33 of marble block 2.	116
Figure 60: PSD plot showing peak locations and crack detection logic for signal 1 to 6 of stone block 3.	117
Figure 61: PSD plot showing peak locations and crack detection logic for signal 7 to 8 of stone block 3	118
Figure 62: PSD plot showing peak locations and crack detection logic for signal 1 to 6 of stone block 4.	119
Figure 63: PSD plot showing peak locations and crack detection logic for signal 7 to 12 of stone block 4	120

Figure 64: PSD plot showing peak locations and crack detection logic for signal 13 to 18 of stone block 4.	121
Figure 65: PSD plot showing peak locations and crack detection logic for signal 19 to 20 of stone block 4.	122
Figure 66: A mechanical system with a single degree of freedom	123
Figure 67: Frequency response function plots	125
Figure 68: SDOF system, magnitude vs frequency for different damping ratios	125
Figure 69: Typical magnitude vs frequency responses of filters	128
Figure 70: Mechanical resonance in a mechanical oscillatory system.....	129

List of Tables

Table 1: Parameters of body and surface waves created by point impact on a solid...	12
Table 2: Specific acoustic impedances and P-wave speed of selected materials.....	16
Table 3: Relation between impactor size, useful frequency, and measurable thickness	25
Table 4: Window function parameters.....	41
Table 5: Specifications of the Impulse hammer Model 086C03	50
Table 6: Roundhead point hammer with fibreglass handle	51
Table 7: Specifications of the accelerometer Model 352C03	53
Table 8: Specifications of the accelerometer Model 2224C	54
Table 9: Specifications of the Data acquisition module NI 9234	56
Table 10: Orientation of source and receiver on a dimensional stone block.....	56
Table 11: Specifications of acquisition module.....	70
Table 12: Power consumption test results of the device in different modes.....	73
Table 13: P-wave velocity in marble block specimens.....	77
Table 14: Density of marble block specimens	78
Table 15: Execution time of Different PSD algorithm	89
Table 16: Peak frequencies, amplitudes, and PSD of bands for the intact and cracked medium	93
Table 17: Prominent diagnostic pattern in the spectral character	94
Table 18: Tabulation of various data for stone block 1 (Adanga marble).	97
Table 19: Tabulation of various data for stone block 2 (Arana marble).....	99
Table 20: Tabulation of various data for stone block 3 (Supreme black granite).....	101
Table 21: Tabulation of various data for stone block 4 (Super white marble).	103
Table 22: Mechanical counterpart elements of solids to electrical elements.....	127

List of Abbreviations

<i>Acronym</i>	<i>Definition</i>
AC	Alternating Current
ADC	Analog to digital converter
AIC	Akaike Information Criterion
AR	Auto Regression
ASTM	American Standard Testing Method
B&K	Bruel & Kjaer
BEM	Boundary Element Method
BNC	Bayonet Neil Councilman
COG	Chip on Glass
CPU	Computing Processing Unit
CRC	Cyclic Redundancy Check
DAQ	Data Acquisition
DFT	Discrete Fourier transform
DOF	Degree of Freedom
EEPROM	Electrically Erasable Programmable Read-Only Memory
ESD	Energy Spectral Density
FAT16	File Allocation Table 16 bits
FEM	Finite Element Method
FFT	Fast Fourier Transform
FPE	Final Prediction Error
FRF	Frequency Response Function
GB	Gigabyte
GBWP	Gain Band Width Product
GPR	Ground Penetrating Radar
GUI	Graphical User Interface
I2C	Inter-Integrated Circuit
ICP	Integrated Circuit Piezoelectric Circuit
ICs	Integrated Circuits
IDFT	Inverse DFT
IE	Impact Echo
IEPE	Integrated Electronic Piezoelectric
KB	Kilobyte
L-C	Inductance Capacitance
LCD	Liquid Crystal Display
MATLAB	Matrix Laboratory
MCU	Microcontroller Controller Unit
MHz	Mega Hertz
MNIT	Malaviya National Institute of Technology

<i>Acronym</i>	<i>Definition</i>
NDE	Non-destructive Evaluation
NDT	Non-destructive Testing
NI	National Instruments
NIRM	National Institute of Rock Mechanics
PCB	Printed Circuit Board
PSD	Power Spectral Density
PSDE	Power Spectral Density Estimation
PSE	Power Spectral Estimations
RAM	Random Access Memory
SAW	Surface Acoustic Wave Filter
SDOF	Single Degree of Freedom
SEA	Statistical Experimental Analysis
SPI	Serial Peripheral Interface
STFT	Short Time-Frequency Transform
TISAR	Testing and Investigation using Seismo-Acoustic Resonance
USB	Universal Serial Bus

Chapter 1: Introduction

1. Introduction

1.1 Dimensional Stones

Since the Stone Age, the natural stones have played a key role in the history of mankind starting from hunting tools and safety covers in caves to modern day constructions and buildings because of their easy availability and longer durability. Even today, the natural stones adorn the legacies of businesses, societies, nations, and kingdoms. In olden days, they were used primarily as building blocks, but with the development of new manufacturing and processing techniques since last 50 years, it has become commercially feasible to use them for cladding, flooring and other industrial applications.

The natural and dimensional stones have deep imprints on the architectural and cultural heritage of the Indian history. World famous monuments, temples, forts, and palaces like Sanchi Stupa, Konark Sun temple, Taj Mahal, the rock-cut Khajuraho temple and Elephanta caves have been constructed from locally available stones. Besides these, all major archaeological excavations have revealed exquisitely carved sculptures and carvings on the stones [1]. Even today, the use of natural stone in architecture is seen at places like the President and Parliament Houses, Supreme Court and other government buildings.

India possesses a wide spectrum of dimensional stones that include granite, marble, sandstone, limestone, slate, and quartzite, which is abundant throughout the length and breadth of the country. With an estimated resource of about 1690 million cubic meters, comprising over 160 shades of dimension stones and granites, India accounts for about 20% of the world resources in this category. There are roughly 300 varieties of dimensional stones which are traded in the world market and nearly half of them originate from the India [2]. The industrial production of dimensional stone includes flooring and cladding slabs, tiles, chips, tombstones, sculptures, monuments, kerbs, cubes, pebbles and garden stones.

Now, it is being increasingly used in homes because of its beautiful finishes, shades, low cost and easy availability in the market due to latest production

technologies. In recent years, natural stone materials have seen exponential growth in use for external cladding and internal flooring in houses and public buildings. Because of these new areas of uses, there is demand from the construction professionals as well as house owners to know the mechanical properties and durability of stones being used.

1.2 Damage Assessment Needs and Current Status

The commercial journey of dimensional stones starts from the extraction of sizable blocks in cubical shapes from the native deposits to slicing for use as slabs, cladding or tiles in varieties of applications. Therefore, the success of stone industries depends upon safe extraction of blocks from native deposits and its mechanised slicing. For commercial viability, it is important that the mined-out stone blocks should not have any inherent or induced defects like intrusions, fissures, cracks, natural joints, and damage. These defects in mined-out blocks lead to further damage during slicing, adversely affect their market potential and restrict their application areas.

As a rough estimate, almost 30% of the mined out dimensional stone blocks get rejected during slicing and slabbing because of the presence of hidden defects or cracks found. These defects are either natural or man-made during the quarrying or processing. These defects, affect the optical and mechanical properties, e.g., impurities give undesired colours in dimensional stones and gemstones. Some of the properties like aesthetically appealing colour patterns add to the market value of these stones.

The prior detection of inherent defects will help in the quality assessment of these blocks so that they are not subjected to further costly and time-consuming exercise of slicing or slabbing and polishing. At present, there are no commercially viable tools to detect such hidden defects within standard blocks of one meter cube or larger. All earlier research work have focused on reflected wave measurements, which restricts the depth of detection to just 2-4 inches [3–7]. While considering the development of a reliable tool for such defect detection, it should be borne in mind that the basic requirement of defect detection is that the prescribed method should clearly identify intact and defective one even by a layman.

1.3 Earlier Research

Most research and developments in the past several decades are focused on the development of in-situ NDT tools for flaw detection in concrete and man-made structures only. A wide range of physical parameters is measured by the ultrasonic pulse and other techniques for homogeneous or heterogeneous materials, e.g., near-surface, larger sized (> 10 cm) volumetric defects and cracks in concrete structures [7].

Most of the reported studies for dimensional stone blocks have been done in the area of restoration of ancient monuments and buildings only. Very little work is done in the area of defect detection in dimensional stone blocks at mining stage or before being subjected to gang saw so as to reduce wastage and improve the quality of production.

1.4 Gap in Existing Approaches

Presently available methods are more suitable for research labs and scientific communities for specific applications. The interpretation of the results of these methods is not easy and needs experts for analysis. They cannot be used by an ordinary person on a day-to-day basis at the gang saw. Lack of prior knowledge and reference measurements create further bottlenecks in the current methods. Hence, there is a need for identifying and characterising these defects in-situ by a credible scientific method for everyday use by industries.

1.5 Research Objectives

The objective of this research work is to go beyond the limits of the presently used impact-echo method and develop a new method for defect detection in dimensional stone blocks for use by an ordinary person at the mining or gang saw operation stage. This will lead to improvement in the quality of facades production, reduction of the wastage of material and decrease the cost of production. The aim of this research work is:

- Development of a suitable algorithm for identification of hidden cracks, flaws, and fissures in virgin dimensional stone blocks with or without a reference line (index for intact stone).

- Implementation of the developed algorithm in a proto-type portable battery operated instrument for on-line detection of the presense of defect.

1.6 Innovative Aspects of the Research

Some innovative theoretical aspects of the work, which needs special mention, are as under:

- The range of frequency so generated by hammer depends on three factors - (a) duration of impact/contact and (ii) material of the hammer tip and (c) surface area of contact. A short duration impact or a sharp hammer tip (smaller surface area) generates higher frequency signals compared to a blunt head and longer contact time. Similarly a soft hammer tip/head generates a lower frequency signal compared to a harder tip. The importance of hammer force's spectra has been evaluated for defect assessment for dimensional stone blocks. It is shown that the hammer's impact plays its role only in the generation of a signal in the suitable frequency band.
- It has been proved that response spectra have sufficient media signatures to detect the internal cracks or defects in dimensional stone blocks. This made damage detection simpler without using a reference of the intact stone block.
- A simple algorithm for spectral dispersion and redistribution has been identified and explained as the main discriminant for the presence of inherent flaw or defect.
- Shifting of the natural frequency of stone blocks because of the presence of inherent defects has been explained with case studies. Optimal frequency filtering for the usable band has been applied during signal conditioning stage itself.
- A simple, battery operated prototype device is designed for use in the field. With damage detection algorithm built-in, this makes the defect assessment simpler and can even be used by a layman.

1.7 Restrictions

In the present work, the investigation has been restricted to actual experimental study on the dimensional stone blocks. Hence the simulation analysis and other aspects are not covered, viz.

- This research work does not deal with model testing techniques and finite element methods because it focuses on the experimental methods for damage detection,
- For the same reason, the numerical algorithms for model identification and optimisation are not used nor discussed.
- This thesis does not deal with damage detection on a microscopic scale rather it discusses the same at a macro level in the actual stone block.

1.8 Outline of the Thesis

The thesis is organised into six chapters which begins with an Introduction in Chapter 1, a brief description of the current non-destructive testing method is made in Chapter 2 which describes the acoustic wave propagation methods currently being used in concrete structures and natural stones. The theoretical aspect of acoustic stress wave propagation through the solids is discussed here and changes of the attendant wave properties of these waves because of the medium interface have been explained.

Chapter 3 discusses the mechanical vibration of the system because of an impulse force wherein a single degree of freedom system for free vibration mode is explained. It also describes the natural frequency of the mechanical system and parameters affecting it. The mechanical filters are explained and compared with the equivalent electrical one. The defects in the material correlated to the properties of mechanical wave filters. The proposed method is discussed and applicable suitable signal processing techniques are also explained in this chapter.

Chapter 4 describes in detail the data acquisition technique, sensor and their mounting methods, and tools used in the field for dimensional stone as well as the common measurement problems. The MATLAB application “ImpulseScope” which is used for data collection and analysis and the prototype instrument designed for field trials have been discussed. The P-wave velocity in marble and the density of marble is

calculated as a correlation exercise. The common types of dimensional stone defects are also discussed.

Chapter 5 describes the data analysis of dimensional stone blocks. The consistency of readings has been verified and transient signal duration has been calculated. The importance of source spectra, selection of source frequencies for dimensional stone blocks explained. The useful signature energy band has been identified to be used in defect detection. The defect signatures have been identified in the spectral domain for which applicable signal processing tools are described in detail. Classification of defects in dimensional stone has been done based on the selected algorithm using contemporary signal processing tools.

In chapter 6, the results, key findings, and suggestion for further research are discussed.

Lastly, plots of PSD estimation by Burg method for various stone blocks are given in the first part of Annexure. In the second part of Annexure, the mechanical vibrations in systems are discussed in details, single degree of freedom systems and its behaviour during free oscillations, mechanical filters and resonance of the system.

Chapter 2: Nondestructive Testing Methods

2. Nondestructive Testing Methods

This chapter presents a review of the literature on the current nondestructive testing (NDT) methods for concrete and stones. The processes and methodologies of mechanical stress wave propagation methods are reviewed in detail. The major in-situ nondestructive methods are classified based on their working principles used [8], [9, p. 6], and described in the following sections.

The NDT methods are the procedures to test, evaluate and inspect the components, materials or assemblies for defects or differences in characteristics without damaging them. The NDT methods are easier and more economical than destructive ones because they do not need a sample extraction and preparation; they also offer unique ways to assess the material properties of historic and architectural buildings, where the possibility of extracting core samples is limited or not possible.

While destructive methods damage the materials during the testing and applied to the limited number of items to understand their performances or material behaviour under different stress conditions. These destructive methods are used to determine and verify the physical properties of materials, e.g., ductility, impact resistance, yield, and fatigue strength.

The NDT methods are simple one druminess of the sound result of striking the surface of the object with a hammer or visual inspection to judge the quality of the material to complicated ones where the sonic or ultrasonic signals pass through the material. When using simple methods like hammering or visual inspection, defects are noticed, it is a waste of time in applying the more advanced and complicated methods to verify the interiors. Major NDT evaluation methods are the visual inspection, sounding bar, dye penetrant, ultrasonic, and elastic wave propagation methods. The elastic wave propagation methods and some other NDT methods' basic principle, applications, advantages, and limitations are described. There are numbers of other NDT methods available and are used in special applications only, e.g., acoustic emission, neutron radiography, thermal imaging, infrared, tomography, microwave, strain sensing, holography, and radioisotope gauges.

The nondestructive methods are used in production and allied industries and in-situ evaluation to verify reliability and integrity of machinery and systems, to regulate the process, lowering the cost, and to improve the quality of products. In building and monuments areas, in-situ evaluation is done to ensure that these places are safe for the public to continue to use.

It is essential that NDT testing individuals ought to have the learning of different NDT methods available for testing a parameter and choose the best one from them as per the current state of the material or system. Utilisation of various techniques for assessing a single parameter builds the certainty and gives the confidence in the results.

A good NDT method should have following features:

- Sensitive to small cracks, voids, and anomalies in the object
- Simple to use for the intended application and easy result interpretation
- Low cost and preferably portable battery operated one for field application

All the NDT methods have limitations and thus, it is not possible to obtain 100% accuracy from every method. There are factors that affect the reliability of the method as follows:

- Defect location and its orientation
- Test object and structure geometry
- Selection of correct technique and its use
- Weather, and material property
- Test environment and time constraints.

2.1 Visual Inspection

In NDT methods, visual inspection is most widely used, easiest and oldest technique that provides valuable information to the well-trained eyes. It is the first step in the NDT inspection and provides lots of information that may lead to the identification of the reason of noticed distress and form the basis of further investigations. A detailed visual examination makes it possible to pinpoint the critical

areas of the object that need further testing using advanced methods. Visual inspection applies to most surfaces and its effectiveness increases by cleaning the surfaces prior to the examination for scale, dust, or loose paint and wide knowledge of the inspector.

The trained eyes of an inspector often identify information that is sometimes difficult to detect by hi-tech instruments. It needs a light source, either the sun or artificial one and the surface to examine. Sometimes, mechanical and optical aids may be necessary to perform visual inspections. The object is observed either directly by eyes or optical instruments for detection of surface defects, joints, and the object conformances to applicable standards [10]. This method helps to detect surface cracks, visual features related to workmanship, material damage, and signs of distress, e.g., disintegration, spalling, pop-outs, the impact of weather, change of colour, and surface disfigures. It is the most cost-effective method for assessing the structural conditions conjunction with other scientific methods in interpreting the results of the latter.

The benefits of the trained eyes are depicted by Sherlock Holmes when he said: “I see no more than you, but I have trained myself to notice what I see” [11, p. 44]. The accuracy and reliability of both routine and in-depth visual inspections could be improved through training of the types of discontinuities that should be identified and the methods that would frequently allow identification to be possible [12]. This method also depends on the inspector’s experience and his vision, and lighting conditions.

2.2 Sounding Bar

The sounding bar or tapping technique is one of the most common nondestructive methods based on travelling of acoustic stress wave in solids. Even today, an ordinary person uses it in multiple applications to identify the cracks, e.g., chinaware, glassware, or mudware in streets while buying or selling the items.

The most common types of audible inspections at the industrial level are chain dragging, hammer sounding, and listening under load. Chain dragging is normally used in large concrete surface areas, such as bridge decks, while hammer sounding can be used on several materials in random locations. Listening under load can be used to detect many problems, including loose bars in steel grid decks, settled areas, and bad expansion joints. The inspector listens to thuds, pops, vibrations, or other

unusual sounds when traffic is passing to help identify and locate problems and their locations. This method relies on the experience of the inspector to identify the change in sound from one region to another in the same material.

In this method, the object's surface is hit by a hammer or bar and listening to the sound by ears or special microphones to detect the presence of subsurface internal defects, cracks or delaminations and it is supported by the visual inspection [13] and other NDT methods. When an object is hit by a hammer or bar, delaminated or crack regions produce drum like, dull or hollow sound compared to good regions which produce a sharp ringing sound [13], [14], [7, pp. 14-16], [15]. Sometimes, electrical powered tapping device and sonic receiver are used instead of the hammer and bar. For large structures, like bridge decks, dams or roads, dragging a chain over the surface is considered. The operator notes dull or hollow sounds accomplish the detection of delaminations in them. It is subjective to the experience and hearing ability of the person and surrounding noise and limited to detecting subsurface defects only [13], [15], [16]. The extent of any noted defects is subject to the inspector's interpretation of the tonal differences in the produced sound.

Despite these inherent limitations, it is widely used method after the visual inspection method to detect surface and near-surface defects in the material. This method may be used in conjunction with other methods of determining the conditions of objects and can be used to determine the specific areas of delamination requiring repair [15].

2.3 Stress Wave Propagation Methods

In these methods, analysis of materials is based on acoustic wave travelling through the material under study using suitable wave source and captured by the receiver after travelling through or reflecting from the surface of the medium. The analysis of these received signals gives internal information of the material or structure through which they pass or reflect. The properties of the material and interested information plays a vital role to select suitable method, induced signal frequency, instrumentation, and criteria for interpreting the results [17]. The degree of homogeneity of material decides the frequency of used signal and its energy level, e.g., ultrasonic frequency above 500 kHz with the narrow band is suitable with directional transmit and receiving probes for metal objects. In a metallic object, because of the homogeneous

nature, the metallic objects allow the signals to travel without measurable reflections, refractions or mode conversion unless the presence of anomalies. For non-homogeneous objects like concretes, structures and natural stone need wideband low frequency signals (usually less than 5 kHz) with higher energy to compensate the absorption, reflection, diffraction and other media properties [17].

The important property of these techniques is that internal properties of test object have a significant impact on the travelling of these acoustic waves when they pass through them. These techniques differ by stress wave source and its frequencies, the testing configuration, the measured response and the signal processing methods applied to them. These differences make each method unique to the particular application area [7, 14-2]. To understand these methods, theoretical formulation of stress wave propagation is explained below.

2.3.1 Stress Wave Propagation

When stress waves are generated by an impulse source, i.e., hammer with ball pointed head or transducer to the surface of the object, these waves travel into the medium as body waves called P-, compressional or longitudinal waves and S-, transverse or shear waves, and surface wave called R- or Rayleigh waves. The S- and P-waves travels into the object as the hemispherical wavefronts and get reflected, refracted and diffracted due to internal flaws, i.e., cracks, voids, joints and boundaries of the structure and the R-wave travels on the surface of the object [9], [18], [19], [20], [21], [3]. The motion, direction and velocity relationship of these waves are shown in Figure 1.

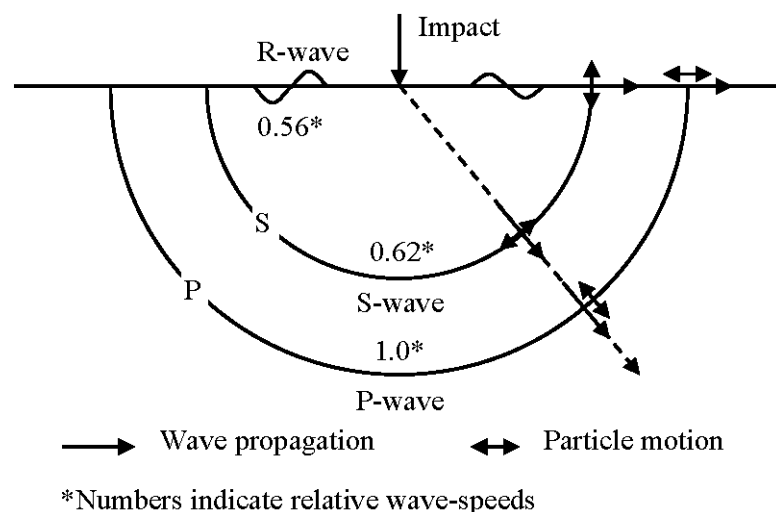


Figure 1: Propagation of stress waves by an impact source on a surface of object [3].

2.3.1.1 Wave Characteristics

When a solid surface is impacted on a face by a point source, the vibration travels away from the impact point as body and surface waves explained in Figure 1. The P-waves, the result of the compressional stress propagates at a faster speed than others and at any point, the particles oscillate into the direction of travelling in the radius drawn from the impact source to the point of observation.

The S-wave due to shearing stress travels at a lower speed than P-waves and at any point, the particles oscillate normal to the direction of travel. The R-waves move at the lowest speed and their particle motions are more complex. The properties of body and surface waves are summarised in Table 1. The major part of the vibration energy is available in the R-waves as shown in Table 1.

Table 1: Parameters of body and surface waves created by point impact on a solid [22].

Wave type	Particle motion direction	Wave speed*	Relative wave speed for $\nu = 0.2$	Energy content, %
P-waves	In parallel of propagation	$C_P = \sqrt{\frac{E(1-\nu)}{\rho(1+\nu)(1-2\nu)}}$	1	7
S-waves	Perpendicular of propagation	$C_S = \sqrt{\frac{E}{2\rho(1+\nu)}}$	0.62	36
R-waves	Retrograde elliptical	$C_R = C_S \frac{0.87+1.12\nu}{1+\nu}$	0.56	67

* E = Young's modulus of elasticity; ν = Poisson's ratio; ρ = density

2.3.1.2 Wave Speed

In acoustic wave propagation methods, the stress wave of a finite short duration either induced by blow of the hammer or ultrasonic transducers and the resultant vibrations travel through the object as an impulse. The travelling of these impulse waves through nonhomogeneous bounded solids, such as stone blocks and concrete structures and relationship of physical properties of the material to wave speed is governed by the principle of wave transmission in infinite, elastic and isotropic media [21]. In isotropic and homogeneous materials, the properties such as density of the material and the velocity of waves are the same at every location in the material,

whereas in anisotropic materials the velocities might be different in different directions because of sedimentation forming process [9].

In the infinite elastic solids, the speed of the P-wave, C_P , Young's Modulus of Elasticity, E , Poisson's ratio, ν and the density, ρ , has the following relation [21]:

$$C_P = \sqrt{\frac{KE}{\rho}} \quad (1)$$

where $K = (1-\nu)/((1+\nu)(1-2\nu))$

within a narrow range of K , a variation of E and ρ have a significant effect on velocity than variation in ν [7].

The equation (1) shows a very useful relation that the speed of elastic waves in a solid depends on its physical and internal properties instead of elastic waves.

For cylindrical bodies, e.g., beams or piles, the speed of P-wave does not depend on Poisson's ratio provided the diameter of the rod is much less than the wavelength of the travelling wave and it is named, the bar wave speed, C_B , as given below [21]:

$$C_B = \sqrt{\frac{E}{\rho}} \quad (2)$$

The S-wave speed, C_S , in an infinite elastic solid is given as [21]:

$$C_S = \sqrt{\frac{E}{2\rho(1+\nu)}} \quad (3)$$

R-waves speed, C_R , is given by [21]:

$$C_R = \frac{0.87 + 1.12\nu}{1 + \nu} C_S \quad (4)$$

From equation (1) to (4), indicates that once the speed of P-waves is estimated in any medium, other speeds can be calculated mathematically. Because of the higher speed of P-wave compared to others, they can be recognised without interference from other waves.

2.3.1.3 Reflection and Refraction

When a transient generated by a pointed impact on the surface of a solid passes through, it encounters change in elastic properties or composition of material, known as a change in acoustic impedance, the part of the incidence energy gets reflected back in primary medium, remaining passes into the next medium (refraction) [8], [21].

The reflection and refraction mechanism of elastic wavefronts at the boundary are analogous to light rays and follows Snell's law [21]. The angle of refraction, β , depends on the incidence angle, θ , and wave speed ratio, C_2/C_1 , in the two mediums and is governed by Snell's law below [21]:

$$\sin\beta = \frac{C_2}{C_1} \sin\theta \quad (5)$$

The reflection of the P-waves from the interface boundary gives to rise a phenomenon known as mode conversion and depends on the angle of incidence on the interface. The incident P-wave partially reflects back, and remaining refracts as P- and S-waves and this mode conversion of reflection and refraction also follow the Snell's law as well, though the wavefronts are elliptical instead of spherical in nature [8]. This reflection of wave fronts and mode conversion continues from interferences, surface, and bottom of objects and successive amplitude and energy attenuate till the wave fronts loose the whole energies. The S-wave travel is slower than a P-wave, their reflection, θ_s , and refraction angles, β_s , are smaller than the angles of the P-waves and are shown in Figure 2(B) [21].

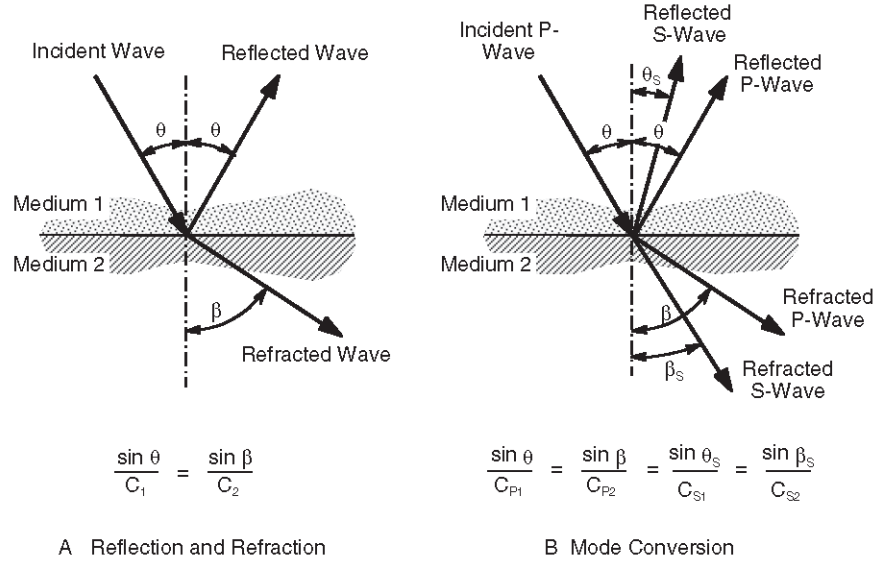


Figure 2: The behaviour of P-wave incident on an interface between two dissimilar media: (a) reflection and refraction; (b) mode conversion (adopted from [21]).

The amplitude and energy of reflected waves depend on the change in acoustic impedance of the medium at the interface, the incidence angle, the interface distance from the wave source, and the wave attenuation during travel [21]. The amplitude of reflected wave is highest when the incidence angle is normal to the interface. The specific acoustic impedance, Z , of a medium depends on density, ρ , and velocity of P- and S-wave and is given by [21]:

$$Z = \rho C_p \quad (6)$$

The equation (6) is applicable to S-waves also when these waves are used to determine specific acoustic impedance. By using equations (1) and (6), the specific acoustic impedance, Z , of a medium can be defined as:

$$Z = \sqrt{\frac{\rho E(1 - \nu)}{(1 + \nu)(1 - 2\nu)}} \quad (7)$$

For a small value of Poisson's ratio, ν , equation (7) can write as [21]:

$$Z = \sqrt{\rho E} \quad (8)$$

The specific acoustic impedances of P-waves in different materials are shown in Table 2 [21].

Table 2: Specific acoustic impedances and P-wave speed of selected materials.

Material	Density(kg/m ³)	P-Wave Speed(m/s)	Specific Acoustic Impedance (kg/m ² .s)
Air	1.205	343	0.413
Concrete*	2300	3000–4500	6.9–10.4 x 10 ⁶
Granite	2750	5500–6100	15.1–16.8 x 10 ⁶
Limestone	2690	2800–7000	7.5–18.8 x 10 ⁶
Marble	2650	3700–6900	9.8–18.3 x 10 ⁶
Quartzite	2620	5600–6100	14.7–16.0 x 10 ⁶
Soil	1400-2150	200–2000	0.28–4.3 x 10 ⁶
Steel	7850	5940	46.6 x 10 ⁶
Water	1000	1480	1.48 x 10 ⁶

*The density of concrete depends on the mixture ratios, the relative densities of the mixture elements, and moisture content. The specified density is a typical value for normal density.

The reflected, A_R , to the incident, A_I , the wave amplitude ratio is defined as reflection coefficient of the interface. It depends on the acoustic impedances of the medium of the interfaces and for a normal angle of incidence, it is given as [8], [21]:

$$R_C = A_R/A_I = \frac{Z_2 - Z_1}{Z_2 + Z_1} \quad (9)$$

Where R_C is the reflection coefficient for normal incidence, Z_1 is the acoustic impedance of medium 1 and Z_2 is the acoustic impedance of medium 2.

The equation (9) shows that when Z_1 and Z_2 are not equal, the energy gets reflected as well transmitted. If the acoustic impedances of both mediums are equal, no reflection or very little reflection occurs. For incident angle other than normal, it depends on the incidence angle which applies to plane waves incident on plane boundaries [21], [23].

In earlier discussions, it is shown that reflection and refraction in solids occur at the interface of two dissimilar media. This same condition holds true for defects in solids. These properties of stress wavefronts are used to detect flaws such as cracks, voids, and discontinuities using stress wave propagation methods [21].

The ability of acoustic stress wave propagation techniques to identify defects depends on the frequencies of the wave used and the defect size in the object. As a thumb rule, detectable the defect size must be close to or bigger than the wavelengths of waves used. The relation between wave speed, v , wavelength, λ , and frequency, f , is given as [21]:

$$v = \lambda.f \quad (10)$$

In equation (10), the wave speed, v of acoustic waves depends on the material properties through which they pass. That means source frequencies of waves need to select based on detectable sizes of flaws in the object. This relation controls the selection of the frequency of the source and penetration depth in the medium [7, 8-2].

The level of inhomogeneity depends upon the wavelength utilised for the examinations. When the wavelength is many times larger than the characteristic dimensions of the inhomogeneity in the material, it interacts as a homogeneous material to the waves. Contrarily, when the wavelength is many times smaller than the characteristic dimension of the inhomogeneity, it interacts as an inhomogeneous material to the waves and the waves will be dispersed in all the directions [9].

2.3.1.4 Attenuation

When the acoustic stress waves travel through the solids, their amplitude attenuates with path length because of the divergence, scattering, and absorption. The amplitude of spherical waves attenuates the inverse of the distance, r , from the source due to divergence [24]. The geometrical attenuation $A(r)$ of P- and S-waves given by following formula [25, pp. 90-91]:

$$A(r) \propto 1/r \quad (11)$$

and the wave energy, E , is the inverse of the square of the distance from the source as [24], [25, pp. 90-91]:

$$E(r) = 1/r^2 \quad (12)$$

In the investigations, waves with low-frequency used to reduce the attenuation because of scattering, but low frequencies reduce the penetration ability of the waves to small defects due to scattering. It limits the size of flaws that can be detected using ultrasonic stress wave propagation methods [21].

2.3.1.5 Diffraction

When an incident wave encounters the sharp edge of a discontinuity or interfaces like a slit, diffraction of waves occurs. It is like as twisting of waves around the edges of an obstacle in the region of the geometrical shadow of the obstacle. This characteristic behaviour of diffraction is explained as the interference of waves

according to Huygens–Fresnel principle. This behaviour is shown when the wavefronts meet with an obstacle or a slit of comparable size to their wavelengths. A similar effect also occurs when an elastic wave propagates through a medium with varying specific acoustic impedance. The waves generated by diffraction are also spherical and follow the Snell’s rule for reflection and refraction [8].

2.3.2 Ultrasonic Pulse Velocity Method

It is used to detect internal defects as well as deterioration resulting from the environment, freezing and thawing with time in the structures [7]. It is based on the idea that velocity of P-waves travelling through a medium relies upon the elastic and density properties given as shown in equation (1). In this method, the ultrasonic wave burst injected into the surface of the test object with the help of an electro-acoustical transducer. This pulse generates wideband stress waves and propagates in the object as body and surface waves. The body waves undergo multiple reflections and refractions at the interfaces of the different material phases within the object as well as from the boundaries of the object. The first wave to reach the receiving transducer is the P-wave because of the high speed compared to others in solids. The ultrasonic waves pass through the test object from the transmitter to receiving transducer and its travel time, T is measured as shown in Figure 3. By knowing the distance, L , between these two transducer points, the velocity of the P-wave wave is calculated as [11]:

$$v = \frac{L}{T} \quad (13)$$

A schematic diagram of P-wave velocity measurement is shown in Figure 3 and further details of the method are given in ASTM Test Method C597 [26].

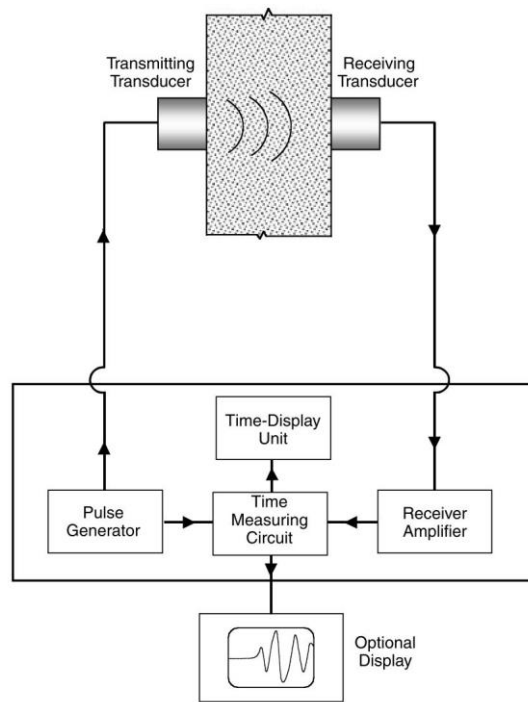


Figure 3: Schematic diagram of ultrasonic pulse velocity test circuit [7, 8-3].

Figure 4 shows the possible locations of both the transducers on the surface of the object under test for measurement of pulse velocity. The direct transmission method is preferable because maximum energy of the pulse is received by receiving transducer due to the P-waves, from the transmitter travel in the normal direction to the transducer face [7]. It needs both faces of media that are not possible in all the cases. The semi-direct can also be used quite satisfactorily provided both transducers are not too far apart. The indirect transmission method is not preferable because of the amplitude of the received signal is significantly lower than other methods [7, 8-4-8-5].

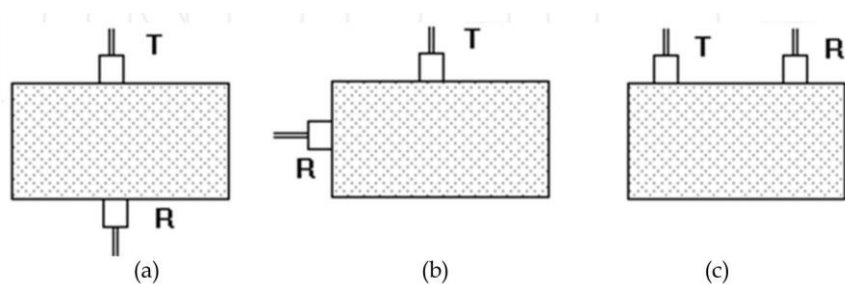


Figure 4: Pulse velocity measurement configurations [7, 8-2, 27]. (a) Direct method. (b) Semi-direct method. (c) Indirect or surface method.

This method is also useful to measure the thickness of plate-like object based on the time taken for pulses to reflect off the back wall of the plate [28, p. 14].

The direct transmission is the best arrangement to use for the NDT because of its known possible path length through the test object. Because of this, once the arrival time of the first wave is measured, there is no need of analysis and distinguish of complex wave frequencies and their reflections. It is successfully used to verify the uniformity, detection of flaws, and the depth of surface cracks of the object. A propagating ultrasonic wave finds a path around the flaws, resulting in amplitude attenuation and an increase in the arrival time of the signal to the receiver [29].

2.3.3 Pulse-echo Method

In the pulse echo method, an ultrasonic transmitter used to inject a known frequency of pulses into an available surface of the test object. This pulse travels into the test object and gets reflected and refracted because of internal defects in an object such as flaws, voids, interfaces, and boundaries.

The reflected wave or echo because of internal defects of the object is recorded at the transmitting surface of the object by either the same transmitter acting as both receiver and transmitter (true pulse-echo) or by a separate receiver located nearby the transmitter (pitch-catch) [21]. In practice, when the transmitter and receiver are two separate units, they are fixed in a single assembly to make sure that the distance between them is always constant. This distance must be as small as possible to minimise the error in the calculated depth of reflecting interface and to have maximum reflected signal from the interface. The pitch-catch arrangement provides flexibility in the selection of transducers, heavily damped for transmitter (narrow pulse) and lightly damped for the receiver. Figure 5 describes these two types of pulse-echo methods. The transmitted and received pulses are recorded either by an oscilloscope or data acquisition module with a computer. These recorded pulses are shown in the upper area of Figure 5. The time, Δt between the start of the transmitted pulse to start of receiving pulse is measured (round-trip or up-down travel time) using amplitude-time plots as shown in Figure 5. With the help of wave speed in object material and travel time in the object, the depth of the reflecting interface (defects or boundaries) from the transmitting surface is determined as [21]:

$$T = \frac{\Delta t \cdot C_p}{2} \quad (14)$$

Where T is the depth of reflecting media from the transmitter and C_p is the P-wave speed in an object's material.

The equation (14) is approximate for a pitch-catch system and applicable only if the distance between the transmitting and receiving transducer is small [21].

The pulse-echo method is successfully used in the metal inspection. It is also tried for concrete and pavements. However, it is not much of success because of the heterogeneous nature of the concrete, and pavements compared to metals and limited to measuring the thickness of thin slabs, pavements, and walls where the material is more uniform [21]. The presence of paste-aggregate interfaces, steel reinforcement and air voids in concrete structures results in the diffraction or multiple echoes of high-frequency waves used in pulse-echo method render the results meaningless and hide the real defects [14].

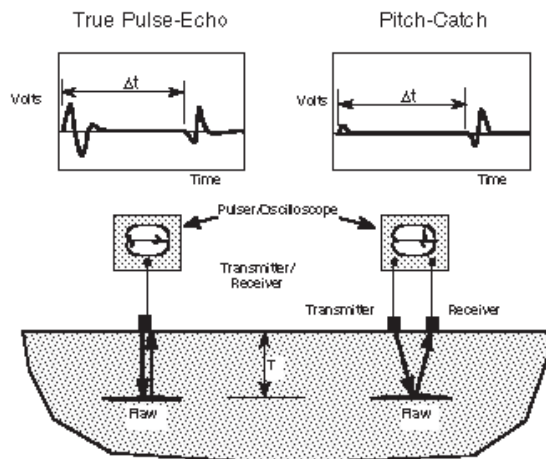


Figure 5: A schematic block diagram of pulse-echo and pitch-catch methods (Adopted from reference [21]).

2.3.4 Impact-echo Method

The ultrasonic pulse-echo methods are not suitable evaluation solutions for inhomogeneous and heterogeneous materials because of high-frequency used in these methods. The high-frequency stress waves cannot penetrate far in these materials and have the problem of wave diffraction because of low wavelength. To overcome the limitations imposed by high frequencies for inhomogeneous and heterogeneous materials, low-frequency stress waves are needed [7]. The transmitting transducers to generate the low frequencies are not feasible because of their bulky size and other

design problems. To address the problems of transmitting transducers and diffraction of waves in inhomogeneous and heterogeneous materials, Sansalone and Carino [30] developed a testing method for the concrete structures called the impact-echo in the 1980s.

2.3.4.1 Principle

In this method, the stress waves are injected into the test object on an accessible surface by a hammer or steel ball impact instead of an ultrasonic transmitter as done in ultrasonic methods. The application of mechanical impactor provides a much simpler way to introduce a much higher amount of energy pulses than by an ultrasonic transmitter. This impact generates a short-duration transient of a wideband frequency spectrum and the upper limit of frequency depends on the contact time of hammer or ball to the object surface and stiffness of the object under impact. The stress waves go through the process of reflection, refraction, and mode conversion because of internal defects if any and boundaries of the object. This process of multiple reflections between the impacted surface and opposite surface or any internal defects creates periodic reflections or resonance. It continues till whole energy of the mechanical impact gets dissipated [31]. The working principle and measurement of the impact-echo method are shown in Figure 6.

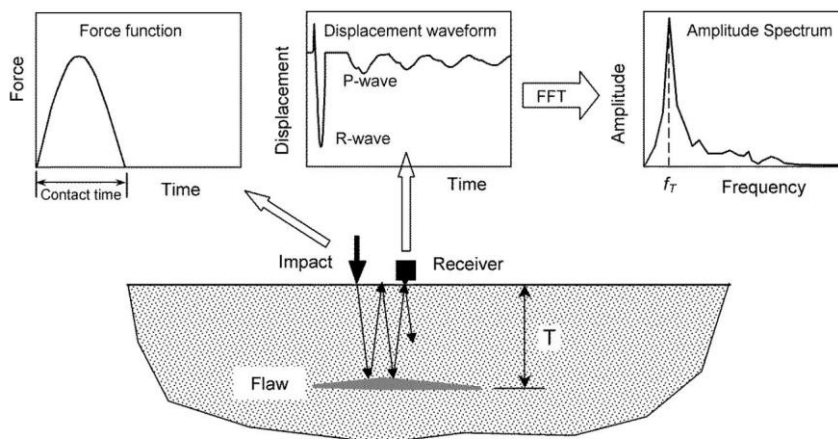


Figure 6: Principle of the impact-echo method [22].

The displacement generated by reflected waves on the impacted surface is captured by a broadband receiver (displacement or acceleration) with the help of the data acquisition system as shown in Figure 7. The receiver is placed close to impact point and the reflected waveforms are dominated by the displacement caused by P-waves

because of the radiation pattern of P- and S- waves [30], [4]. The depth, T of internal flaws or a boundary of impact surface is measured using below formula:

$$T = C_{PP}/2f \quad (15)$$

where C_{PP} is the velocity of P-wave in the object measured by the indirect method (Impact-echo), and f is dominant peak frequency in the amplitude spectrum.

The relation between C_{PP} and C_P (equation (1)) for P-waves in a large solid is defined as [21].

$$C_{PP} = 0.96C_P \quad (16)$$

The velocity of P-waves is measured separately through a portion of the specimen with known thickness, by the indirect method. In practice, it is difficult to measure accurately the travel time from the time domain displacement waveform and this problem is solved using frequency domain analysis. The field measurement method in the impact-echo method is shown in Figure 7. The measurement results with numerical values are explained in Figure 8.

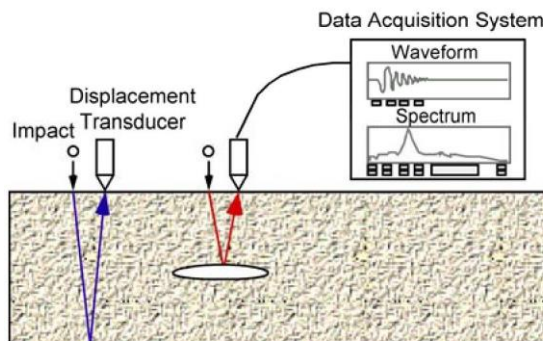


Figure 7: Schematic of Impact-echo testing[32].

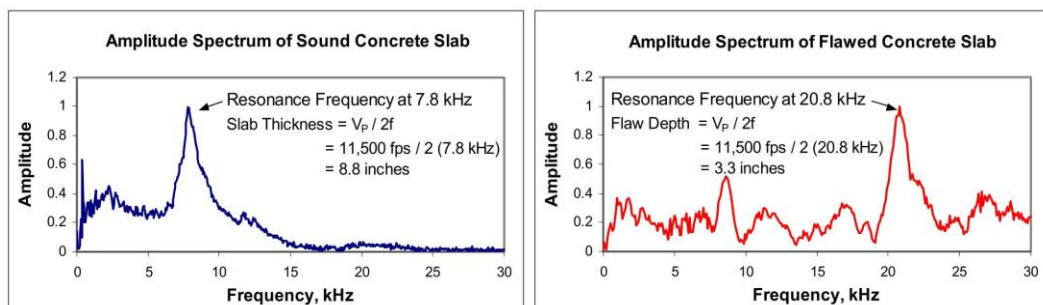


Figure 8: Example of Impact-echo measurement with results [32].

The success depends on the proper selection of an impactor (tip size of impact point) with suitable contact time for an object [21], i.e. depth of object and its material. The impactor with the smallest possible contact time (<10 msec) and a sharp contact tip, produces a better discerning signal. The uncertainty in P-wave velocity and resonance frequency at the given point affects the accuracy of thickness measurements [31]. The size and depth of detected internal cracks depend on the wavelength of signals employed, i.e., the material of the impactor, its contact time with the surface of an object and stiffness of the objects. The major benefits of this method are that it does not require physical access to both sides of the object and need one measuring transducer.

In this method, the selection of the frequency peaks is problematic when there are multiple nearby peaks in the spectrum. This problem can be solved by either selecting the threshold of the amplitude or choosing a suitable impactor for an intended objective of the study. The expected reflected frequency should have maximum energy in the induced pulse to get a desirable quality of the data and ease of interpretation of results [33].

2.3.4.2 Instrumentation

The impact-echo test system has three main elements: an impact source, receiving transducer, and a data acquisition hardware with a suitable software suite to data capture, processing, and management [7]. An impact source is a most critical element and needs to be careful while selecting it.

2.3.4.2.1 Impact Source

In the impact-echo method, the impact sources are of various sizes of small steel ball bearings with metallic flexible spring rod as shown in Figure 9. The material, shape, and size of the impact source control the frequencies of the waveform get injected into the test object. Sansalone and Street [11] gave a relation between the maximum frequency, f_{max} in kHz for a steel ball bearing and its diameter D in mm:

$$f_{max} = \frac{291}{D} \quad (17)$$

While selecting suitable impactor, the diameter of the ball varies until a clear single dominant frequency peak is obtained from a good area of the object. It is the reflected

signal from the opposite face boundary of the source surface and gives the thickness or depth information of the material being tested [11]. The standard impactor kit for the impact-echo test has ten spherical impactors; sizes vary from 3 mm to 20 mm in diameter. With the help of equation (17) and approximate P-wave velocity of 4200m/sec in concrete, the useful frequency maximum range and measurable thickness of concrete objects for available various impactors are shown in Table 3. The relation between contact time (t_D) and ball diameter (D) is given by [22]:

$$t_D(\text{in microsecond}) = 4.3D(\text{in mm}) \quad (18)$$

Table 3: Relation between impactor size, useful frequency, and measurable thickness [14].

	Diameter (mm)	Maximum useful frequency (kHz), equation (17)	Minimum detectable thickness (cm), equation (15)
1	3	97	2.1
2	4	73	2.8
3	5	58	3.5
4	6.5	45	4.5
5	8	36	5.6
6	10	29	7.0
7	11.5	25	8.1
8	13	22	9.2
9	16.5	18	11.2
10	20	15	13.4

The latest impactors are spring-loaded and each impact can be repeated having the same wide range of frequencies and energy and are shown in Figure 9.



Figure 9: Impactor kit for the impact-echo method, containing impactors on springs connected to plastic cylinders and rubber couplings. The housing has a rubber ring resting against the surface. (Model Spider DOC-210N, taken from Germann Instruments A/S, www.germann.org)

2.3.4.2.2 Impact Duration

The force-time history of an impactor can be approximated as a half-cycle sine curve and mathematically defined as [22]:

$$F(t) = F_{max} \cdot \sin\left(\frac{\pi t}{t_D}\right) \quad (19)$$

$$F = 0, \text{ for } t > t_D$$

The shape of the force amplitude spectrum of the equation (19) is shown in Figure 10. An approximate estimate of the maximum frequency induced is the inverse of the contact duration of impactor to the surface of object [11]:

$$f_{max} = 1/t_D \quad (20)$$

The optimal results can be achieved by exciting the surface of the object at the resonant frequency related to the thickness of the object. As the contact duration decreases, the useable frequency range increases, but the amplitude of receiver signal decreases because of attenuation [14].

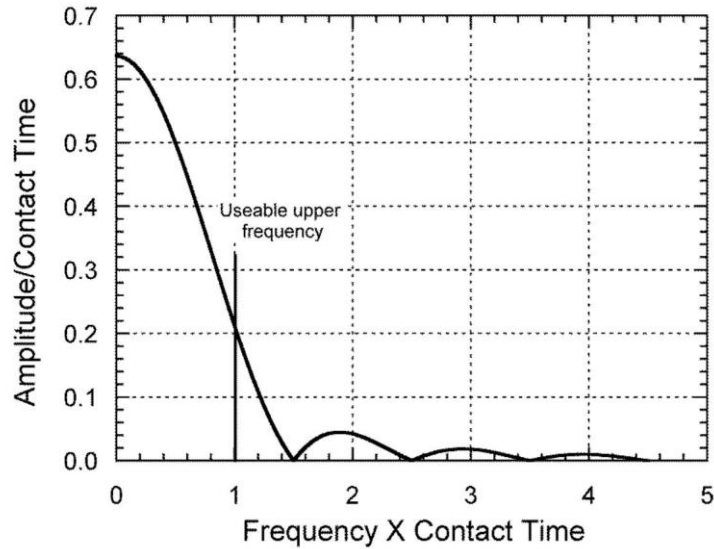


Figure 10: Normalised amplitude spectrum of a force-time function with the shape of a half cycle sine curve [22].

2.3.4.2.3 Source to Receiver Distance

Based on the studies conducted at the Cornell University by Sansalone and others, it found that the best results for impact-echo are obtained when H (distance between impact source and receiver) / T (depth, the top to the bottom surface) ratio is between 0.2 to 0.5. The resulting P-wave arrival will be sharp, clear and the reflected signals are simple and free of complications from R-wave and S-wave reflections [22]. When the receiver is too far from the impact source point, the captured waveform includes the reflected P-wave and the effect of the reflected S-wave also [22].

2.3.4.2.4 Receiving Transducer

Two types of receiving transducers are used in impact-echo method viz. i) acceleration type and ii) displacement, but later has difficulties in availability. Whatever type of transducer used, it must be wideband to capture the frequency range from DC to 2-3 times of the upper limit of selected frequency for the study.

2.3.4.2.5 Data Acquisition System

The data acquisition system is a computer with the data acquisition hardware module and software. It has provision to interface two receiver transducers and software suit for signal processing of captured signals. The system has provision for optimal selection of sampling frequencies which depends on the thickness of the test object. The higher sampling rate is more useful for testing of relatively thin objects.

2.3.4.2.6 P-wave Velocity Measurement

The prerequisite requirement of the impact-echo method is knowledge of P-wave velocity in the material under test and its thickness frequency. ASTM Test Method C1383 [20] has two parts. Procedure A, as described in Figure 11 (A) is used to measure the velocity of the P-wave in the test object by measuring the travel time of the P-wave between two receivers for a known distance between them. Procedure B described in Figure 11 (B) is used to calculate the thickness frequency (dominant amplitude frequency in amplitude spectrum, i.e. frequency used to calculate thickness of object) with the help of the impact-echo and the thickness of the object is determined using the measured velocity of the P-wave and thickness frequency using the equation (15). The calculated thickness has an uncertainty within 3% of the real thickness and it is because of the sampling interval errors in Procedure A and the time duration of the captured signal in Procedure B [7, pp. 14-18].

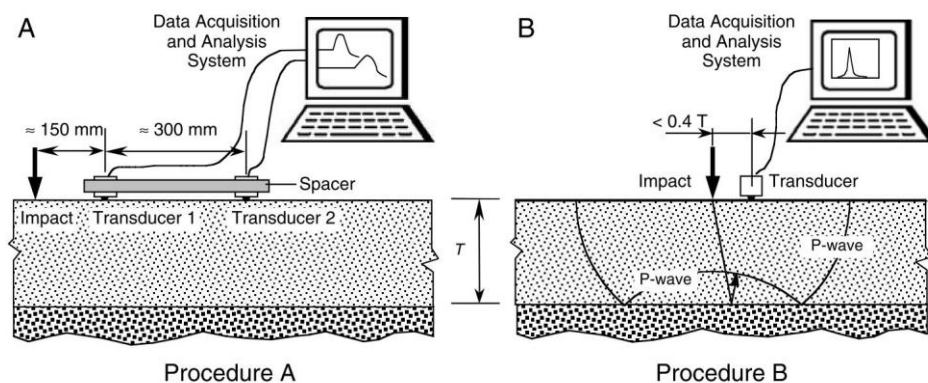


Figure 11: ASTM C 1383 for measuring the thickness of slab-like concrete structures: (A) procedure to determine P-wave speed, and (B) procedure to determine the thickness frequency [7, pp. 14-19].

2.3.4.3 Advantages and Disadvantages of Impact-echo Method

The major advantage is data interpretation in the frequency domain, identification of peak frequencies and requirement of a single surface of the object under test. By knowing the peak frequency and velocity of P-wave in the object, the thickness of object and depth of internal flaws can be detected easily. It is important to realise that the response will not only consist of reflections from voids and delaminations but also include reflections from any location where there is a change in material. Essentially, impact-echo is a system that detects a change in mechanical properties that can be

further analysed to give the depth at which the change of material interface is located [34]. Below are summarised advantages [35]:

- Can detect delamination at very early stage.
- Can detect debonding of layers, like concrete type overlays.
- Fast data analysis with respect to delamination characterization.
- Reliable and repeatable when conducted properly by an experienced operator.

Although impact-echo can successfully detect internal defects, there are some apparent disadvantages also. It is a localised testing method, and testing a large bridge deck takes many resources and time. Therefore, IE is typically used as a tool for reassurance by using it with other methods. The impact-echo does have the ability to show the existence and depth of a defect, however, it is difficult to classify the characteristics of the material that produces the reflections. For example, it cannot differentiate between responses because of air voids, reinforcing steel or large aggregate easily. Another disadvantage of IE is the sensitivity of the results based on the receiver contact with the concrete surface. Inadequate contact will give inaccurate and false measurements. There are difficulties in the ability to receive reliable data in such cases [34]. There are other limitations also as described below [35]:

- Moderate to significant expertise and training required for equipment setup and data collection, processing, and interpretation.
- Slow data collection using traditional single probe equipment; requires a lane closure.
- Requires a dense test grid to accurately define the boundaries of delaminated areas, adding to the test duration.
- More complicated to evaluate the condition of overlaid bridge decks; cannot assess the condition of the deck in areas where the overlay is debonded.

2.3.5 Impulse Response Method

The acoustic wave propagation principle of the impulse response method [36] is same as the impact-echo method. An acoustic stress wave pulse is induced by the hammering of an instrumented hammer with force sensor on the surface of an object under test. A nearby receiver transducer to the impact point captures the vibration of the surface because of the mechanical hammering. The signals from the force sensor and receiver transducer are captured using data acquisition module and processed by a dedicated analyser or computer with suitable software. It is different from impact-echo on two counts: force-acceleration-time recording and signal processing method used. The major use of this method is reported in integrity testing of piles [21] and model validation in labs.

2.3.5.1 Signal Processing

In the impulse response method, the impact force-time and its transient response (velocity or acceleration) of the test object are recorded. These time histories of force and response signals with the help of FFT algorithm are converted into the frequency domain. The ratio of response (output) to force (input) is calculated and it is called frequency response function (FRF). The FRF depicts the structural characteristics, and its shape and properties depend on the material, its geometry, and the existence of flaws in it [7]. The FRF is given as:

$$H(\omega) = V(\omega) / F(\omega) \quad (21)$$

Where, $V(\omega)$ and $F(\omega)$ are FT of Response, $v(t)$ and impulse force, $f(t)$ respectively.

To improve the results in the field, multiple impact data collected from a point (3 to 5 times) and averaging of them are done. Based on parameter measurement of structural response, i.e., velocity, acceleration, or displacement, $H(\omega)$ in equation (21), called mobility, accelerate or compliance respectively. The peaks in the mobility plot occur at the resonant frequencies of the structure. The dynamic stiffness and depth of the structure are calculated using the mobility plot. Figure 12 shows an idealised mobility plot for a pile for displaying parameters and their calculations. The difference between two adjacent peaks of resonance frequency Δf , P-wave velocity in pile C_b , and length of pile, L are related by [7]:

$$L = \frac{C_b}{2\Delta f} \quad (22)$$

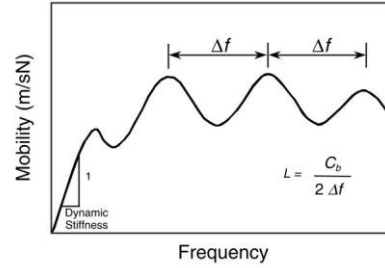


Figure 12: Idealised mobility plot for a pile. (adopted from [7, pp. 14-21])

2.3.5.2 Instrumentation

The impulse response method consists of an instrumented hammer with force sensor as a source, a geophone or an accelerometer as a receiver, and a multi-channel signal analyser or laptop with data acquisition module and processing software capabilities to capture, process the data and calculations of FRFs [7, pp. 14-21].

2.3.6 Resonant Frequency Method

When a solid structure is struck by a force, it vibrates at its natural frequencies. These natural frequencies of structure depend mainly on the density, ρ , and dynamic modulus of elasticity, E of material. The dynamic modulus of elasticity of an object is calculated from the fundamental longitudinal frequency, N_l by [37]:

$$E = 4L^2\rho N_l^2 \quad (23)$$

Where, L = the specimen's length.

The equation (23) is also applicable to inhomogeneous solids when the size of the object is larger than the size of its constituents. Equation (23) shows that the dynamic modulus of elasticity of a structure has relation with its natural frequency. Therefore, by measuring the changes in the natural frequencies of the system, the degradation of the system can be found [37]. That means the shift in resonant frequencies can be inferring changes in the integrity of the system.

2.3.6.1 Forced Resonance

In 1938, the first time the resonant frequency used to infer mechanical integrity of solids by Powers [37]. Later, this method has been refined by Hornibrook, Thomson, Obert, and Duvall, and Stanton particular uses of a vibrating force for excitation of specimens. The resonance occurred when the vibrations have the highest amplitude

while the driving through variable force frequency. This driving force frequency at which highest vibration amplitude occurs is called resonance frequency of the specimen and the phenomena called forced resonance.

The forced resonance method is explained in ASTM test method C215 [37] for concrete as shown in Figure 13. This method has two sections: the mechanical vibration generator and a sensor that senses these vibrations in the specimen. The amplified output of the variable audio frequency generator is fed to the driver to convert electrical signals to mechanical vibrations. These mechanical vibrations in the test object are measured by a piezoelectric transducer and converted these mechanical vibrations into voltage signals. These voltage signals are amplified and fed to an Oscilloscope or similar device which shows the frequency of the signal and its amplitude. In operation, the frequency of driver oscillator is varied and maximum amplitude and its frequency is noted from the Oscilloscope. This is resonance frequency which is little smaller than the fundamental frequency of the specimen. To identify the fundamental frequency rightly, skill and experience are needed because of multiple resonance frequencies may occur corresponding to the modes of vibration. The dynamic modulus of elasticity, the shear modulus of elasticity, and the dynamic Poisson's ratio of the object can be determined as per ASTM C215 method.

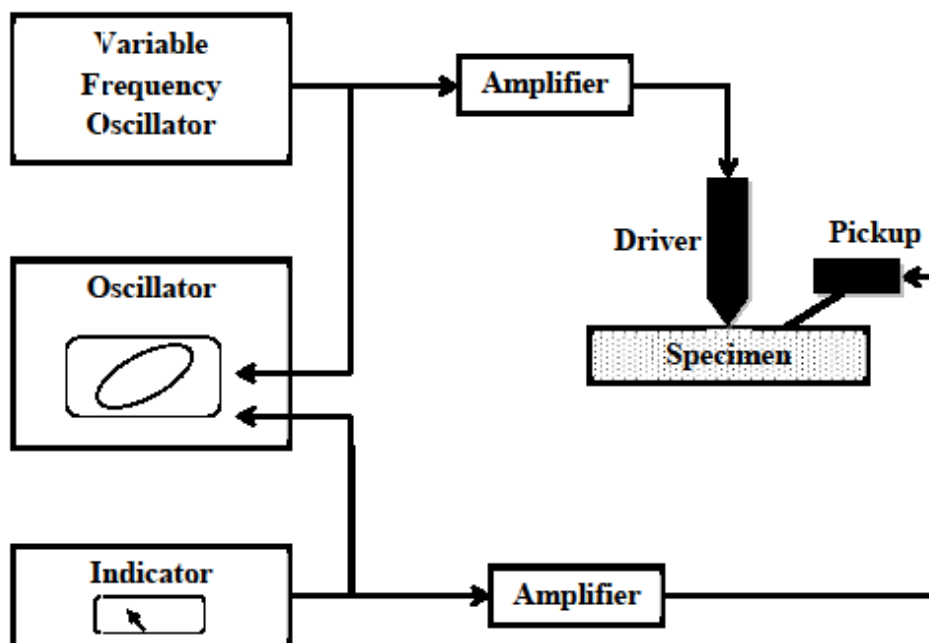


Figure 13: Schematic of the instrument for forced resonance test [37].

2.3.6.2 Impact Resonance

Another technique for calculating fundamental frequencies has been proposed by Gaidis and Rosenberg, as an alternate option of the forced resonance method. In this technique, the object is impacted by a small hammer and hence it is called an impact resonance method. The impact causes the object to vibrate at its natural frequencies. The vibration response is measured by an accelerometer mounted on the specimen as shown in Figure 14. The amplitude spectrum of vibration is captured using spectrum analyser that determines frequency components using FFT. The frequencies of major peaks in amplitude spectrum are resonance frequencies of the specimen. The advantage of this method compared to forced resonance is that it does not need a variable frequency oscillator and driver to vibrate the object which increases the speed of testing. The impact resonance method was adopted by ASTM in 1991 as an alternative procedure [37]. The damping of specimen causes free vibrations to decrease amplitude with time. It creates a difference between resonance and natural frequency of specimen. The resonance frequency is always lower than the natural frequency because of damping of the specimen. The resonance methods have a limitation because of the limited size of the specimen, its boundary conditions, and properties, shape factors in the equations of modulus calculations [37].

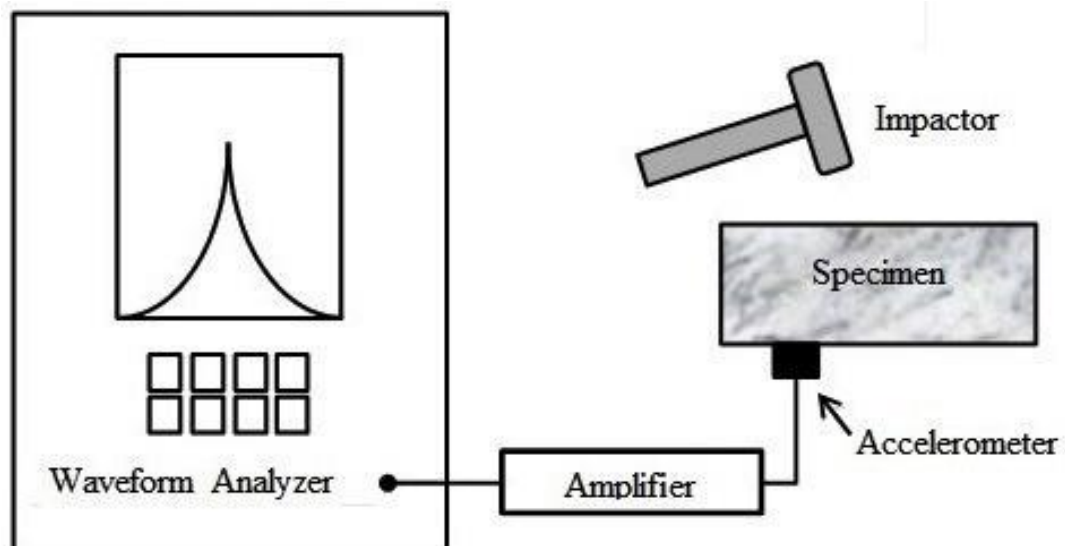


Figure 14: Schematic of apparatus of impact resonance test [37].

Chapter 3: Transient Signal

3. Transient Signal

3.1 Introduction

In simple terms, signals which last for a very short period of time are referred to as “Transient Signals”. Classical examples of such signals include switch bounce, the Shock wave generated from an impact test, Seismic Signals. Going by this definition a transient signal is limited in duration and dies exponential after a while. These signals are usually deterministic in nature and are broadband with continuous frequency spectra. Mathematically a *transient signal* has an *infinite* number of sinusoids Fourier expansion. Therefore, transient signals are better analysed by their energy spectra. It is very difficult to analyse a transient signal in time domain, where it looks like a burst and has very limited parameters in amplitude-time plots. A transient signal can be transformed in the frequency domain using Discrete Fourier Transform (DFT) algorithm.

3.2 Discrete Fourier Transform

When an analog continuous signal is captured using ADC and is sampled at a regular interval of Δt , it generates discrete time series with sampled signal $x(n)$ of N samples. The discrete Fourier transform, DFT, of the signal $x(n)$, is then defined as:

$$X(k) = \sum_{n=0}^{N-1} x(n) e^{-j2\pi kn/N} \quad (24)$$

Where $k = 0, 1, \dots, N-1$.

To get the time series from the spectrum $X(k)$, the inverse DFT is used and defined as:

$$x(n) = \frac{1}{N} \sum_{k=0}^{N-1} X(k) e^{j2\pi nk/N} \quad (25)$$

for $n = 0, 1, \dots, N-1$.

Each value, $X(k)$, of the DFT is referred to as a frequency line or bin at an increment of $\Delta f = 1/T$.

3.3 Energy of Transient

The transient signals have continuous spectra, but do not continue in time indefinitely as shown in Figure 15. The transient signals are represented by energy spectra and it is called Energy Spectral Density, ESD. The definition of the ESD is given as:

$$ESD = T.PSD \quad (26)$$

where, T is the time duration, the time to collect a one-time signal block.

The ESD can be interpreted the area under the curve of the energy in the signal. The simplest way to calculate the ESD is the sum of point-wise squared amplitude spectra of the signal.

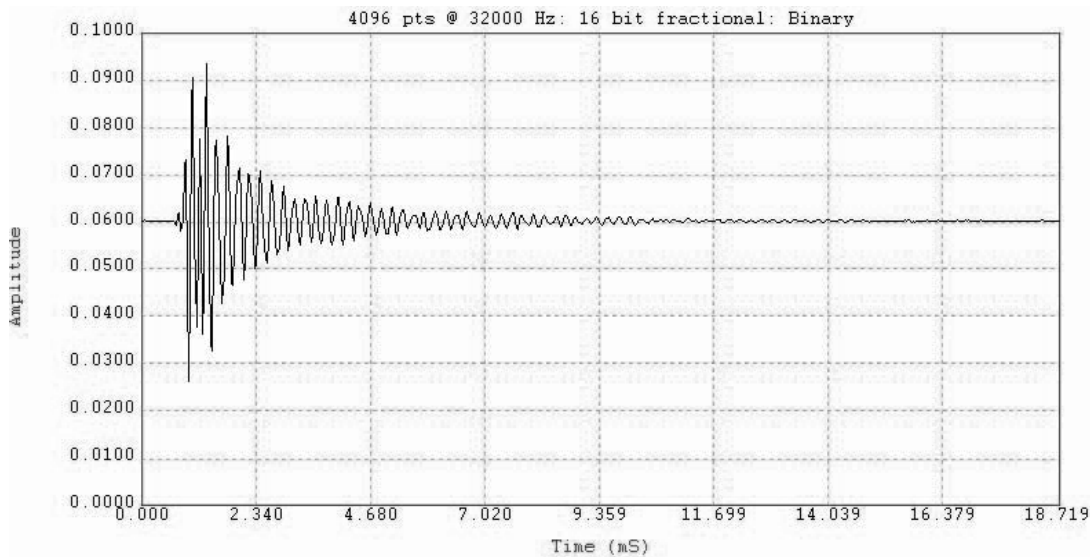


Figure 15: Typical transient signal from a Dimensional stone block

The continuous Fourier transform is the basis for frequency analysis of aperiodic and transient signals [38]. The Fourier transform, $X(f)$, of a time signal, $x(t)$, is defined by the Fourier transform integral as:

$$X(f) = \int_{-\infty}^{\infty} x(t) e^{-j2\pi ft} dt \quad (27)$$

The time signal can be calculated from the Fourier transform, $X(f)$, by the inverse Fourier transform defined by:

$$x(t) = \int_{-\infty}^{\infty} X(f) e^{j2\pi ft} df \quad (28)$$

The transient signals being of exponential decay type in nature, windows used in signal processing are not used, which means that there is no need for any correction factor. Instead, the measurement time is adjusted, if possible, so that the transient signal both starts and ends at zero to avoid leakage.

Figure 16 shows various transient functions and their amplitude spectra. It is seen that a transient pulse contains energy spread over all frequencies from zero to infinity and that the spectra are continuous with no discrete frequency components [39].

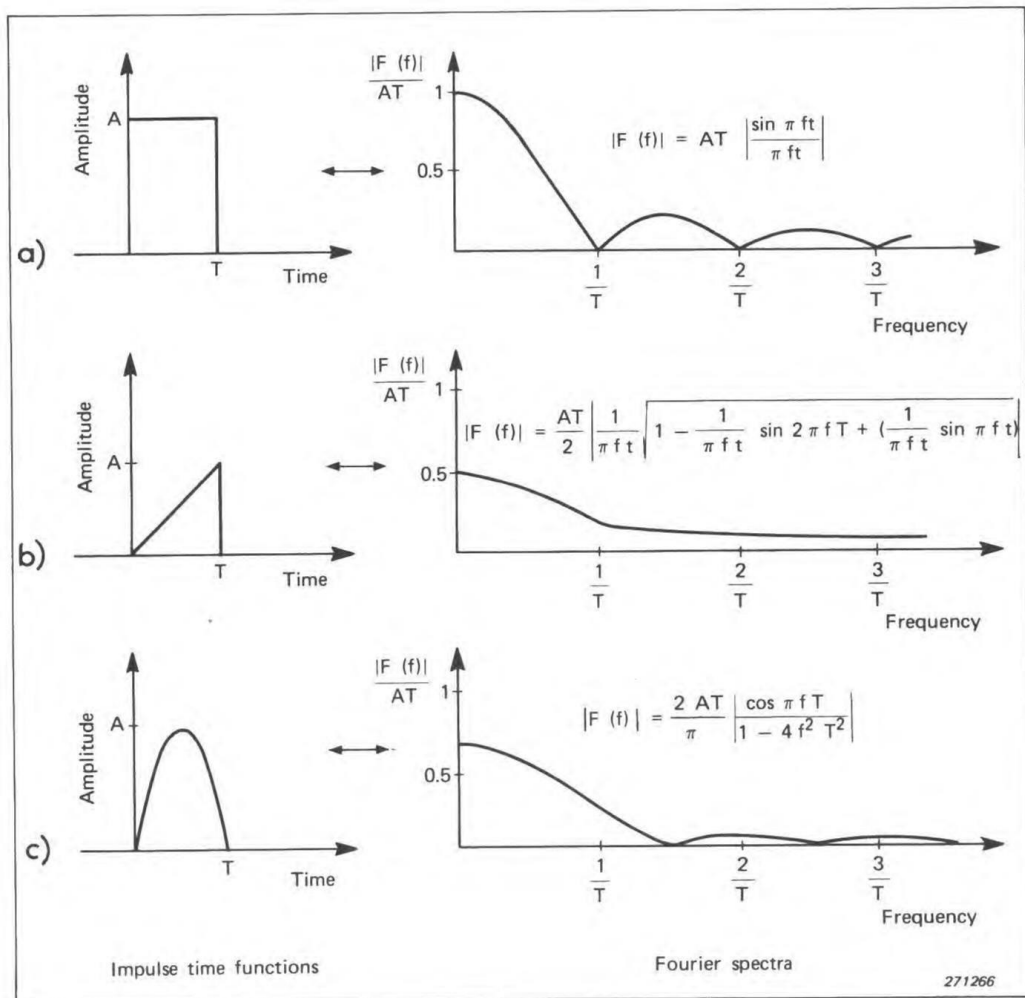


Figure 16: Examples of transient functions and their Fourier transforms. (a) A rectangular pulse, (b) A final peak saw-tooth pulse, and (c) A half-sine pulse [39].

3.4 Power Spectral Density Estimation

The power spectral density (PSD) estimation of a signal defines the distribution of the power of in a signal in the frequency domain. Estimation of PSD is used in the detection of signals buried in noise. PSD is commonly used in features extraction and identification of internal properties of materials through which the received signals have passed through. The quality of the estimation is affected by the size of samples and larger size gives better estimation [40]. The PSD estimation is divided into two major groups: parametric and nonparametric methods.

3.4.1 Nonparametric Methods

The nonparametric PSD estimation methods use Periodogram and its modified version uses the Fourier transform of the signal itself, albeit with some modifications. These methods have problems of low resolution, spectral leakage, aliasing error, violent fluctuation in spectral lines, difficulties in fitting smooth curves and unsuitability for the short data [41], [42] because of windowing effect. The limitation of methods lies in the assumption of the auto-correlation coefficients outside the window being zero [43, 44].

3.4.1.1 Periodogram Method

This method of estimating the PSD makes use of the DFT of the biased estimation of the autocorrelation function. For a signal, x_n , length of N , and sampling rate, f_s samples per second, the Periodogram is calculated as follows [40, 45]:

$$\hat{P}(f) = \frac{1}{N} \left| \sum_{n=0}^{N-1} x_n e^{-j2\pi f n} \right|^2 \quad (29)$$

The variance of $\hat{P}(f)$ does not decay to zero with N tending to infinity. The other issue with this method is the effect of a limited number of data which results in low-resolution and distorted estimation. To overcome above mentioned problems, several modifications have been proposed [40]. One of them is to reduce the variance by breaking the time series in multiple segments.

3.4.1.2 Bartlett Method

To address the convergence problem of the Periodogram, the Bartlett's method (averaging Periodogram) divides the data sequence into K non-overlapping segments of length L , defined as [40]:

$$x_m(n) = x(n + mL), \quad \text{where } n = 0, 1, \dots, L - 1 \text{ and } m = 0, 1, \dots, K - 1$$

The average Periodogram is defined as:

$$\hat{P}_{AV}(f) = \frac{1}{K} \sum_{m=0}^{K-1} \hat{P}_m(f) \quad (30)$$

where $\hat{P}_m(f)$ is calculated by equation (29) using segment length L . The variance of average Periodogram decays to zero as N tends to infinity. The variance in Bartlett's estimated spectrum is reduced by the factor of K and also provides consistent results [40].

3.4.1.3 Welch Method

The Welch method (modified Periodogram) implements two modifications in Bartlett's method viz. i) the overlapped data segments, and ii) application of windowing function to time series. In this method, a modified Periodogram for each segment is estimated and an average of these estimates is used to get the final power spectral density estimation. The segments can be defined as [40]:

$$x_m(n) = x(n + mD)$$

where, $n = 0, 1, \dots, L - 1$, $m = 0, 1, \dots, K - 1$ and D is the size of overlapped segment and $D \neq L$. The modified Periodogram is given below based on overlapped segmentation [40, 46]:

$$\hat{P}_m(f) = \frac{1}{L} \left| \sum_{n=0}^{L-1} x_m(n) w(n) e^{-j2\pi f n} \right|^2 \quad (31)$$

The Welch estimation is the average of modified Periodograms and given as [40, 46]:

$$\hat{P}_W(f) = \frac{1}{K} \sum_{m=0}^{K-1} \hat{P}_m(f) \quad (32)$$

3.4.1.4 Windowing

The use of a limited size of data in spectrum analysis is same as multiplying by the rectangular window to the signal in the time domain. At the start and end, a window function decays to zero. By multiplying the window function to the time series data, the output tapers the data gradually and addresses the leakage problem of the periodogram, it also guards against the loss of information caused by windowing [45]. There are popular window functions: Rectangular, Hamming, Hanning, Bartlett, Kaiser, and Blackman.

Figure 17 shows four common windows used in the time domain and their frequency spectrum with a sampling rate of 1Hz, a window length of 64 and a signal length of 1024.

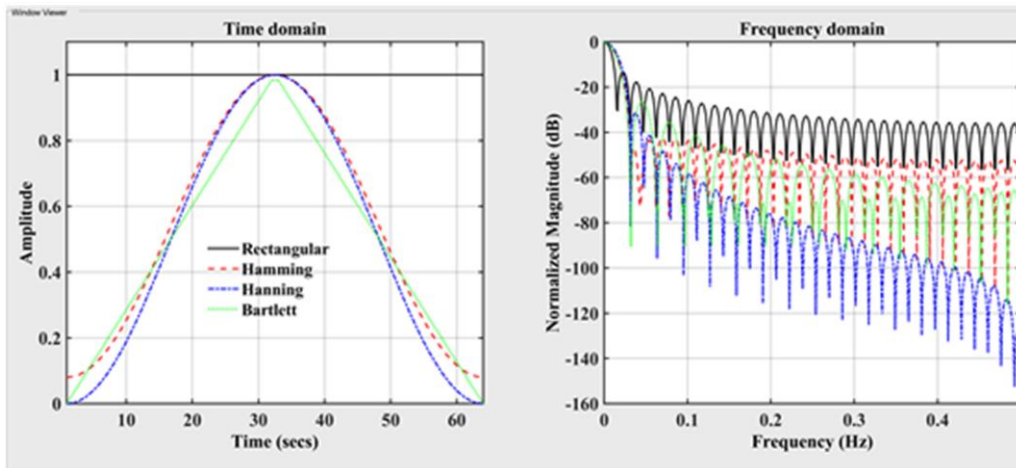


Figure 17: Window function's time and frequency domain plots. Sampling rate of 1 Hz, a window length of 64 and signal length of 1024.

Table 4 shows the window's parameters while selecting a suitable window for an application. There are two important parameters while selecting window function [40]: (i) its length and (ii) window type. These parameters decide the performance of the main lobe width and the side lobes' power. The length of the window defines the main lobe width. When window's length increases, the main lobe width decreases. A narrow main lobe width provides better resolution, i.e. has the ability to separate very close frequencies in the signal. The effect of the window type controls the leakage from the other frequencies to the main lobe. Based on application and intended

information, selection of the window function and its length are decided and then data are processed to resolve closely spaced sinusoids present in the signal.

Table 4: Window function parameters at the sampling rate of 1 Hz, a window length of 64 and signal length of 1024 samples.

Name of window	Leakage factor (%)	Relative side lobe attenuation (dB)	Main lobe width (-3dB) (mHz)
Rectangular	9.14	-13.3	13.672
Hamming	0.03	-42.5	19.531
Hanning	0.05	-31.5	21.484
Bartlett	0.28	-26.5	19.531

3.4.2 Parametric Methods

The non-parametric methods have some disadvantages for the limited size of data samples. For achieving reasonable resolution from the non-parametric methods, a long set of data is needed and use of windowing is essential. The leakage may restrict in finding weak signals in the data. These weaknesses are addressed by parametric methods. They assume that the data are the output of a linear system driven by wideband white noise and then estimate the model parameters of that linear system [47]. These methods have better characteristics and can yield higher resolutions for a shorter length and aperiodic signals. For *impact transient signals, being nonperiodic and limited in length, parametric methods are more suitable*. Among the parametric methods, the Burg method is most suitable due to its stable output model for a limited length of data and less number of linear equations needed to solve the AR parameters.

3.4.2.1 Burg Method

It is based on minimising the forward and backward prediction errors while satisfying the Levinson-Durbin recursion [44, 48]. The estimation of the reflection coefficients is done directly instead of calculating the autocorrelation function. This method has problems of frequency shifting for the small sample record, and for higher SNR, line splitting may appear in the PSD [47].

This method assumes that the data, $x(n)$ is the output of a linear system where $x(n)$ satisfies an auto-regression model with an order p defined as:

$$x(n) = \sum_{i=0}^p a_p(i)x(n-i) \quad (33)$$

where $a_p(i)$ are real-valued AR model coefficients. The PSD estimate of the data with a sampling interval of time, T is given as:

$$P(f) = \frac{e^{2T}}{\left|1 + \sum_{i=1}^p a_p(i)e^{-j2\pi fT}\right|^2} \quad (34)$$

where e^2 is the minimised least square error [49].

Optimal selection of the order p is an important step in AR methods. Final Prediction Error (FPE) and Akaike Information Criterion (AIC) given by Akaike [50] are common criteria to calculate the AR order. The other criteria such as Criterion Autoregressive Transfer (CAT) by Parzen [51], Minimum Description Length (MDL) by Rissanen [52], and Residual Variance (RV) [53] are also reported. The order is selected by a minimum of the following criteria:

$$FPE(p) = \sigma^2 \frac{N + p}{N - p} \quad (35)$$

$$AIC(p) = N \log(\sigma^2) + 2p \quad (36)$$

where N is the number of samples in $x(n)$ and σ^2 is estimated prediction error variance of the white noise for order p [54].

The flowchart in Figure 18 shows the process of data acquisition, the estimation of PSD using the Burg method.

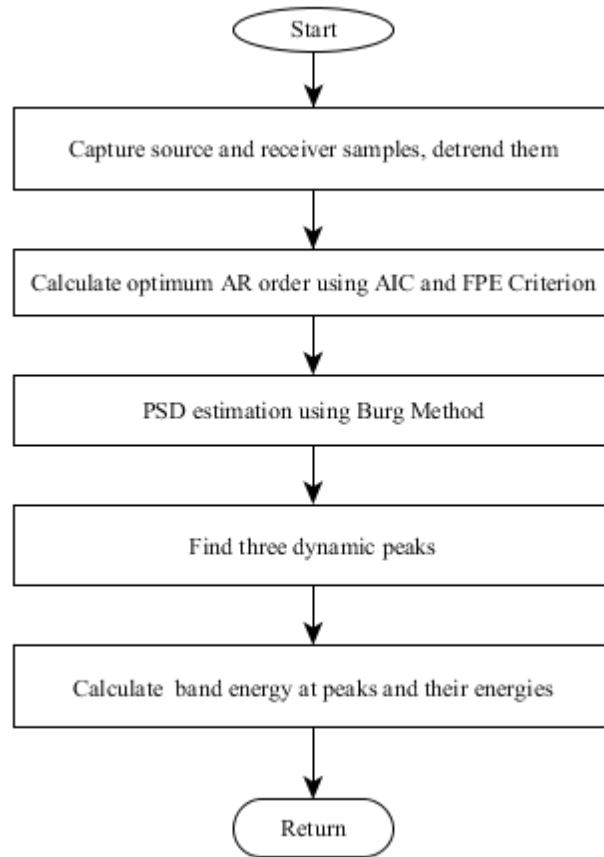


Figure 18: Flowchart of PSD estimation by the Burg method

3.5 The Proposed Method

The defect assessment techniques based on measurement of vibrations assume [55–57] that:

- The propagation of the acoustic waves because of vibration get affected by the medium through which they travel.
- The defects such as cracks, voids, and fissures change one or more structural properties of the material, i.e., mass, stiffness and damping. The major impact will be on stiffness and damping of the material.
- These changes lead further change in the dynamic properties of natural frequencies, mode shapes, and damping ratio.

In the 80s, damage detection techniques were focused on changes in natural frequencies due to damages. Cawley and Adams developed a method for detecting imperfections in an FRP plate, on the basis of changes in natural frequencies [55]. In

the proposed method in this research work, the acoustic stress wave transmission characteristics through solids are selected in preference to other characteristics.

The incident transient wave signal gets dispersed due to the presence of a defect within the medium. The pattern of dispersion depends upon the inherent defect and if this pattern is discernible, the defect can be determined. Basically, the defect changes the stiffness, mass, and damping properties of the material which results in shifting of the natural frequencies of the system when energised by a transient source. The shift depends on how the flaws interact with the specific defect pattern. When the frequencies of excitation coincide with one or more natural frequency of the system, the resonance occurs, and there will be peaks in the response spectrum. The numbers of peak depend on the number of the excitation frequencies match to the natural frequencies of the system.

This behaviour may be due to defects behaving like mechanical capacitive low pass filters in solids for an acoustic wave when they pass through it and allows passing through the selected frequencies only and other frequencies get attenuated. The analysis of received signal for the intactness of the medium is done using the following fundamental wave principles:

1. Defect behaves like a capacitive low pass filter in the solids for the acoustic waves when they pass through them and allows passing of the selected frequencies only while other frequencies get attenuated. The allowed frequencies' cut off depends on medium stiffness between the source and the receiver and mass of the material.
2. Defect changes one or all physical properties, stiffness, mass, and damping of the material which results in a change in the natural frequencies of the system.
3. Whenever the frequencies of an external driving source coincide with one or more natural frequencies of the system, the resonance occurs (i.e. peaks in response spectrum).

Unlike the reflected signal (echo) forming the core of classical acoustic stress wave methods, it is based on the analysis of the signal passing through the defective

medium under test (transmitted one). Salient features of the proposed methods are as below:

- The received signal is the one recorded across the object (on opposite or adjacent face) instead of being on the same face (reflected).
- Instead of using the conventional echo from the flaws, the spectral redistribution in the received signal and the energy contained around dominant bands (surrounding peaks) are used as the discriminants for the defect detection.
- The signal processing is done in the spectral domain and the spectral characteristic of the signal is used for parametric analysis.

It is important to note here that shifts in the resonant frequency bands are measurable if the defect is structurally significant for either the size or the location of the flaw within a specific resonance mode shape. Hence, sometimes minor flaw might get overlooked, under this resonance peak criterion.

Chapter 4: Data Acquisition

4. Data Acquisition

Proper data acquisition is an important step in the sensitive diagnostic studies proposed in the present research work. This chapter describes the test instruments and the software used for data collection and analysis.

4.1 Introduction

To achieve the objective of the study, an instrumented impulse hammer, USB interface based data acquisition module, and IEPE accelerometer are used, software to capture data and processing is written in MATLAB [58].

Finally, one prototype unit is developed incorporating the algorithm in the on-line data processing for classification of the diagnostic pattern. This is proposed for use in the field for further study and collection of data. The material density of the dimensional stone block and P-wave velocity through them are calculated for marble blocks from different mines. The impulse hammer with stainless steel tip is selected as vibratory sources of transient frequencies within 0 – 5.0 kHz [59].

The schematic setup of the data acquisition module comprising instrumented impulse hammer, accelerometer and USB based DAQ unit interfaced with the laptop is shown in Figure 19.

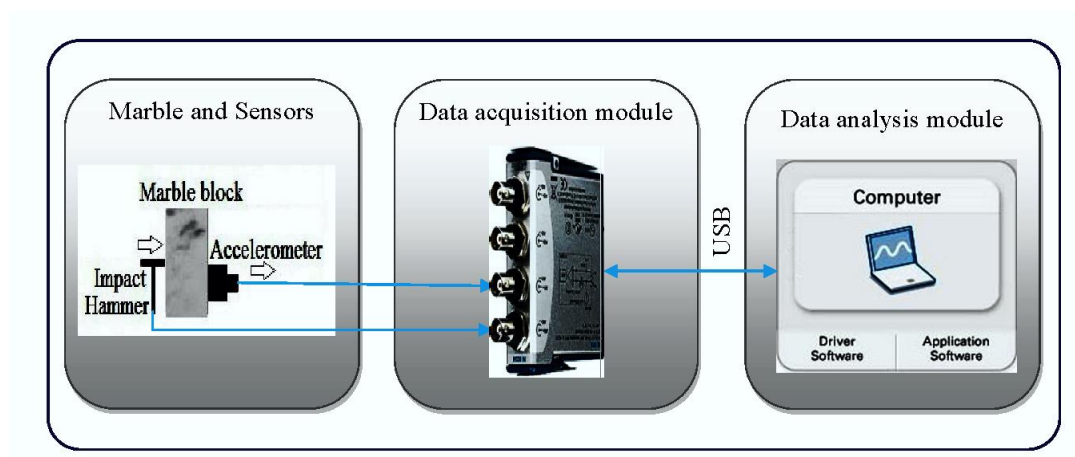


Figure 19: schematic diagram of measurement setup with NI 9234.

Figure 20 shows the actual photograph of the data collection process from the marble block in the field using the proposed method.



Figure 20: Photograph of data collection setup from a marble block in the field.

4.2 Impulse Hammer

The force-time history of an impact hammer is a transient energy transfer pulse. Its force amplitude spectrum is a continuous one with maximum amplitude at DC and decreasing with increasing frequency [60] as shown in Figure 21. The spectrum has a periodicity with zero force at frequencies of n/t_c intervals, where n is an integer and t_c is the duration of the transient (i.e., contact duration of hammer tip to the surface of the object).

The force-time history of the impact of the impulse hammer can be considered as a half cycle sine curve [60], [61] with the impact duration t_c . The duration and shape of the spectrum of an impulse impact depend on the material of hammer tip and stiffness of the structure under impact. For a rough estimate, the highest frequency component with the significant amplitude in the spectrum equals the inverse of the contact time [21].

The useful frequency range of an impact hammer is calculated by observing the force amplitude spectrum of the impulse hammer. It can be found by looking from DC to a frequency F , at which point the spectrum magnitude has decayed by 10 to 20 dB [60]. In order to adequately excite the test object for a selected frequency range, the Fourier sampling frequency must be at least 1.25 times the highest desired frequency for study [61].

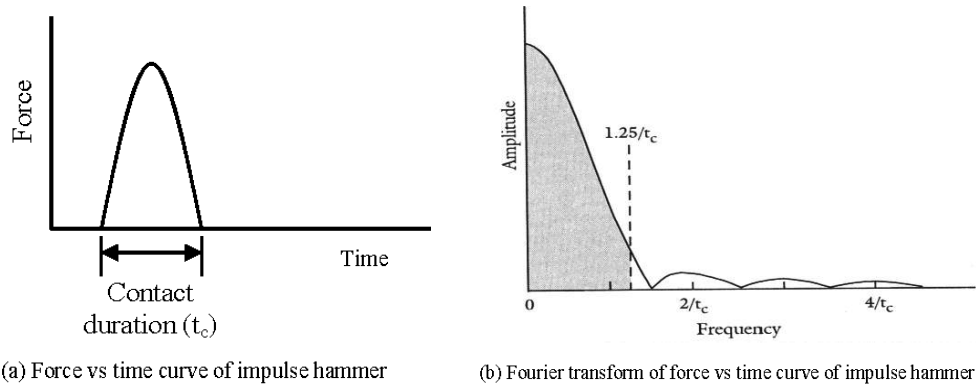
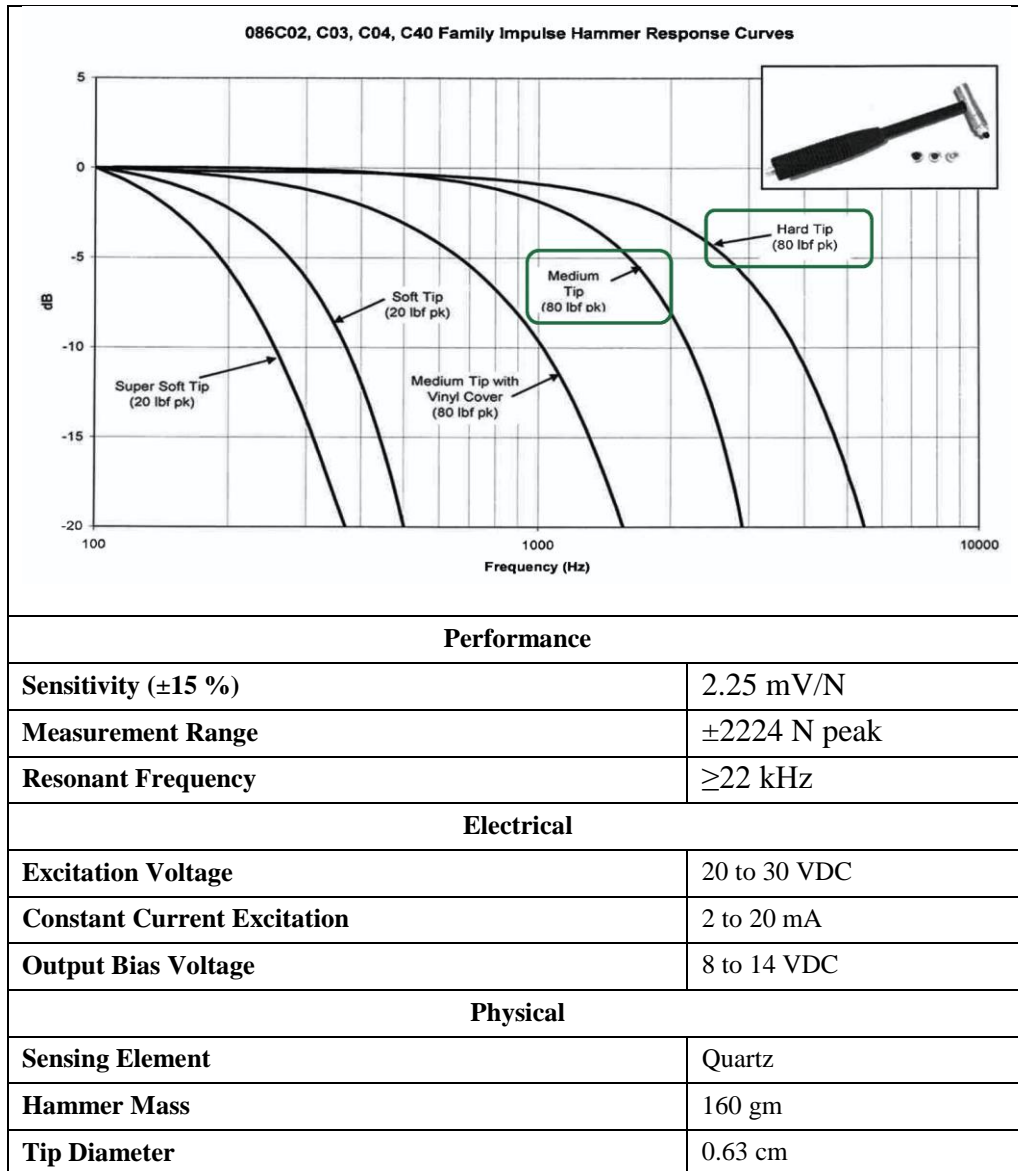


Figure 21: Parameters of impulse hammer with force sensor (adopted from [61]). (a) Shows force vs time history of impulse hammer, where t_c is surface contact duration (b) Shows Fourier transform of force vs time history. The shaded portion shows useful frequency range of impulse hammer.


In the present study, the impulse hammer with stainless steel tip model no. 086C03 with a force transducer from PCB Piezotronics, Inc., USA is used as the source which generates a maximum frequency of 5 kHz. The detailed specifications and different upper tip frequency for various material tips of instrumented impulse hammer are listed in Table 5.

Table 5: Specifications of the Impulse hammer Model 086C03, PCB Piezotronics Inc., USA [62].



Finally, after the development of a prototype instrument, data are collected with stainless steel hammer source. The detailed specifications of this model with its image are listed in Table 6.

Table 6: Roundhead point hammer with fibreglass handle, Model GY10565 [63]

	
Material	Stainless Steel
Weight	300 gm
Manufacturer	Shaurya Industries, Jalandhar, India.
Model	Goodyear Ball Pein Hammer, GY10565

4.3 Piezoelectric Accelerometers

A piezoelectric accelerometer is selected for data capturing exercise in the present study because its frequency response is flat within the range of interest (1000-3500Hz) of the vibratory mechanical signal required for defect characterisation or identification. Even earlier tests conducted in dimensional stone blocks [59] reveal that most of the recorded transient frequency of vibratory signals lies within 100 - 5000 Hz.

The accelerometer's upper frequency limit is dependent on its resonance frequency whereas the lower cutoff frequency is limited by the time constant of the charge amplifier. A typical frequency response of an accelerometer is shown in Figure 22, an amplitude rise of ~5% is expected at ~1/5 of the natural resonance frequency, f_n .

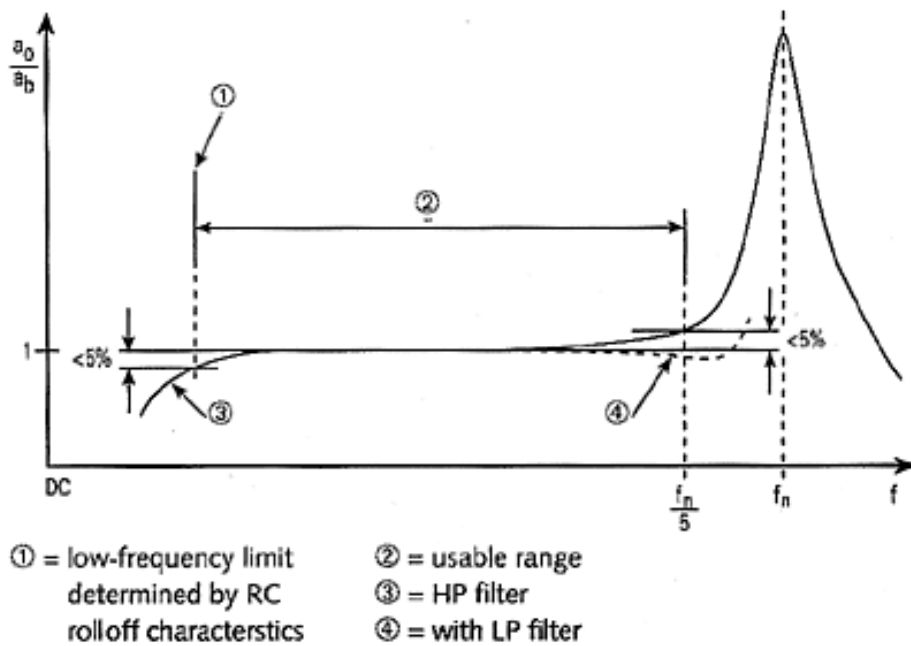


Figure 22: A typical response curve of the accelerometer. 1 = low-frequency limit determined by an RC roll off characteristics; 2 = usable range; 3 = high-pass filter; and 4 = with a low-pass filter, which can be used to attenuate the effects of the amplitude rise at $\sim 1/5$ the resonance frequency [64].

In the present study, the impulse signals generated by instrumented hammer are captured using IEPE accelerometer, ceramic shear mode, Model 352C03 from PCB Piezotronics, Inc., USA. It was directly connected to data acquisition module. The detailed specifications of this model are listed in Table 7.

Table 7: Specifications of the accelerometer Model 352C03, PCB Piezotronics Inc. [65]

Performance	
Sensitivity ($\pm 10\%$)	1.02 mV/(m/s ²)
Measurement Range	± 4900 m/s ² peak
Frequency Range ($\pm 5\%$)	0.5 to 10000 Hz
Resonant Frequency	≥ 50 kHz
Electrical	
Excitation Voltage	18 to 30 VDC
Constant Current Excitation	2 to 20 mA
Output Bias Voltage	7 to 12 VDC
Physical	
Sensing Element	Ceramic
Weight	5.8 gm
Sensing Geometry	Shear
Electrical Connector	10-32 Coaxial Jack



In prototype device, charge output type of accelerometer is selected because of low power consumption and its cost. It does not need high voltage biasing and excitation current to operate. The impulse signals generated by a ball point hammer for the prototype device are captured using charge output accelerometer, shear mode, Model 2224C from Endevco Corp., USA. The detailed specifications of this model are listed in Table 8.

Table 8: Specifications of the accelerometer Model 2224C from Endevco Corp. [66]

Dynamic characteristics	
Charge sensitivity(pC/g, typical and minimum)	12 and 8.5
Amplitude response ($\pm 5\%$)	1 to 6000 Hz
Resonant Frequency	32 kHz
Shock limit (g peak)	2000
Electrical	
Output polarity (Positive output)	Acceleration into the base
Resistance (G Ω)	≥ 10
Capacitance (pF)	800
Grounding (Signal ground)	Transducer case
Physical	
Sensing Element	Piezite® type P-8 crystal
Weight	16 gm
Sensing Geometry	Shear
Electrical Connector	10-32 Coaxial Jack



4.4 Mounting of the Accelerometer

While mounting an accelerometer it is necessary to have clean and smooth surface. The smallest bit of dirt or surface roughness may make elasticity in the mounting, which can seriously influence the measurement. Various methods are available for mounting of the accelerometer and common methods are screws, glue, wax, and magnets. The mounting of accelerometer has spring action with a certain stiffness. This spring stiffness and the accelerometer's mass reduces the original resonance frequency resulting limiting the measuring range.

The accelerometer signal rises sharply when the frequency approaches its mounted resonance frequency, f_{mount} . Normally, a frequency range up to $f_{mount}/4$ is used for a maximum error of approximately 5%, or $f_{mount}/3$ for a maximum error of approximately 10% [38]. It is impossible to predetermine this resonance frequency since it depends on the object's stiffness at the mounting point. The influence of mounting methods on the frequency range of the accelerometer is shown in Figure 23 [67].

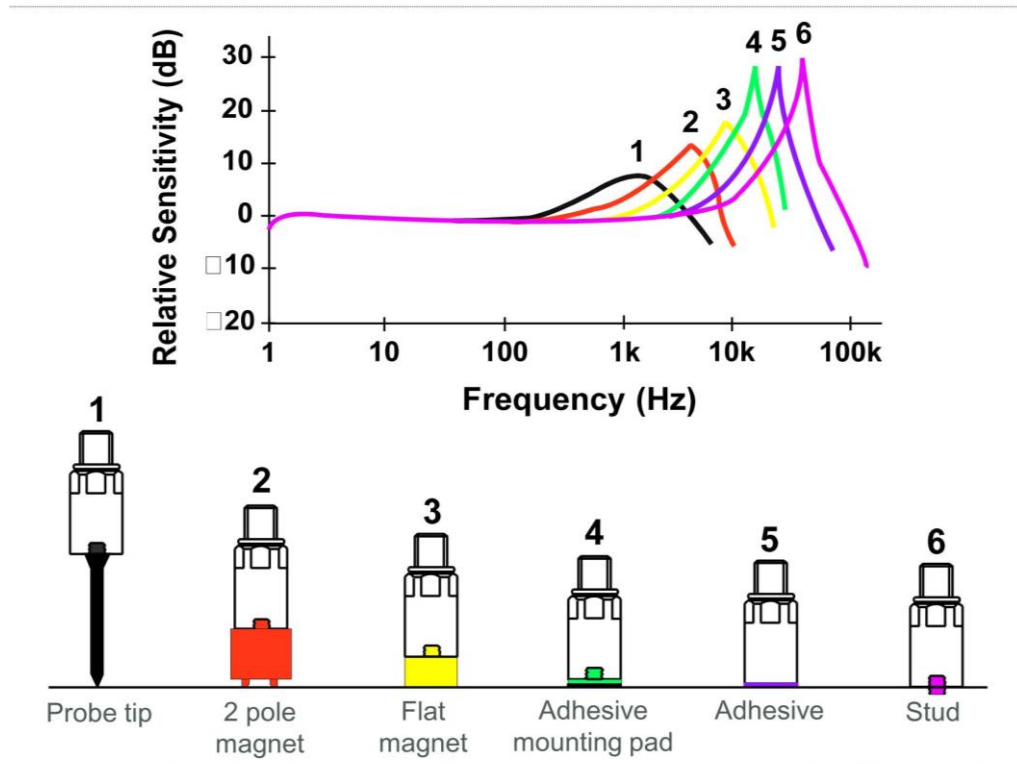



Figure 23: Different mounting methods and their effects on the higher frequency range of an accelerometer [67]

4.5 Data Acquisition Module

The transmitted impulse signals are captured by an accelerometer mounted at a distance and recorded by a laptop PC through the USB port of NI based 4-channel data acquisition (DAQ) module connected to the laptop. This DAQ module has four input channels for IEPE type sensors; out of them only two are used in the present case - one for the force sensor of instrumented hammer and other for the accelerometer. The major features of the module which make it an ideal device for such measurements are shown in Table 9.

Table 9: Specifications of the Data acquisition module NI 9234 from NI [68].

Numbers of Channels	4 analog inputs	
ADC resolution	24 bits	
Type of ADC	Delta-Sigma	
Sampling mode	Simultaneous	
Sampling rates	1.652 to 51.2 kS/s	
Input coupling	AC/DC	
AC cutoff frequency	-3 dB for 0.5 Hz	
Input voltage range	±5V typical	
IEPE excitation current	2.1 mA typical	
Alias-free bandwidth	0.45*Sampling rate	

4.6 Source and Receiver Orientation Setup

Figure 24 shows the data acquisition setup in which the source (hammer hit point) and the receiver (sensor pick up point) locations are shown. The inherent crack in the medium is also shown therein. Transmitted signals around this crack are captured on various faces. Hit points (source) are accordingly laid in the different orientation as explained in Table 10.

Table 10: Orientation of source and receiver on a dimensional stone block

Hit point (Source)	Location of hit point	Receiver location	Intervening medium	Remarks
1	Left side face	Front face	Crack present	Semi-direct
2	Front face		Crack present	Indirect
3	Front face		Intact	Indirect
4	Right side face		Intact	Semi-direct
5	Opposite face		Crack present	Direct
6	Opposite face		Crack present	Direct
7	Top face		Crack present	Semi-direct
8	Top face		Intact	Semi-direct

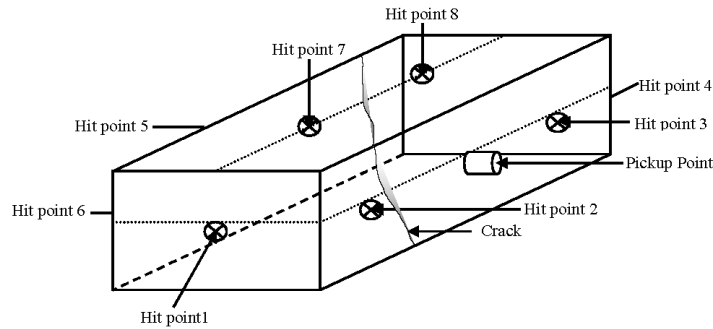


Figure 24: Typical pickup sensor and impulse hammer impact points on a dimensional stone block

The signals are captured by keeping the pickup sensor at one place and hitting with a roving impact hammer on different locations / faces. The data were captured from direct, semi-direct and indirect points. Only direct and semi-direct points are used for analysis; direct point data being more reliable because they are sure to pass through a defect in the media. The data has been collected from various marble blocks of mines located in different geographical places.

4.7 MATLAB Application ImpulseScope

4.7.1 Introduction

The data collection and analysis in the lab and field are done using available commercial software and hardware packages like from Dytran, Igor, Data Translation and B&K which include acquisition hardware and associated software. These are also used in industries to measure the dynamic performances of civil structures and mechanical systems. These tools have lots of features, efficiency, and user-friendliness with dedicated applications in mind to satisfy the particular segment of the market. They have very limited flexibility to customise according to new research needs.

An application with graphical user interface called “*ImpulseScope*” has been developed using the MATLAB [58] scripts and off the shelf hardware to collect and study data from marble blocks. It allows calculation and analysis of transient response spectra using standard hardware from market to address the problem of flexibility, easy to use and configure and expandability of functionalities whenever required by research. The spectra of impulse transient response are calculated from force-acceleration-time data collected from marble blocks in the field. The application has functionalities to capture the data using NI 9234 data acquisition module from

National Instruments. The application has two major parts. The first one is used for acquiring data of marble blocks on the field, called “*Data Acquisition*” and another one, “*Post Processing*” allows the signal processing of collected data from the field, e.g. FFT, Energy, PSD, Transfer Function and so on.

4.7.2 Data Acquisition

MATLAB has been chosen to develop the application due to its inbuilt data acquisition (DAQ) toolbox for NI, the familiarity of script writing in MATLAB. The application developed to capture the data with the help of NI USB 9234, IEPE accelerometer and instrumented impulse hammer with force sensor and impulse hammer channel as a trigger source with a threshold level.

Figure 25 shows the flowchart of start-up of application which is common for data acquisition and post-processing phases. There are two types of settings and are stored in the system. The first one is related to the accelerometer and instrumented hammer used for the data collection as shown in Figure 29 and the other one is from the block and session profile which is shown in Figure 30. When the application launches, the user has to verify following settings for data acquisition. It is also possible to change or modify following parameters:

- Data acquisition module hardware
- The sampling rate in Hz – one from the list
- The trigger level in volts
- The pre-trigger data in samples – one from the list
- The number of data per event – one from the list
- The sensitivity of each channel based on sensor connected
- The channel used for triggering, i.e. force sensor or impulse hammer
- Data capturing mode, i.e. single or multiple events
- Data logging mode, i.e. manual or automatic saving of the captured event
- Testing face of the block and a number of hit points on the face
- Data logging path

Figure 26 shows the flowchart of the data acquisition phase. After setting all the parameters of sensors and session, the session can be started, the application captures from the both channels continuously and displays the force-acceleration-time history on right-hand side top plot area in two different colours with a common time scale as shown in Figure 30. In the background, data from the force sensor, i.e. trigger channel is monitored for trigger level also as shown in Figure 27, once the signal from trigger channel crosses the set trigger level, data from both channels are captured of an event including pre-trigger samples. These captured data for an event are plotted in right-hand side lower plot areas force and acceleration respectively as shown in Figure 30. The user will be prompted to check signals, i.e., multiple hits because of a single hammer hit, saturation of the signal and probable shape to accept or reject the captured data. Based on data capture and log modes, the session will be continued. The force and acceleration data for every event are saved in separate files and names are generated automatically based on a selected face of the block and other user defined parameters so that they can easily co-relate with actual marble block to identify later stage during post processing.

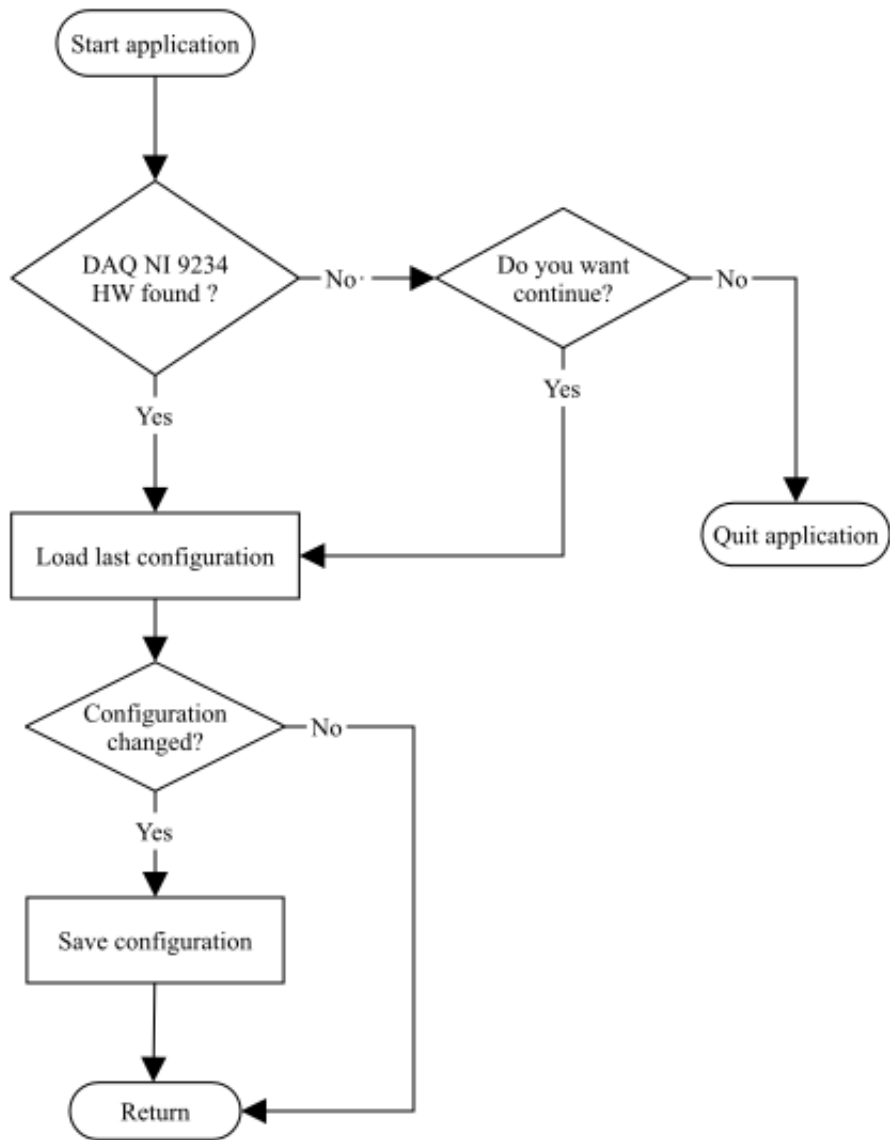


Figure 25: Start-up flowchart of MATLAB application.

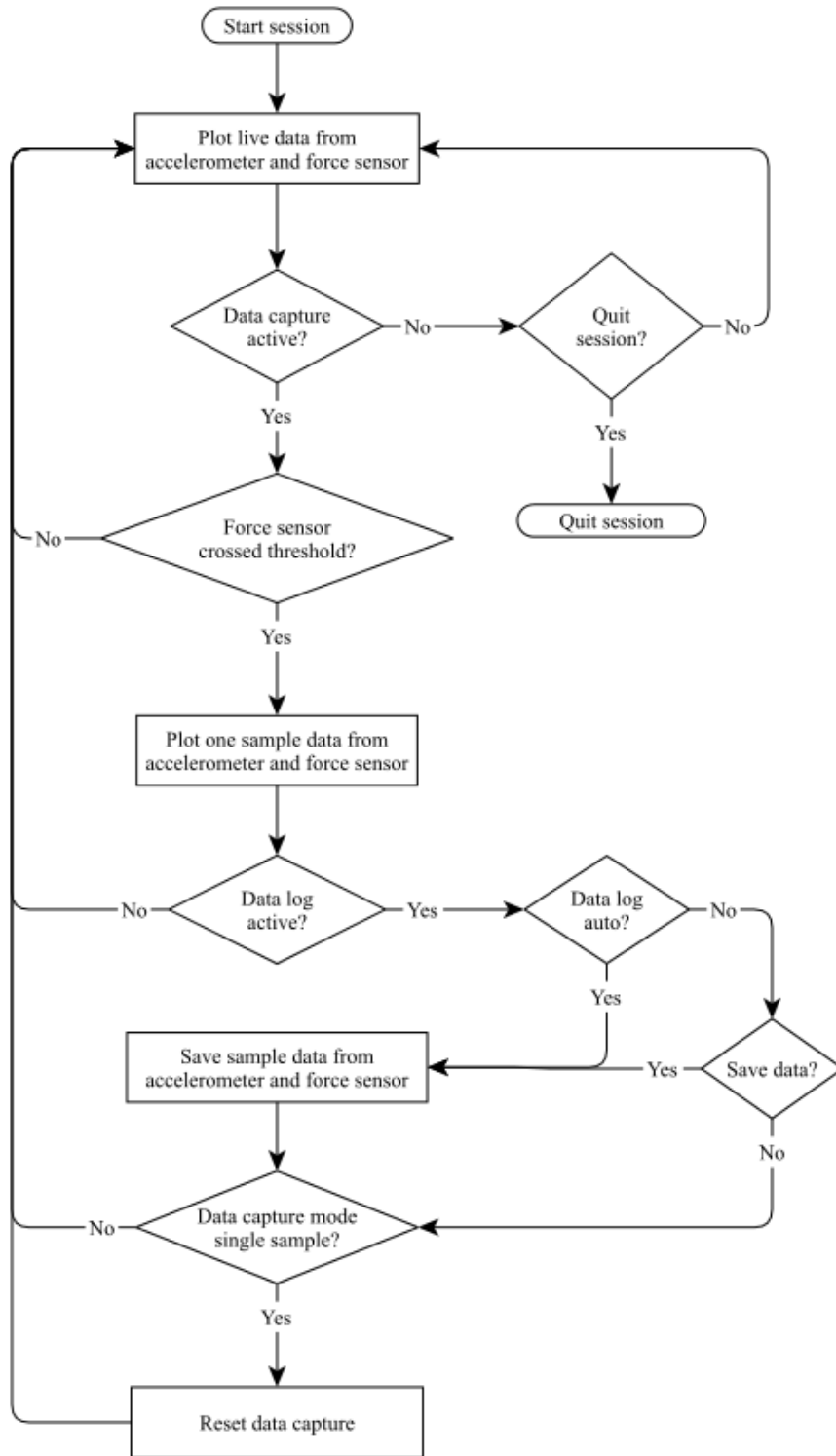


Figure 26: Data capturing flow diagram of MATLAB application.

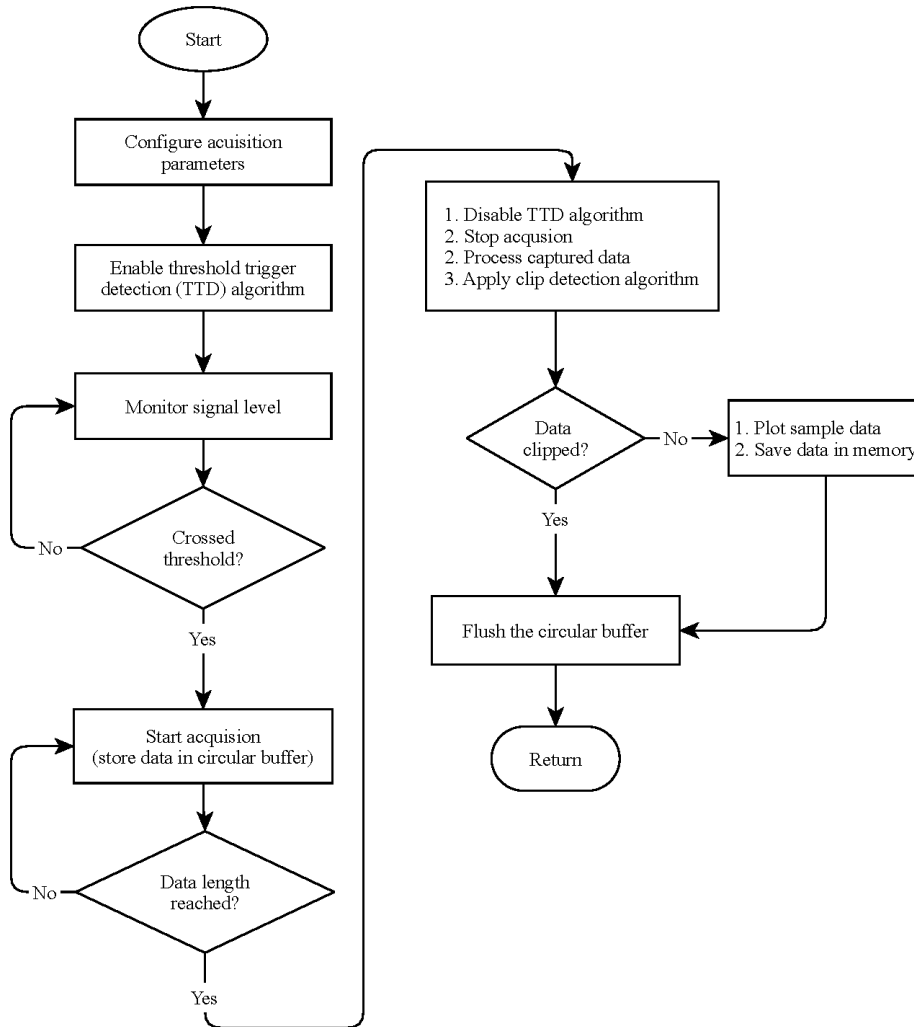


Figure 27: Trigger Mechanism of data capturing from marble blocks.

4.7.3 Post Processing

After capturing the data from different faces of the blocks, the post-processing can be done offline. The post-processing allows calculating, displaying, and saving of FFT, STFT, PSD and other selected data to study the material properties and their effects on acoustic wave propagation. The structure of post-processing is shown in Figure 28. Before processing of data, following settings needed to verify of DAQ Parameters:

- Sampling rate, number of samples per event
- Sensitivity of sensors used

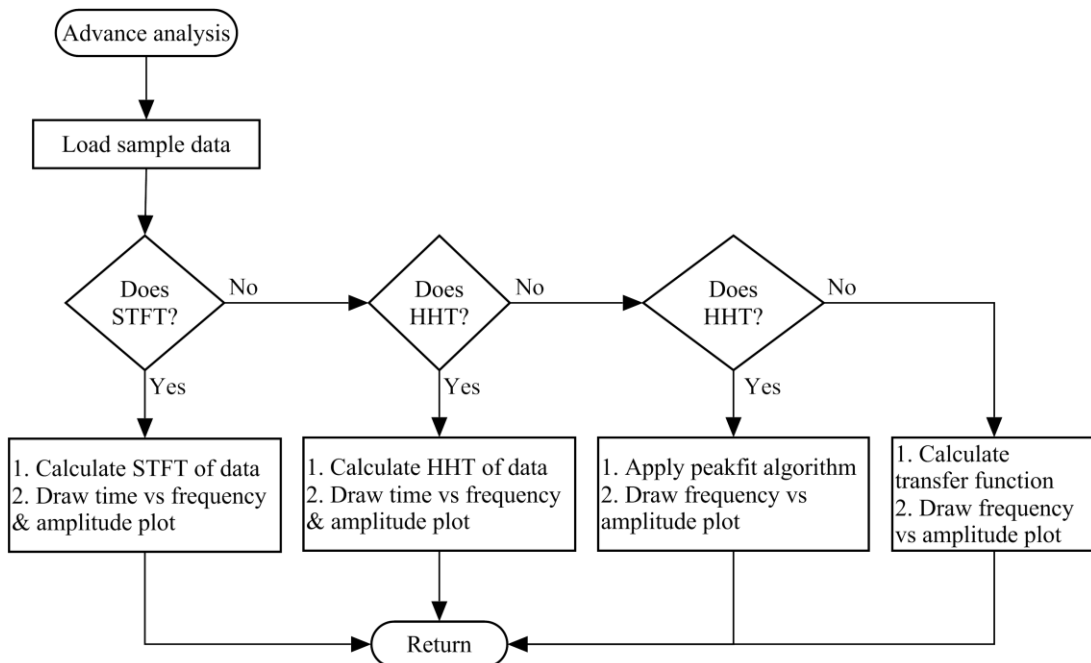
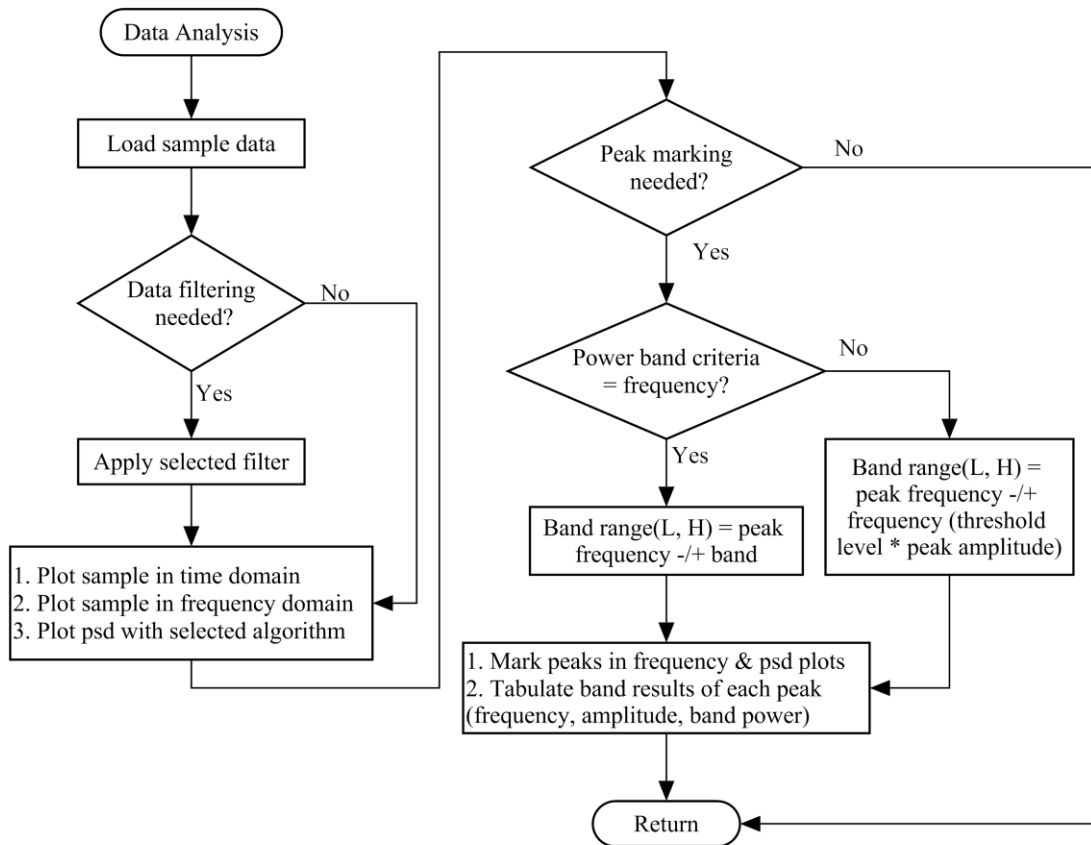


Figure 28: Post processing diagram of data in MATLAB application.

Once above settings are checked, based on selected algorithm, the reports and plots are generated for results analysis and storage. The output files (plots, result, and captured data) have own file extension, to indicate data type and identify the nature of data later easily.

4.7.4 DC Removal and Filtering

A DC offset gets added to the captured transient signal due to the problem in hardware, data acquisition module and it is called the zero-shift. It needs to be removed prior post processing of data. The zero-shift may occur due to: the noise in wires, an overloaded piezoelectric element or noise in the power supply. The zero-shift can be corrected by using a high-pass filter or subtraction of the mean of the signal. The application uses subtraction of the mean of the signal from the signal to correct the zero-shift.

4.7.5 GUI Screens

The screens of MATLAB application are shown from Figure 29 to Figure 32. Figure 29 shows the selection of DAQ acquisition parameters: DAQ module, samples per trigger, pre-trigger samples, sampling rate, trigger threshold, hammer and accelerometer channels and sensitivities. After changing these parameters, they can be saved for future use. The shown values are default values for data capturing.

Session Parameters		
Device Name	Total Samples	PreTrigger Samples
Unknown	1024	16
Sampling Rate(Hz)	Trigger Channel	Trigger Level(V)
25600	ai0	0.2
Impulse Hammer	Channel	Sensitivity(mV/N)
	ai0	2.25
Accelerometer	Channel	Sensitivity(mV/m/s^2)
	ai1	1.02
Save Parameters		

Figure 29: Data acquisition parameter setting screen

The Figure 30 shows the data capturing and storing menu screen. The left-hand side of the screen are the mode of operations like single or continuous capturing, data logging, stone back face name and data storage location. The top area on the right side

of the screen is reserved for live data plots of a hammer and accelerometer on a common time scale. It shows the continuous live data from the force and accelerometer sensors. The bottom area on the right side of the screen has two areas for hammer and accelerometer time histories. Once the hammer signal crosses the threshold level, data are captured and hammer and accelerometer data displayed in these two windows separately. The pop-up window comes up to save or reject the captured data provide data logging is active in manual mode.

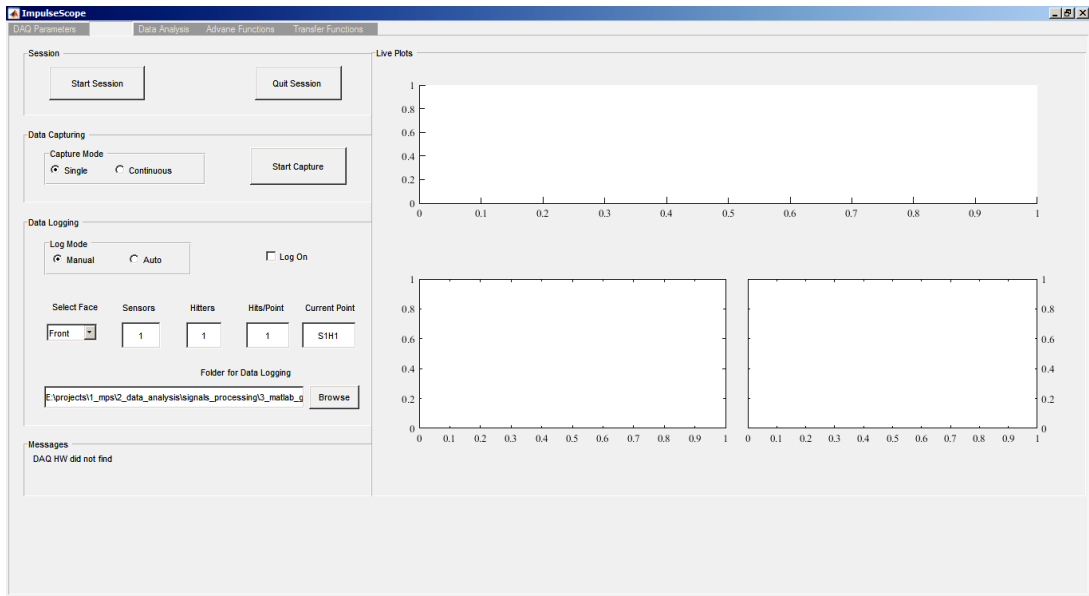


Figure 30: Data session capturing and storing screen

Figure 31 shows the data analysis screen. The left-hand side of the screen is data file location and name, PSD algorithm selection, the range of interested frequencies, peak parameters and results of the analysis in a tabular format. The results of the analysis are also saved in CSV format for reports. The top plot on the right side on the screen shows the time histories of the hammer (black line) and its response (blue line) captured by an accelerometer on a common time scale. The middle plot on the right side on the screen shows the spectral amplitude of the hammer (black line) and its response (blue line) captured by an accelerometer on a common frequency scale. The bottom plot on the right side on the screen shows the power spectral density estimation of the hammer (black line) and its response (blue line) captured by an accelerometer on a common frequency scale.

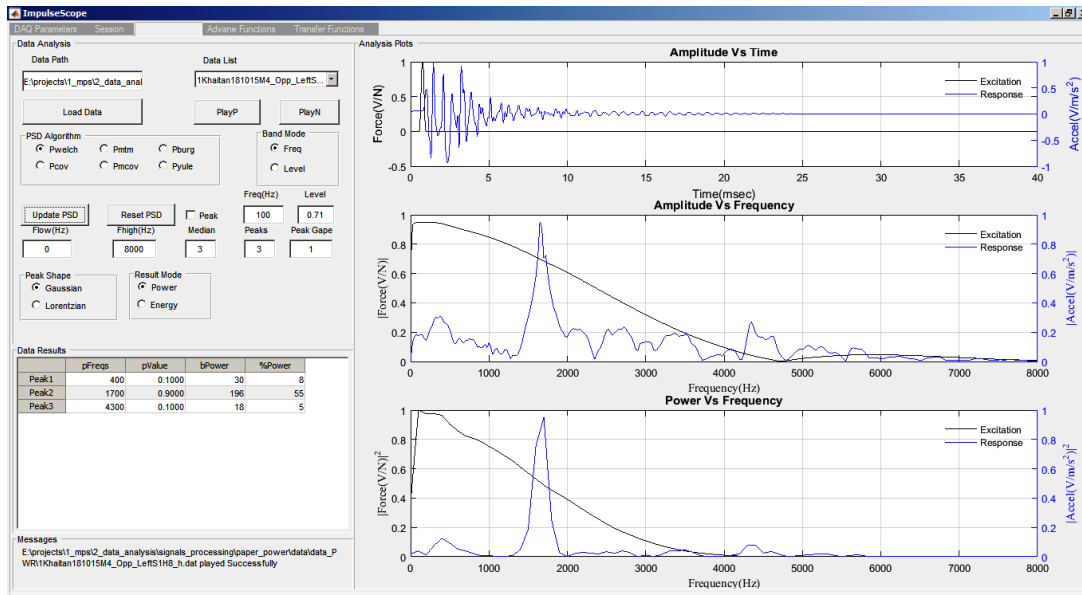


Figure 31: Data analysis screen (FFT and PSD)

Figure 32 shows the frequency response function (FRF) screen. The left-hand side of the screen is data file location and name. The right side of the screen shows the time histories, spectral amplitude, and power density estimation of the hammer (black line) and its response (blue line) captured by an accelerometer on a common time scale. The bottom right plot shows the FRF of the stone block. The ImpulseScope also has advance analysis functions like HHT and STFT which are not described.

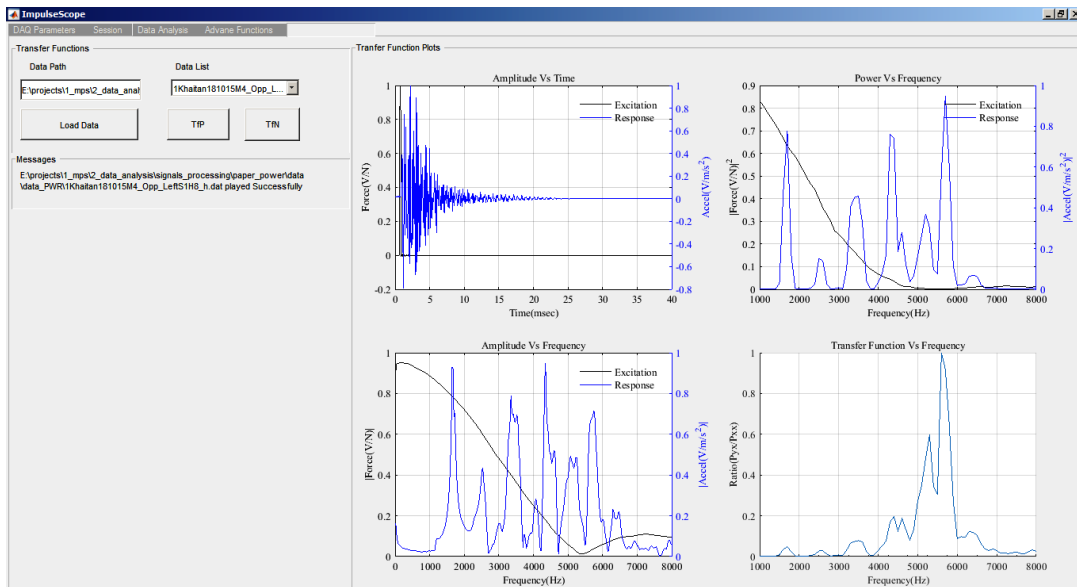


Figure 32: Frequency response function screen

4.7.6 Conclusion

In the market, available data acquisition and processing software are more efficient and user-friendly, but the user depends on the supplier for the customisation of the program for a new application. The purchase of software licenses is also very costly. Sometimes, it turns out a wrong decision when later found that it is not suitable for the planned research. This situation is not suitable for new research when things are not known in advance. The developed application is dedicated to impact-echo and response application for pre and post processing of excitation and response spectra. The application developed with the concern of expendable, cost, easy to use in field and translation of scripts in the executable for a stand-alone prototype for future use. The application has modular functions for the data acquisition and processing, a lot of functions can be customised and dedicated measurement can be built. The application has been used in research to collect data from field and post processing the same to develop the algorithm for flaw detection in dimensional stone blocks.

4.8 Prototype Instrument

4.8.1 Introduction

The main aim of the current research was to develop a portable, battery operated and low-cost instrument which can be used easily by semi-skilled persons in the gang saw and other places to identify the internal flaws, cracks, and fissures in dimensional blocks. To meet this goal, after studying of captured data from stone blocks and development of an algorithm to identify the anomaly in blocks using commercially available hardware and indigenous developed application with MATLAB, a prototype instrument has been designed. It is also used to collect the data from the field during research to validate its hardware and firmware and collected feedbacks and comments from targeted users of the product in the future.

4.8.2 Block Diagram of Prototype Instrument

A small hammer with steel round shape tip is used to generate the impulse transient signal. This impact generates a signal of 10 to 30 msec duration and maximum 5.0 kHz frequency. A piezoelectric accelerometer with charge output is used as the receiver. The data analyser has hardware and firmware that are necessary for signal acquisition, processing, displaying and communication of marble block impulse response data on USB. The instrument is composed of five different modules: a

control module, an acquisition module, a storage module, graphical user interface module, and power module. The block diagram of the prototype instrument is shown in Figure 33 and the photo of prototype instrument is shown in Figure 34.

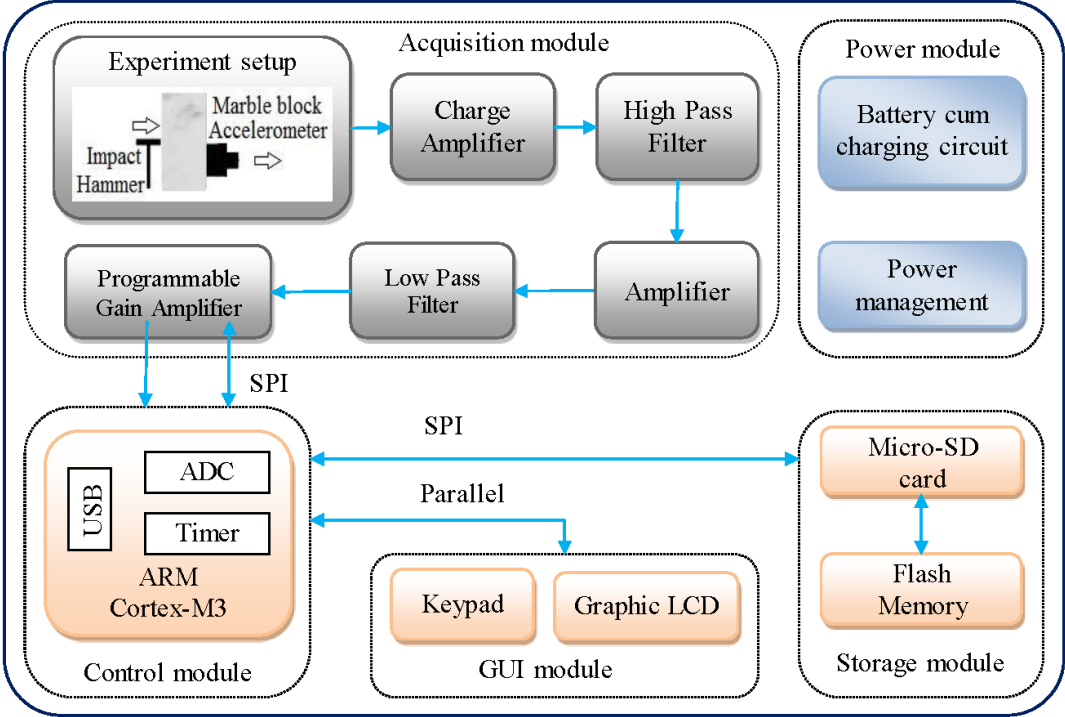


Figure 33: Block diagram of prototype instrument

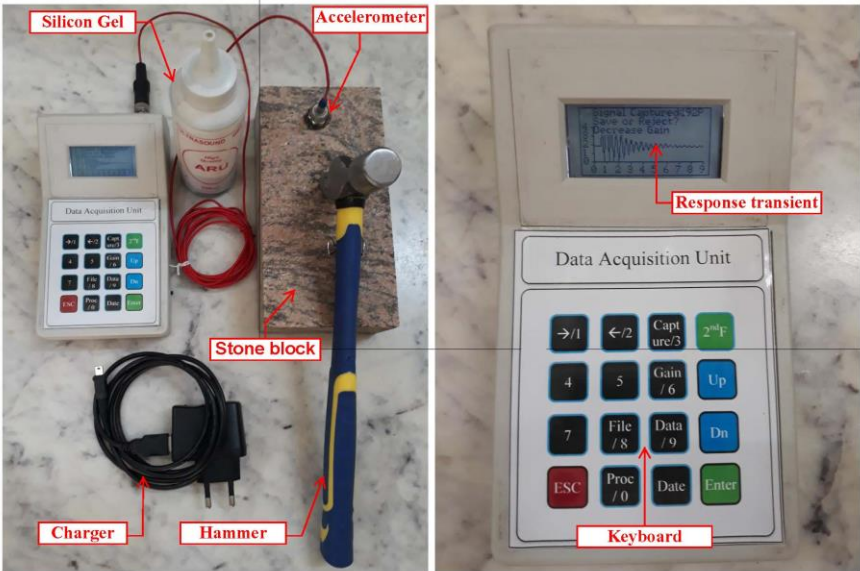


Figure 34: Photograph of prototype instrument

4.8.3 Control Module

The instrument is designed using a microcontroller, STM32L151 [69] from ST Microsystem, running at 24 MHz and inbuilt 384 KB of flash program memory, 48 KB of data RAM and 12 KB of non-volatile EEPROM. The STM32L151 controller performs data acquisition, storage, displaying, communication and processing. The data capturing is done with the help of a hardware timer at a fixed rate based on sampling rate selection.

During the process of vibration data acquisition, the STM32L151 controller handles the tasks of data collection, display, keypad and saving in RAM and Flash memory. A USB port is provided to download data to the computer for post-processing operation. The multiple tasks handling are done using a real-time kernel which makes sure that all the tasks are serviced without any lockup condition in a round robin method. The tasks of data acquisition handled by a hardware interrupt to avoid non-uniform sampling rate and data loss problems.

4.8.4 Acquisition Module

The acquisition module is the most critical of an analog instrument with respect to hardware and software design. It is the interface between the physical and digital world. While designing it, the balance between piezoelectric accelerometer output, input dynamic range of ADC, power supply voltage, power consumption, and noise are kept in mind to meet the implied requirements of long life and low weight of the instrument. These requirements are critical for a battery-operated device in the field due to limited availability of power source to recharge the instrument and to continue testing for a long duration.

The frequency response spectrum of the hammer with steel tip has a wide band with an upper range of 5 kHz. The problem of noise and false sample capturing has been addressed using the selectable trigger threshold level based on the condition of the object (stone block) under test. Major specifications of an acquisition module as shown in Table 11 below:

Table 11: Specifications of acquisition module

Parameter	Value
Sampling rates	8, 16 and 32 kHz
Amplifier gain	1, 2, 4, 5, 8, 10, 16, 32
Trigger threshold level	0.4, 0.6, 0.8 and 1.0 V
Pre-triggered points per sample	16, 23, 64 and 128
Total points per sample	512, 1024, 2048 and 4096
ADC input range	0 to 3.3V
ADC bits	12 bits

The acquisition module uses the STM32L151 controller's inbuilt ADC for conversion and it is 12 bits and supports conversion rate up to 1 Msps. The clipped signal detection algorithm has been implemented in software to take care the saturation limit of the analog section. The rail-to-rail input and output single power supply operational amplifier MCP6L91/94 [70] from Microchip has been used for charge amplifier, fixed gain amplifier, and low pass active filter. These amplifiers provide 10 MHz gain bandwidth product (GBWP), low input bias current of 1 pA, very high input impedance in order of 10^{13} ohms and 850 uA per amplifier quiescent current.

The internal hardware timer of the STM32L151 controller is used to periodically start the ADC conversion based on the sampling rate. The converted data is stored in RAM buffer for a single sample. It is checked for saturation limits of signal conditioner for clipping condition. Once the clipped free data are captured for a sample which includes pre and post triggered, the data buffer is copied to processing RAM buffer for display, store to non-volatile memory and further signal processing. While capturing the data of an event, if the clipping occurs for one data, the whole data buffer gets rejected and data acquisition module refreshed for the new acquiring process. The flow chart of data capturing from the accelerometer for the impact is shown in Figure 35.

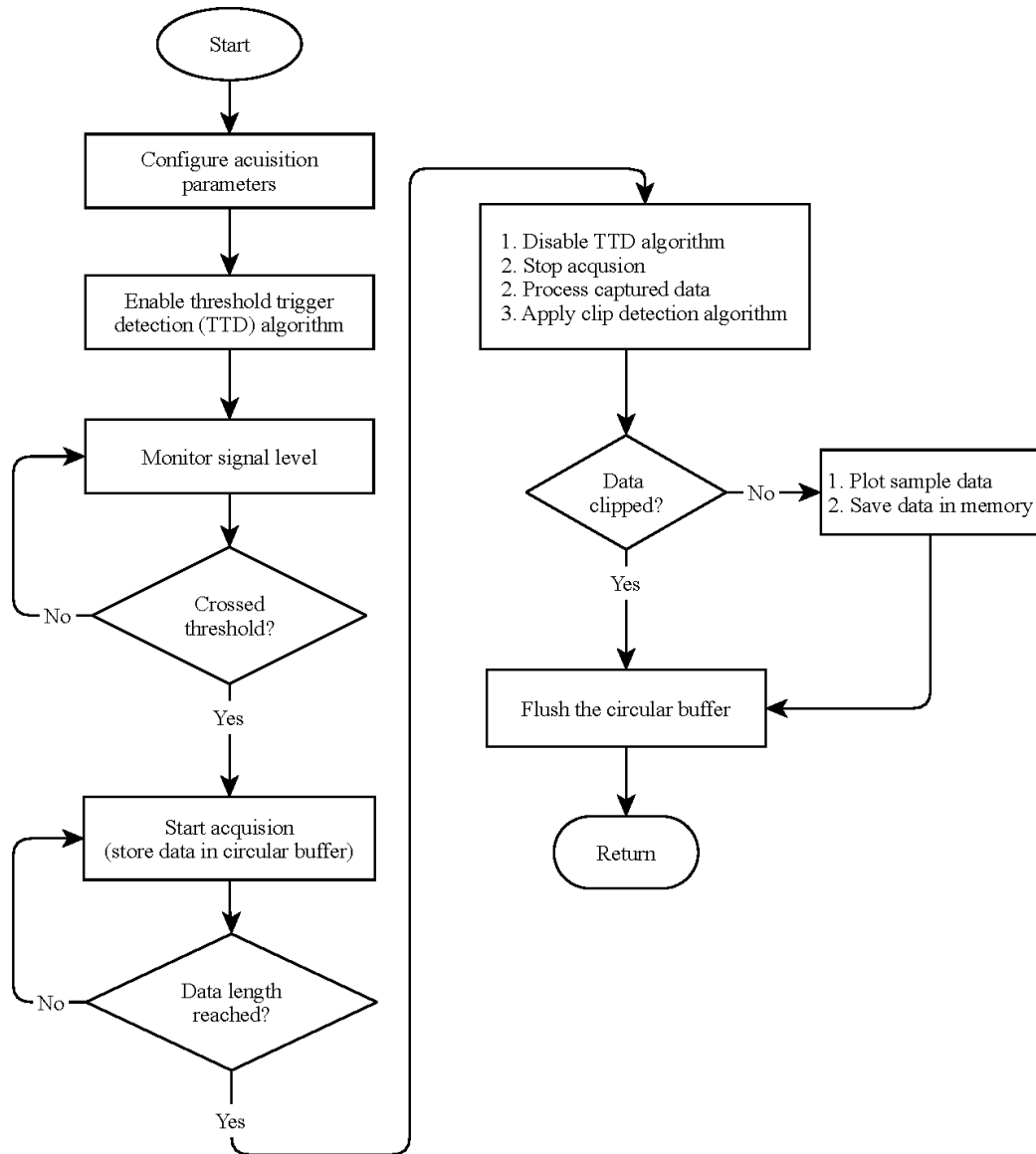


Figure 35: Flow chart of single impact data collection

4.8.5 Storage Module

The impulse response data need high resolution, a large number of data per impulse and high sampling rate. These samples are saved in a non-volatile serial NOR flash memory W25Q64 [71] from Winbond having a capacity of 8MB using embedded Flash File System FAT16 so that these sample data can be read as a file for each sample and can be replayed on a local display or can be sent to the computer via USB. The instrument also has provision for a 2 GB Micro-SD card as storage media to enhance the storage capacity if needed. Both the storage media are connected to control module via SPI bus. The instrument has provision for real time clock DS3231

[72] from Maxim and temperature sensor TCN75A [73] from Microchip and these are connected to control module via I2C bus.

4.8.6 Graphical User Interface Module

The device has 16 keys to support the functionality and selection of parameters, i.e. gain, sampling rate, data per sample, threshold level, and replay and upload of samples. The parameters are selected from drop down list to avoid any error in the entries. The numerical keypad is also included in setup configuration. The parameters, pop-up messages, results and impulse transient wave are displayed on monochrome graphic LCD 64128E (128x64) [74] from Displaytech. It is a low power COG module operating at 3.3V with internal contrast control and inbuilt-voltage generator for biasing. The LCD module is connected to control module with parallel interface.

4.8.7 Power Module

The instrument is powered by a 3.6V@1000 mAh rechargeable lithium-ion battery which is connected to a recharging circuit of MCP73811 [75] from Microchip. The battery can be charged through a USB port available on the instrument. The power module is using linear low voltage dropout regulator MCP1825 [76] from Microchip for regulation to sustain long duration. The L-C filters are used to remove noise from the power supply for analog circuits.

To extend the battery life of the instrument, it is equipped with low-power components with a sleep and wake up mode. The design strategy consists of three modes. The first mode is fully operational in which all components are working. In the second mode, the power switches off of the charge amplifier, programmable amplifier, and LCD backlight to reduce the power consumption when there is no data acquisition task. When the instrument does not receive any command from USB or key-pressing in a preset time period, the instrument goes to deep sleep and power off.

In order to estimate the average power consumption of different operation modes, the instrument is powered by a DC regulated power supply at 3.6V. The results of average current and power consumption are shown in Table 12. Since the capacity of the lithium battery selected is 1000 mA·h, the operation time of the instrument is evaluated and the results are given in Table 12. In the fully operational mode, the device can work continuously for about 10 hours. When all modules, enter sleep

mode, the current consumption is only 0.14 mA. Therefore, this sleep and wake up mode to help extend the life. These operational modes allow using limited available energy more efficiently.

Table 12: Power consumption test results of the device in different modes.

Operating mode	Current (mA)	Power (mW)	Life (hours)
Full operation	110	396	10
No data acquisition	32	115	34
All modules in sleep	0.14	0.50	7857

4.8.8 Conclusion

A portable prototype instrument for marble industries has been developed. Further refinement of firmware, hardware and visuals can be done in the professional model. There is a provision in the hardware and firmware for improvement of the product in future. This device with associated accessories is needed to carry out day to day testing in the field. A charger is needed to charge the device from AC mains. In future, it is proposed to modify the firmware for suitability of flaw characterization in all types of dimensional stone blocks in the field and provide enhancements and improvements.

4.9 Data Collection

The present research work involves correlation of defect with a pattern in the transient acoustic signals. Therefore, data have been collected for different purposes which include:

- Physical marble samples for marble density measurement
- Data for measuring the P-wave velocity in marbles
- Determining the discernible bandwidth of acoustic signal for diagnostic study
- Correlating anomalies in the blocks to various patterns in the acquired signal
- Collecting data by prototype device over known defects with an instrumented hammer with on-line processing logic for calibrating the prototype device

4.9.1 Capturing Impulse Response Data

The capturing and processing of data is done using MATLAB scripts. The signals are captured at a sampling rate of 25.6 kHz with 1024 sample points so as to provide sufficient resolution and time width to capture the entire transient signal. The impact hammer source was used with stainless steel tip which has a maximum frequency of 5.0 kHz, useable frequency cutoff with this setup is 3.7 kHz. Figure 36 shows the acceleration time histories of hammer impulse with 5.0 kHz tip for six stone blocks. In all these cases the captured signal dies within 20 ms. To satisfy the Nyquist criteria, the minimum sampling rate of 10.0 kHz is needed. To provide the best frequency resolution, the optimum sampling rate of 25.6 kHz is selected, keeping in mind the anti-aliasing cutoff frequency of the data acquisition module which is controlled by the sampling rate (i.e., $0.45 \times \text{sampling rate}$).

The MATLAB scripts are written to remove trending, noise, low pass filtering of signals, calculating amplitude and energy spectrum of impulse responses. In response spectrum, dominant peak frequencies and their amplitudes are measured, and band energy around these peaks is calculated. The different algorithms and signal processing techniques have been applied to the captured signals to correlate with known inherent defects in the material through which they have been passed.

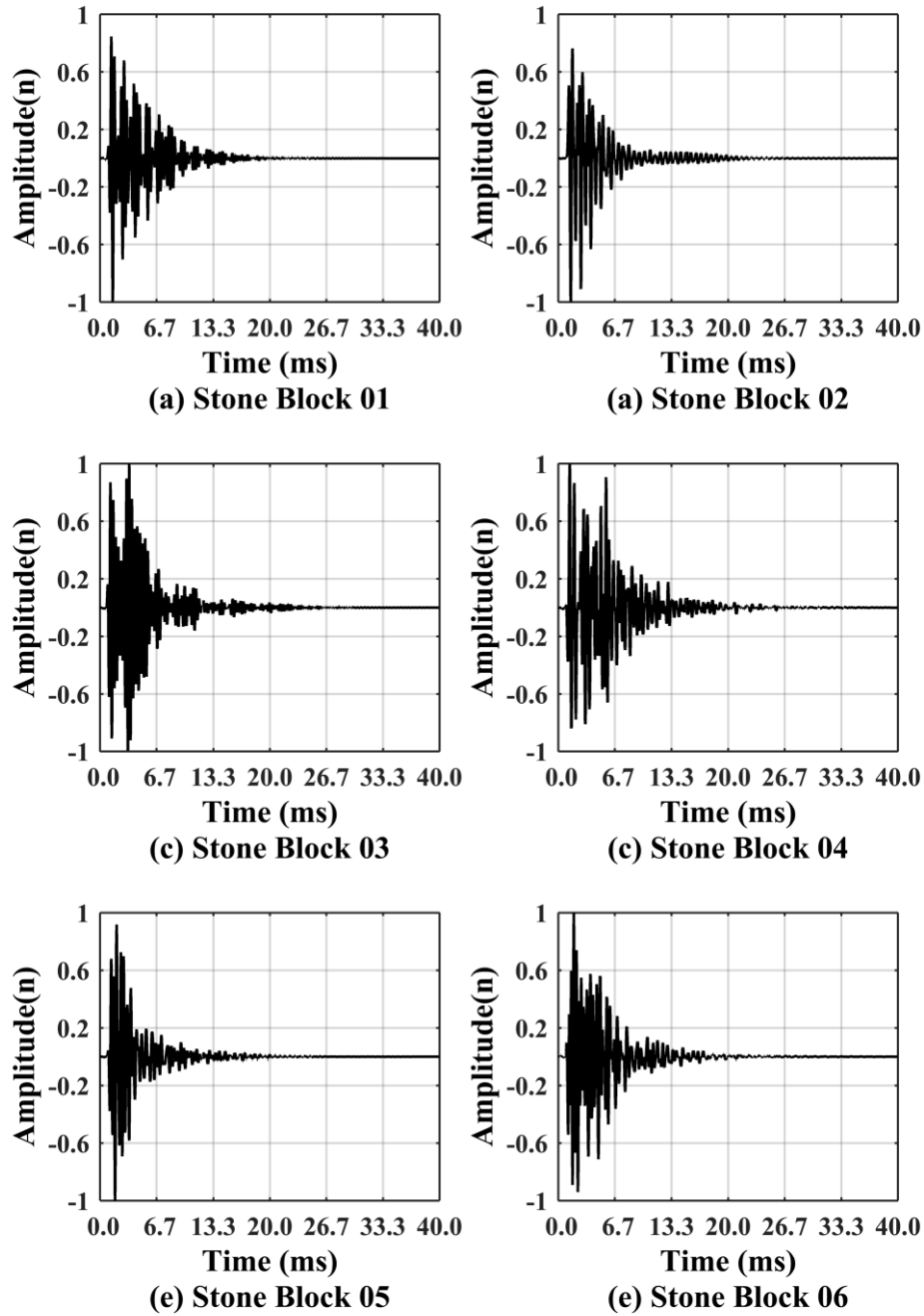


Figure 36: Acceleration time histories of the impact hammer impulse on dimensional stone blocks by an instrumented hammer with 5.0 kHz stain steel tip.

4.9.2 Measurement of P-wave Velocity

The velocity of P-wave in the marble blocks is not measured as per prescribed procedure for laboratories in standard method [77]. It is rather measured using an instrumented hammer with force sensor and accelerometer oriented on the dimensional stone indirect and semi-direct transmission configuration. The short

impulse wave is generated at one point by an instrumented hammer which is picked up by an accelerometer at another point. The schematic diagram of measurement setup is shown in Figure 37. The distance between impulse source and the receiver is calculated using trigonometric formulas after linear measurements with a measuring tape. The signals from both source and receiver transducers are recorded using NI-9234 DAQ module with the help of MATLAB scripts running on the Laptop. The travel time, ΔT , of P-waves between source and receiver is computed as the difference in time between the first arrivals of the pulses. With distance, ΔL , between the source and receiver computed earlier, the average speed, C_P , of the P-wave (source) is calculated by equation (37) as given below:

$$C_P = \frac{\Delta L}{\Delta T} \quad (37)$$

The P-wave velocity in marble thus calculated for two blocks are shown in Table 13. In each marble block, four readings have been taken from each source and receiver location to minimise the measurement errors. Similarly, eight measurements have been taken for different distance between source and receiver for the same block to get an average reading in the block. It is observed that there are variations in C_P values which could be due to two facts.

1. Variation in the source and receiver waveform for hits at the same point
2. Variation in the material properties in the path of wave propagation (for readings taken at multiple points)

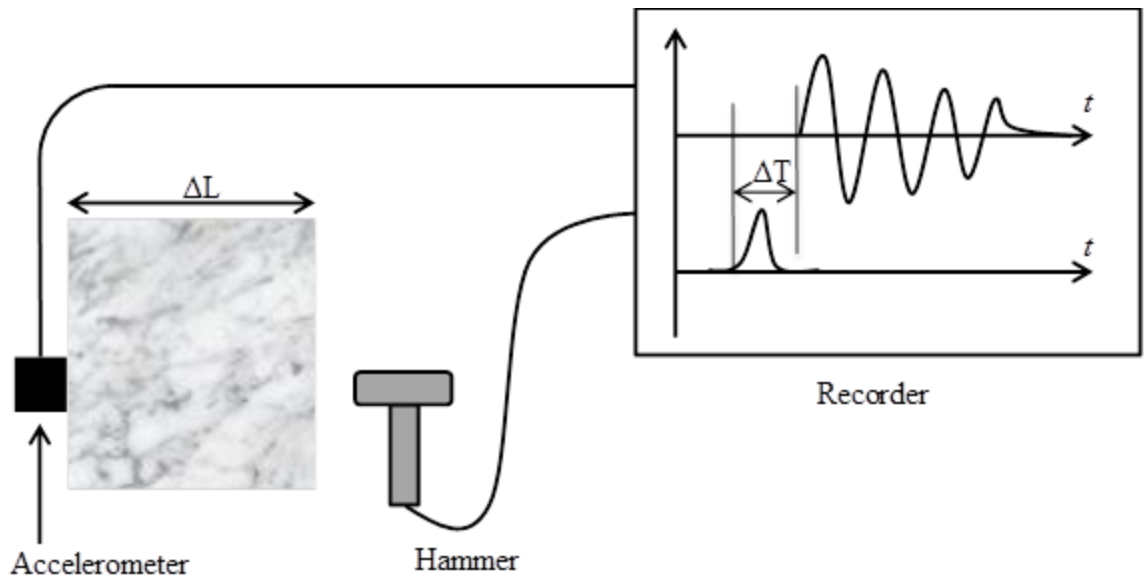


Figure 37: A schematic diagram for P-wave velocity measurement using direct transmission method [9, p. 11]

Table 13: P-wave velocity in marble block specimens

Block 1: Adanga marble of Aspur, Dungarpur, Rajasthan				Density of stone = 2.60		
Source - Receiver pair	Reading 1	Reading 2	Reading 3	Reading 4	Average (m/sec)	Average velocity in block (m/sec)
1	8453	6340	6340	6340	6868	5971
2	7478	4985	2991	4985	5110	
3	7153	7153	7153	7153	7153	
4	6340	5072	3623	3623	4665	
5	7478	4985	4985	4985	5608	
6	5364	5364	5364	5364	5364	
7	6502	6502	6502	6502	6502	
8	6502	6502	6502	6502	6502	
Block 2: Agaria marble of Agaria, Raj Samand, Rajasthan				Density of stone = 2.53		
1	6015	6015	6015	6015	6015	4915
2	4714	4714	4714	4714	4714	
3	4985	5982	4985	4985	5234	
4	5072	5072	5072	5072	5072	
5	4552	3641	4552	3641	4097	
6	4768	5722	5722	5722	5484	
7	3530	4942	4942	4942	4589	
8	3468	2601	5202	5202	4118	

4.9.3 Measurement of Density

The density of the material is one of the fundamental properties of geological materials. The density of the material has a direct bearing on the velocity of elastic wave propagation in that material. For marble stones, the density as specified in the literature ranges between 2400 to 2700 kg/m³ [21]. The density of marble is measured by taking the mass of samples using electronic analytical balance and measuring the volume of samples by water displaced in measuring jar. With these two values, the density is calculated as:

$$\text{density, } \rho = \frac{\text{weight}}{\text{volume}} \quad (38)$$

The density of two types of marble blocks has been calculated and their average values are shown in Table 14.

Table 14: Density of marble block specimens

Block 1: Adanga marble of Ashpur, Dungarpur, Rajasthan						
Sample No	Initial water level (ml)	Final water level (ml)	Volume (cm³)	Weight (grams)	Density (g/cm³)	Average density (kg/m³)
A	150	164	14	35	2.50	2600
B	150	176	26	70	2.69	
C	150	192	42	109	2.60	
D	150	206	56	146	2.60	
Block 2: Agaria marble from Agaria, Raj Samand, Rajasthan						
Sample No	Initial water level (ml)	Final water level (ml)	Volume (cm³)	Weight (grams)	Density (g/cm³)	Average density (kg/m³)
A	156	177	20	46	2.3	2530
B	156	188	32	82	2.56	
C	156	204	48	124	2.58	
D	156	216	60	161	2.68	

4.10 Dimensional Stone Details

Though this research work was aimed as classifying the dimensional stones in a generic way, more focus is laid on classifying the defects in marble blocks which are available in abundance in the study area. Therefore, most of the properties are listed for marbles and case studies with signal processing and defect detection refer to marble blocks of various sizes.

4.10.1 Defects in Marble Blocks

The common defects in marble blocks (also applicable in other dimensional stones too) include cracks, patches (or blotches), bands, lines, colour and pattern variations. The presence and size of these defects are used for classifying the quality grade of the blocks [78].

- **Crack** - Cracks are mainly caused by two reasons:
 - Natural cracks/fractures in the raw material itself present in-situ in the quarry
 - Man-made cracks inducing during faulty production and handling processes.
- **Patch** - It may or may not be the same colour as the stone, because of inherent properties present in the mineral deposits. It occurs because of natural causes and is uniquely characteristic in that particular Block.
- **Band** - It is a continuous patch, which runs along the surface of the slab. If the size of a patch exceeds 30 cm length and 2 cm width it is considered a band. The appearance of a band is like a thick line running across the surface of the slabs.
- **Line** - A line occurs because of inherent mineral properties in a slab. The size of a line can be 1-10 mm in thickness and 1 foot to 10 feet in length.
- **Colour variation** - is non-uniformity of the colour in a particular slab. It disturbs the pattern balance of the slabs. In certain cases, slabs appear two-toned.
- **Pattern variation** - the grain structure/pattern occurs in a way that appears contradictory to the accepted norms; it is termed as pattern variation.

In dimensional stone blocks, many of these defects play important role in increasing its beauty which adds to its market value. It is only the presence of cracks which acts as a villain and ruins the marketing potential of the block. Hence crack detection in dimensional stone blocks is chosen as the theme of the present research work.

4.10.2 Sizes of Dimensional Stone Block

The marble blocks have been selected from wide varieties available in local mandis (market). Block selection is based on the following:

- With and without defects
- Known and unknown defects
- Multiple types of dimensional stones from the different mining area
- Finished surface for mounting of the transducer (receiver)

Sizes of blocks varied from 0.8 to 1.8 m in width, 0.5 to 1.1 m in height and 0.6 to 1.6 m in depth. Thus, an average size of each block is roughly one cubic meter.

Chapter 5: Data Analysis

5. Data Analysis

The data analysis is divided into multiple phases to arrive at the results. The series of tests conducted prior to defect assessment to verify the data acquisition setup and identify the common problems at early stages. The MATLAB based “*ImpulseScope*” application developed to capture, store, and analyse data from the hammer and an accelerometer. The detailed description of this is given in previous section 4.7.

5.1 Repeatability

First, the repeatability tests were conducted with data acquisition hardware and software. For this purpose, several measurements were taken using same acquisition parameters: viz. hammer tip and the location of the impact and the receiver. It is found that the received signals are repeated for multiple instances.

Figure 38 shows plots of multiple hits of the instrumented hammer from the same point of the block. The left side of the figure is time plot, and the right side is their frequency spectrum. It is seen that both the hit time histories and their frequency spectra are similar, except first zero level amplitude reaching frequency. The small change occurs because of the variation in hit angle of the hammer tip on the surface of the block.

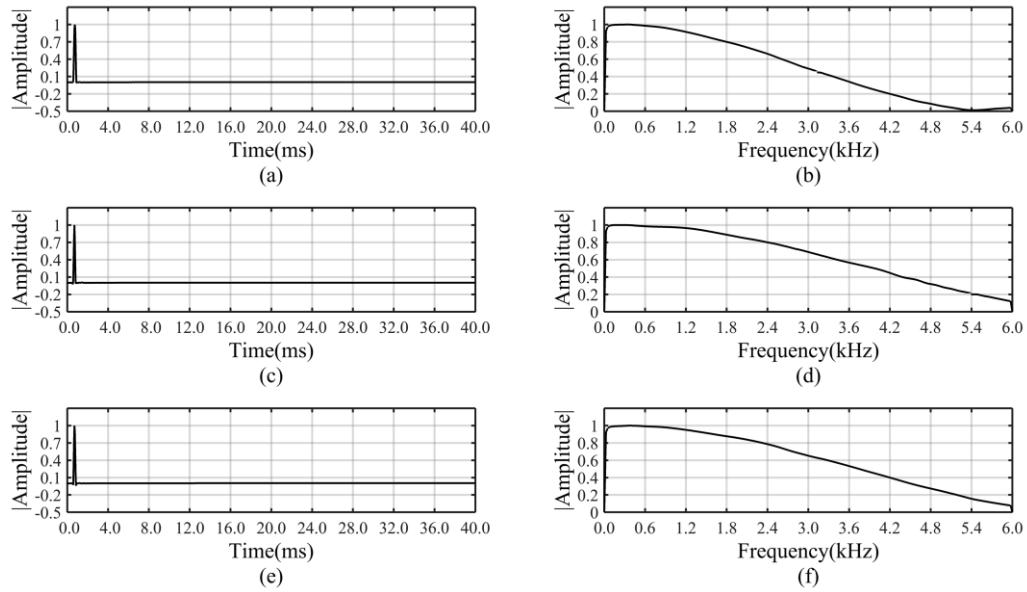


Figure 38: Time histories and amplitude spectra of instrumented hammer hits.

This variation does not pose any error as this is outside the domain of frequency limits chosen for further data analysis [79]. Figure 39 shows accelerometer plots of hits used in Figure 38. The left side of the figure is time plot, and the right side is their frequency spectrum. It is seen that both time histories and their frequency spectra for response are similar.

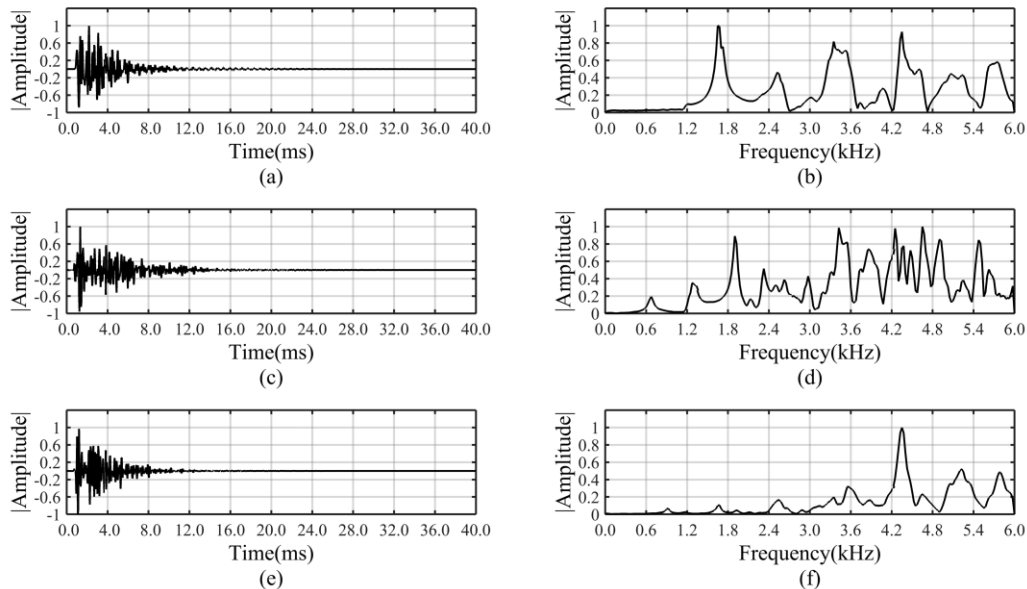


Figure 39: Time histories and amplitude spectra of the receiver with the same source and receiver points.

5.2 Signal Duration

Figure 40 shows the instrumented hammer contact time to surface of the block. It is zoomed scale of the Figure 38 (a). The measured hammer signal duration is 250 microsecond approximately. It depends on the hammer tip material and surface of the object under hit point. Angle of hammer impact reduces the contact area and lowers the signal amplitudes.

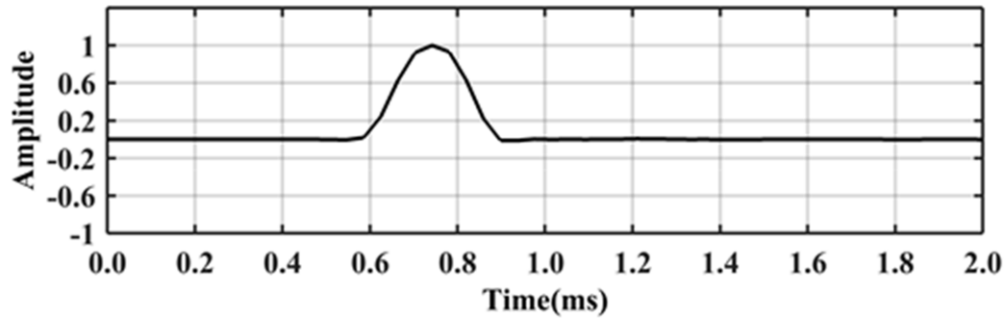


Figure 40: Hammer hit duration on the surface of the marble block with stainless steel tip (zoomed scale).

It is observed in all the readings of the crack and intact media between source and receiver using hits from the instrumented hammer, the receiver (accelerometer) signal diminishes well within 40 milliseconds. The actual duration of received signal depends on media condition between source and receiver points. Signal duration will be more for the softer (lesser density) medium as compared hard (higher density) medium. The selection of sampling rate and the number of samples per event are selected to capture the entire signal as specified in section 4.7.

5.3 Preliminary Spectral Analysis

5.3.1 Role of Impulse Hammer in Spectral Analysis

The conventional model testing is done by calculating the frequency response function (FRF) which is the ratio of the amplitude of the received signal to the input signal. With the data acquisition setup described earlier, the source and receiver data were collected from various marble blocks with and without a crack. Figure 41 (a) shows the time-histories of the hammer (dash red line) and the accelerometer (solid black line) and the corresponding amplitude spectra of these signals are shown in Figure 41 (b). The frequency spectrum of the hammer (dash line) has a maximum

value near to DC and decays to zero nearby 5.3 kHz. Figure 41 (c) shows the frequency response function (the ratio of the received spectrum to the source spectrum) which is conventionally used in the model analysis.

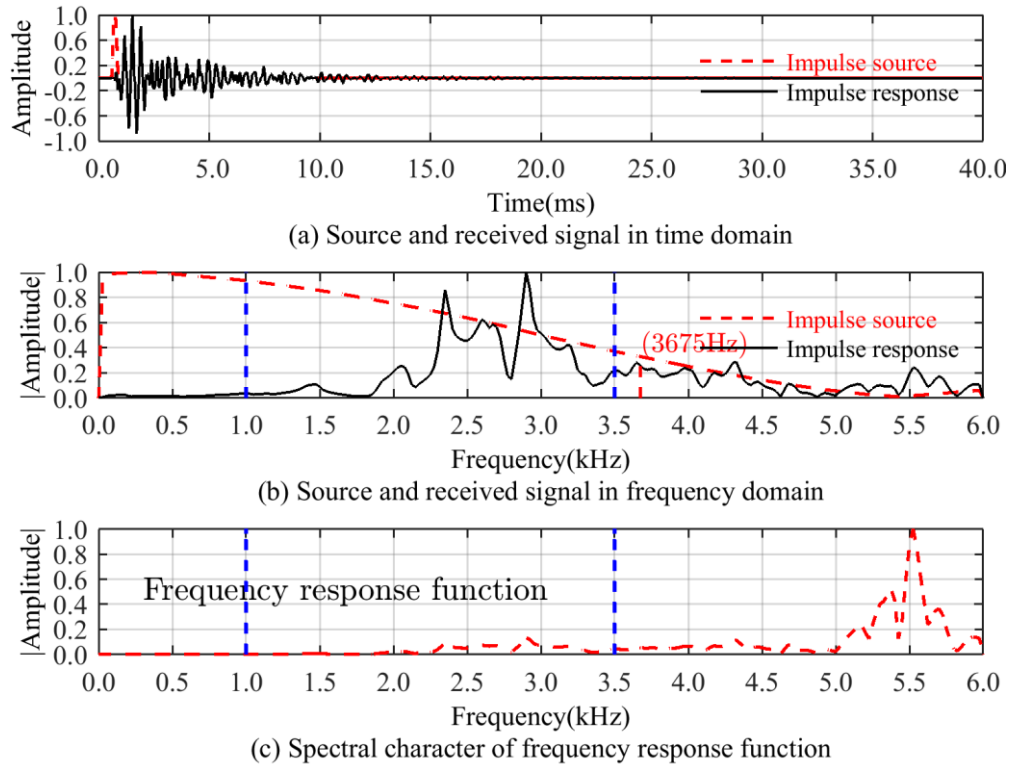


Figure 41: A normalised plot of the source and received signal in (a) time domain and (b) frequency domain. In plot (b), a red vertical line is at 10 dB (i.e., 0.32 of a unit) of the peak of the hammer signal (i.e. 3675Hz). The corresponding frequency response function is plotted in (c) above.

In order to analyse the role of the impulse hammer in generating the characteristic response signals, two spectra, as generated in Figure 41 (b) and (c) are compared. The following points are notable:

- The maximum usable frequency of selected hammer with a steel tip of 5.0 kHz is 3.5 kHz (3.675 kHz to be precise), which is 10 dB below the peak amplitude of the hammer. This has been found true for all the marble and granite stones tested during this research work [61, 62].
- Up to frequency range of 0.0 - 1.0 kHz, the spectrum of the received signal has the least variation and hovers around the zero magnitude. So, this range can be ignored while looking into any diagnostic pattern for the inherent defects.

- Between 1.0 - 3.5 kHz, the received signal has varying amplitude. The source signature too is stable in this region. This can be ascribed as the useful frequency range of impulse. This is shown between two blue dashed vertical lines in Figure 41 (b) and (c). The upper cutoff frequency is explained in forthcoming section 5.3.2.
- Within this frequency range, the spectral characteristic of both the receiver response and frequency response function is matching perfectly, i.e., two spectral plots have the same pattern, sans their amplitude as shown in the zoomed plots in Figure 42.

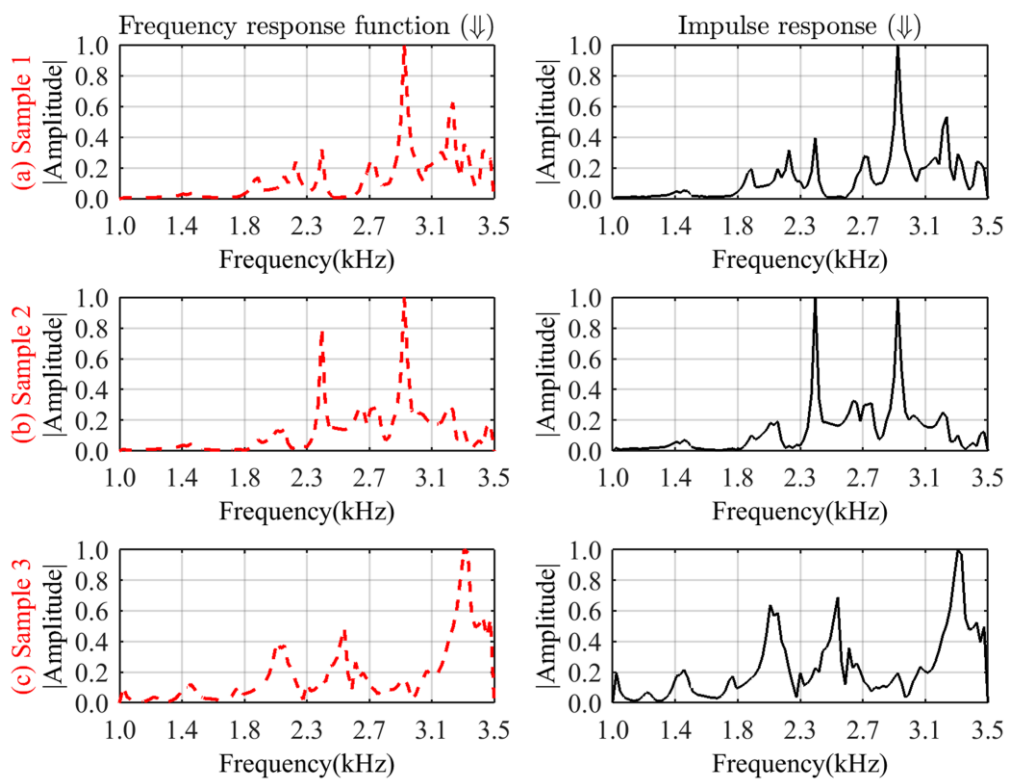


Figure 42: Frequency response function vs Standard spectral response (Spectrum of the received signal) plots for three samples. The first column shows the frequency response function and the second column shows the direct frequency spectrum of the received signal.

It is seen that the signal peaks and amplitude variation patterns in all these plots match perfectly in each sample's frequency response function and standard spectral response plots. Therefore, it can be derived from the above analysis that:

- The frequency response of the received signal carries the sufficient information to analyse the spectral characteristic which can be used in

diagnosing the pattern for identifying the defects in the travelled medium (dimensional stone block), and

- (ii) It is not necessary to calculate the FRF by the additional recording of the source signal because it does not provide any additional information for identifying the properties of the medium.

Thus, the recording of the force signal from the impact hammer's sensor is not necessary for the spectral characterization of the received signal. The impact hammer's tip merely plays its role in deciding the upper limit of the usable frequency range and provides the interested frequency range for the studies [79]. The selected spectral range must be well within the frequency range of hammer (source) within the flat band. Thus the spectral response spectrum alone can be used to develop the algorithm for identifying the defects in dimensional stone blocks. This eases the data capturing mechanism as well as simplifies further diagnostic analysis processes.

In case, if a low-frequency band is required for developing an algorithm for the inherent medium defect, a hammer with the blunt head or soft tip should be used [60, 61, 79].

5.3.2 Identification of Usable Frequency Band

With the data acquisition setup described earlier, the impulse hammer signals are collected from various marble blocks with and without cracks and their PSDs' plotted as shown in Figure 43. It is observed that:

- (i) The response spectrum does not have noticeable information in the frequency range of DC to 1.0 kHz. In some bigger blocks, it is seen that signal is also available below 1.0 kHz because of the natural frequency of system depends on the mass along with other physical parameters.
- (ii) Between 1.0 - 3.5 kHz, the received signal has sufficient information about the properties of the material. This region is also stable as per hammer signal analysis and its tip characteristics.

Thus, the range between 1.0 to 3.5 kHz is used for defect analysis in dimensional stone blocks. This can be ascribed as the useful frequency range of impulse for

dimensional stone blocks. Therefore, 3.5 kHz is selected as an upper cutoff frequency for the analysis purpose and the signal above 3.5 kHz is filtered out. Below this frequency, the source signal is also reasonably strong in order to adequately excite the test object and will provide better signal to noise ratio (SNR).

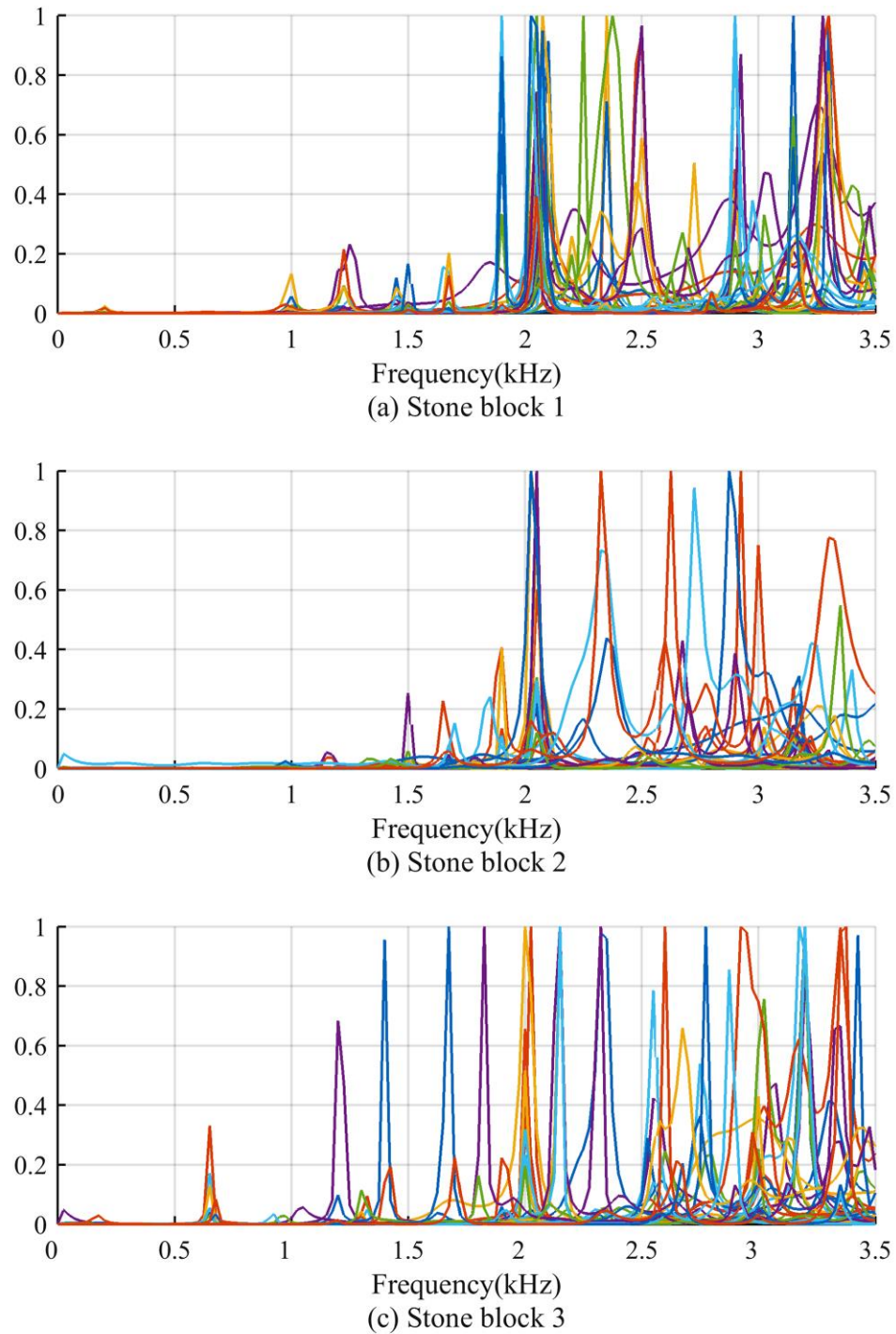


Figure 43: PSD plots of response signals in different marble blocks with common excitation force spectra.

In order to analyse the diagnostic signatures in the spectrum of the received signal, the usable spectral domain of 1.0 - 3.5 kHz is divided into three sub-bands. Selection of these three frequency bands is made based on observations of a series of data from various stone blocks. Following common facts were found during data analysis:

1. The spectrum of the received signals has two to four prominent peaks. In the majority of the cases (over 90%), the number of peaks is restricted to three.
2. The first peak was mostly observed around 1.2 - 1.7 kHz, the second peak was in the intermediate range within 2.2 – 2.8 kHz and the third peak was towards the end, i.e. above 3.0 kHz.
3. Hence it was decided to carry-out further analysis by dividing the usable spectral domain in three sub-bands. The range and nomenclature of the three bands so selected are:
 - a) Lower frequency band: 1.0 – 2.0 kHz
 - b) Middle frequency band: 2.0 – 3.0 kHz
 - c) Higher frequency band: above 3.0 kHz

Further behavioural analysis (both qualitative and quantitative) in terms of the diagnostic pattern for the presence of defects was carried out by comparative analysis of spectral signature in these three bands.

5.3.3 Suitable Power Spectral Density Estimation Methods

The signals of marble blocks for crack and intact media have been analysed using different PSD methods to identify suitable one. Table 15 shows the execution time taken by each PSD method for the individual signal as well as the average time of each method. It is found that PSD by the Periodogram with rectangular window is the fastest one and the Burg method takes the maximum time while calculating the PSD.

Table 15: Execution time of Different PSD algorithm (Calculated using a MATLAB script).

PSD method	Signal's execution Time (in ms) for samples (data property - 1024 points @25600Hz)									Av. time (ms)
	1	2	3	4	5	6	7	8	9	
Periodogram (Rectangular window)	1.10	0.34	0.34	0.68	0.50	0.50	0.70	0.50	0.67	0.59
Welch (Hamming)	12.2	16.0	15.8	16.5	15.9	15.7	16.6	16.2	15.3	15.6
Yule-walker	501	500	507	497	504	495	503	504	586	511
Burg	572	573	583	589	590	562	571	600	632	586

Figure 43 shows different parametric and non-parametric PSD method plots for the three signals. They are plotted with different scale factor for Y-axis for each PSD to avoid overlapping of plots on common axes. In non-parametric methods, the Welch method (hamming window with 50% overlap) is violent and peaks are not sharper whereas Periodogram method (Rectangular window, i.e. FFT) is smoother and peaks are also sharp. Further, within these two methods, the Periodogram with rectangular window has a higher peak resolution and it is also more appropriate for PSD estimation in battery operated devices because of lower processing required by it. For parametric methods, the Burg method gives better results compared to Yule-Walker because of sharper and identifiable peaks.

The following parameters are analysed to select the suitable method for MATLAB application on Laptop and handheld devices:

- Time taken to estimate the PSD
- The processing power needed to estimate the PSD
- Sharper identifiable peaks
- Resolution of peaks

Based on above parameters for different algorithms (parametric and non-parametric), the signals from dimension stone blocks for intact and cracked medium have been analysed. While comparing the results, it is found that the suitable methods are:

1. The Periodogram method with Rectangular window which is the most efficient in time and processing power. It provides sufficient information to interpret the

results and is suitable to implement in battery powered handheld instrument (proposed commercial diagnostic analogue is conceived as handheld one).

2. The Burg method which gives the best results in terms of identifiable well-separated spectral peaks, and higher resolution. It provides sufficient information to interpret the results with time limited data and used on laptop.

Thus, the impact transient signals from the dimensional stone block, being non-periodic and the limited length are analysed using the Burg method because of computationally efficient and a stable output model for the limited length of the data. It is concluded from Table 15 that the Periodogram method with Rectangular window for the battery operated handheld device and the Burg method for data analysis on the laptop are the suitable ones. They are selected for MATLAB application for determining the intactness of the dimensional stone blocks based on their accuracy of results and computational time needed by methods.

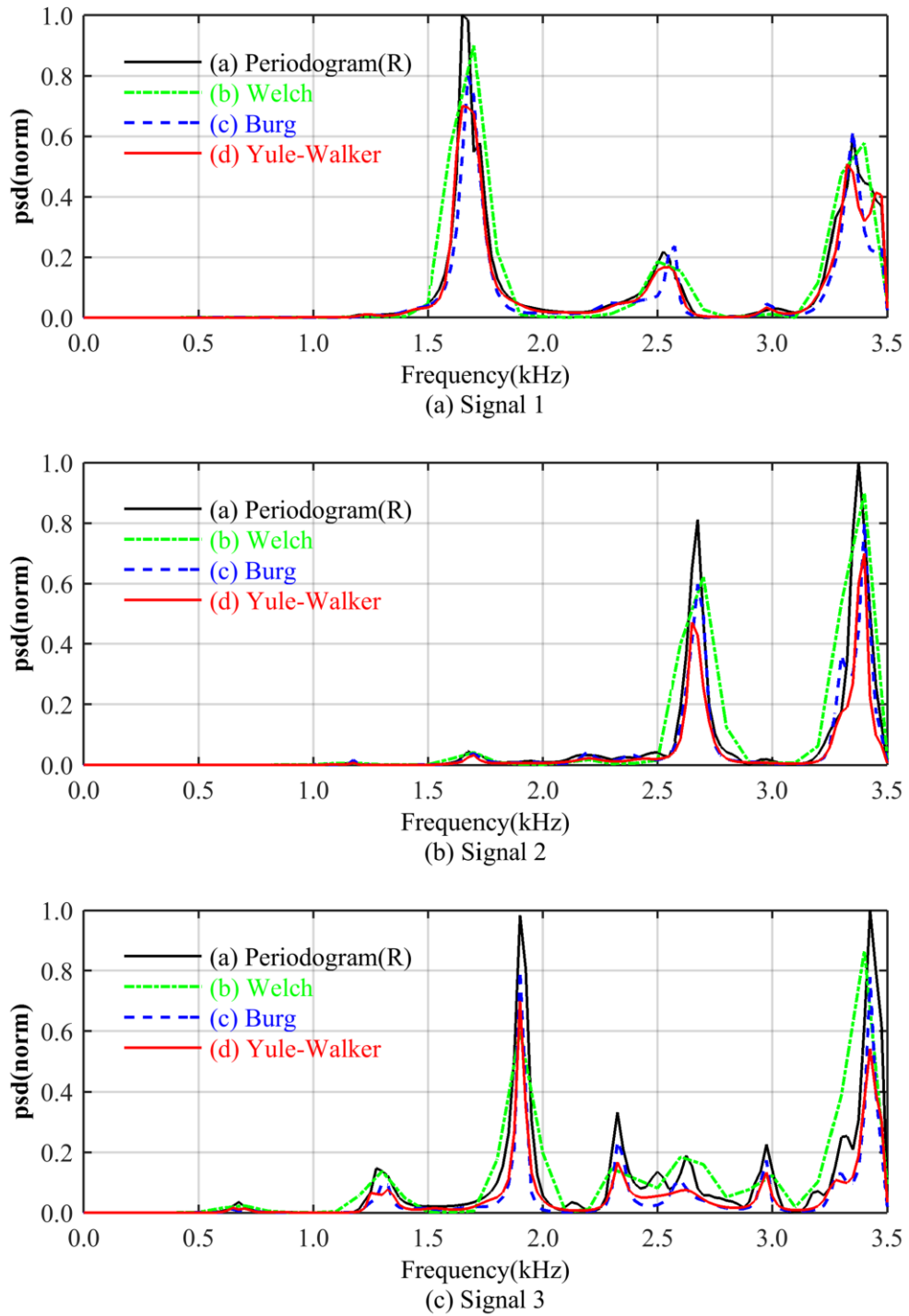


Figure 44: Estimation of PSDs of the marble block response signal using the Periodogram (Rectangular window), Welch, Burg and Yule-Walker method (different scale factor for each Y-axis to avoid overlapping of plots).

5.3.4 Defect Characterization of a Dimensional Stone Block

With the experimental data collected as explained in the previous sections, the resulting time-series data are processed in the frequency domain by calculating the

PSD by the Burg method. It is found that there is a consistency in the power spectral density of the received signal whenever there is a crack between the source and the receiver.

The Figure 45 shows the source frequency spectrum and received signal’s power spectral density estimation using the Burg method for intact and cracked medium between the source and receiver. They are plotted on a normalised scale in one graph for better visualisations. While selecting the peaks in power spectral density estimation plots, the following conditions are used:

- Frequency contents from 0.0 to 3.5 kHz have been selected.
- Band of ± 200 Hz is selected on both sides of the peak.
- The minimum separation between two peaks is 400 Hz, so as to avoid overlap.

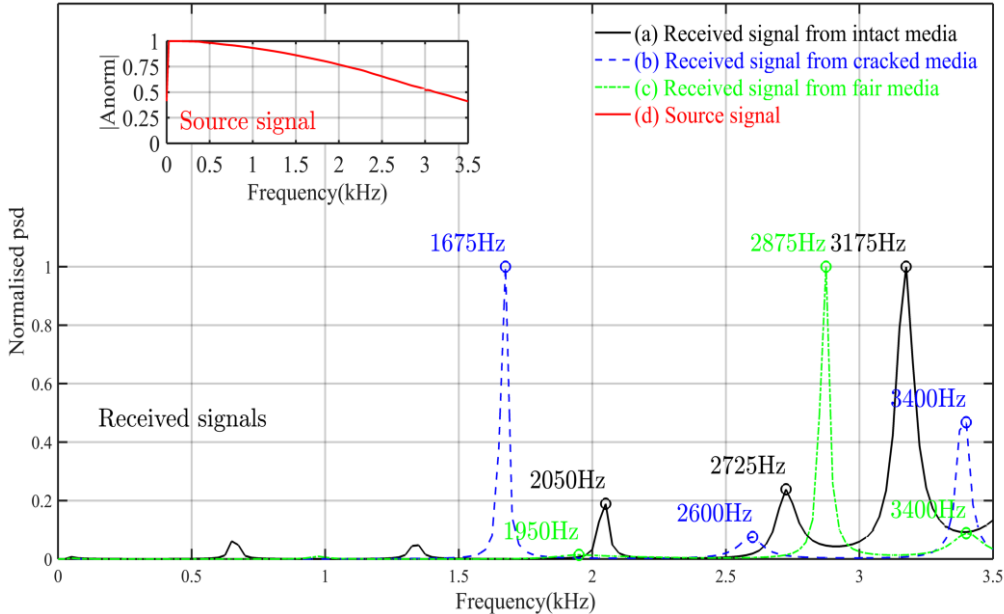


Figure 45: Frequency and Power spectral density estimation spectrum. (a) Source frequency spectrum (Red, inset plot). (b) Received signals from intact (solid black line), cracked (dash blue line) media between source and receiver and (c) fair (dot-dash green line) medium between source and receiver.

In the frequency band of interest between 1.0 – 3.5 kHz, there appears to be dispersion and redistribution of energies in PSD spectrum, as shown in Figure 45. Table 16 summarises the results in support of this claim.

Table 16: Peak frequencies, amplitudes, and PSD of bands for the intact and cracked medium

Medium between source and receiver	Frequency Bands ($\pm 200\text{Hz}$)					
	Peak Freq (Hz)			Peak Amp (normalise)		
	Low	Mid	High	Low	Mid	High
Intact	925	1925	2875	0.01	0.01	1.00
Crack	50	1675	2575	0.00	1.00	0.09
Fair	1950	2875	3400	0.01	1.0	0.09
	PSD			PSD (%)		
Intact	0.03	0.15	2.18	1	6	92
Crack	0.00	1.90	0.54	0	78	22
Fair	0.15	2.29	0.60	5	75	20

Two discernible features are consistently observed in the power spectrum density of the received signals:

- (1) Whenever, there is the presence of a crack between the source and the receiver points, a prominent portion of the energy is seen in the lower frequency region. The entire bandwidth of the received signal shrinks and all the peaks in the three bands move to a lower frequency side.
- (2) With intactness between the source and the receiver, most of the energy in the PSD spectrum is on the higher side of the spectrum compared to lower and middle bands.

Based on experimental analysis of spectral response data sets from various marble stone blocks of different characteristics, it is inferred that:

- (1) When a first dominant peak in spectral response lies above 3.0 kHz, the medium is intact.
- (2) When a first dominant peak in spectral response lies below 2.0 kHz, the medium has cracks. A defective medium has a prominent joint plane or open crack.
- (3) When the dominant peak lies between 2.0 kHz and 3.0 kHz, results are doubtful, sometimes there could be crack and other times, they are absent. We

called this situation as “*fair medium*” and further analysis is needed to draw the conclusion.

This consistency of pattern in the power spectrum density estimation of the received signal is explained in Table 17.

Table 17: Prominent diagnostic pattern in the spectral character

Medium between source and receiver	Spectral character
Intact	Peak above 3.0 kHz
Defect (crack)	Peak within 2.0 kHz
Inconclusive (Fair)	Peak between 2.0 to 3.0 kHz

For prominent peak in the frequency range of 2.0 to 3.0 kHz, the medium property is inconclusive. We have named this as a “*fair medium*” which could be due to the partial influence of crack in the transmission path. The second reason for a medium to be indexed as fair could be the presence of some other ambiguity like colour variation or intrusion. Such medium may result in damage during slicing or after prolonged use. Further studies are needed to discern the characteristics of a fair medium. That’s why we have listed this result as “*inconclusive*” in Table 17. On the contrary, a defective medium has a prominent joint plane or open crack and an intact medium has no crack. The presence of a defective medicum in confirmed in all cases where a middle band peak appears between 1500-2000Hz. This is adopted as the discriminant for the defect detection algorithm.

Thus, it is found that PSD spectrum has the diagnostic signature to identify the defects in the media. In the present study, the discernible frequency bandwidth to spot a defect is found between 1.0 – 3.5 kHz. This discernible bandwidth depends on the size of the dimensional stone block under test as well as the density of the medium and extent of the defect. It is essential that the source (impact hammer) should generate the transient signal with sufficient energy up to the discernible bandwidth of interest to adequately excite the test object under study.

5.4 Experimental Results of Various Dimensional Stone Blocks

5.4.1 Dimensional Stone Block 1 (Adanga Marble, Banswara)

Figure 46 shows the orientation of the sensor and hammer points to collect data from the marble stone block 1 which has front and top faces with the crack line (dark black). The hammer (H1 - H12) and accelerometer (S1 - S2) locations are marked on various faces — *S2, H6 and H7 are on the right face, H2 and H3 are on the left face, H4 and H5 are on the rear face of the block.* Table 18 lists the data collected with this setup for the various source-receiver (hammer-accelerometer) combinations. The last two columns of Table 18 list the media property between the hammer and accelerometer location identified using the algorithm described in Table 17 and actual observation of the block. Except, four cases where the presence of the crack between the source-receiver pair is identified as a fair medium (highlighted), all other results match with the actual situation. This gives the error margin of around 16.7% in the crack detection. It is important here to mention that the medium is classified as fair when neither the logic for the intact nor for the cracked medium is satisfied. This could be in a possible situation where a significant portion of crack is not encountered in the wave transmission path between the source and the receiver.

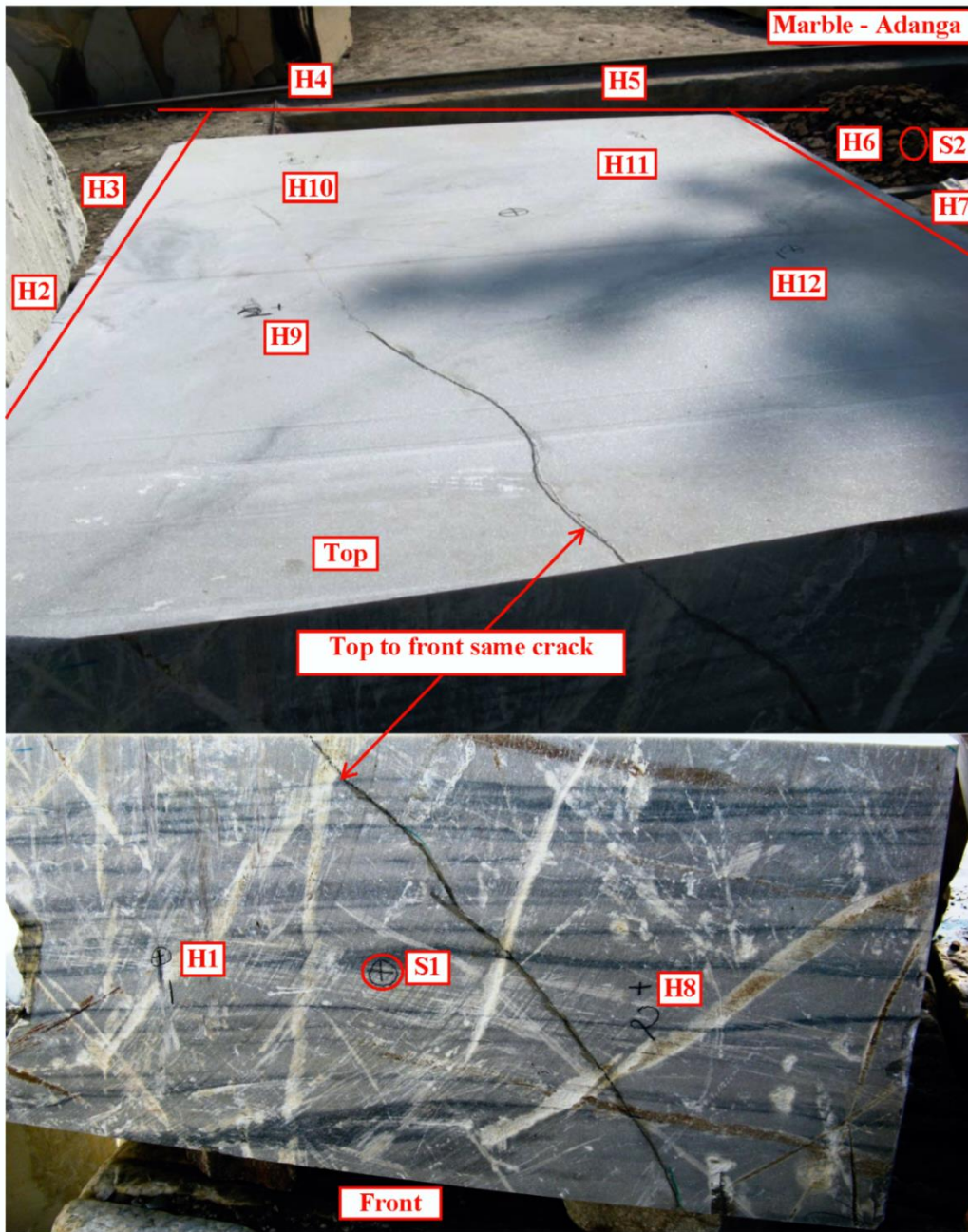


Figure 46: Face photos, hammer and accelerometer locations for stone block 1 (Adanga marble).

Table 18: Tabulation of various data for stone block 1 (Adanga marble).

Location: Aspur, Dungarpur					Trade name: Adanga			
Block size: 1.2x0.6x1.6m (WxHxD)					Density: 2600 kg/m ³			
Frequency bands: Low < 2.0 kHz, Mid 2.0 – 3.0 kHz and High > 3.0 kHz								
Sl. No	Source-receiver set-up	Signal Id	Peak Amp (norm)			Freq. band with highest peak	Conclusi on	Actual condition
			Low	Mid	High			
1	S1-H1	Adanga_01	0.17	0.58	1.00	High	Intact	Intact
2	S1-H2	Adanga_02	0.45	0.07	1.00	High	Intact	Intact
3	S1-H3	Adanga_03	0.02	1.00	0.54	Mid	Fair	Fair
4	S1-H4	Adanga_04	0.07	1.00	0.27	Mid	Fair	Crack
5	S1-H5	Adanga_05	1.00	0.21	0.16	Low	Crack	Crack
6	S1-H6	Adanga_06	1.00	0.29	0.26	Low	Crack	Crack
7	S1-H7	Adanga_07	1.00	0.29	0.19	Low	Crack	Crack
8	S1-H8	Adanga_08	1.00	0.56	0.45	Low	Crack	Crack
9	S1-H9	Adanga_09	0.02	1.00	0.32	Mid	Fair	Crack
10	S1-H10	Adanga_10	0.01	1.00	0.09	Mid	Fair	Crack
11	S1-H11	Adanga_11	1.00	0.31	0.32	Low	Crack	Crack
12	S1-H12	Adanga_12	1.00	0.27	0.00	Low	Crack	Crack
13	S2-H1	Adanga_13	1.00	0.09	0.54	Low	Crack	Crack
14	S2-H2	Adanga_14	1.00	0.03	0.15	Low	Crack	Crack
15	S2-H3	Adanga_15	0.04	1.00	0.09	Mid	Fair	Crack
16	S2-H4	Adanga_16	0.40	0.06	1.00	High	Intact	Intact
17	S2-H5	Adanga_17	0.02	0.46	1.00	High	Intact	Intact
18	S2-H6	Adanga_18	0.07	0.02	1.00	High	Intact	Intact
19	S2-H7	Adanga_19	0.11	0.06	1.00	High	Intact	Intact
20	S2-H8	Adanga_20	0.02	1.00	0.26	Mid	Fair	Fair
21	S2-H9	Adanga_21	1.00	0.76	0.14	Low	Crack	Crack
22	S2-H10	Adanga_22	0.01	1.00	0.05	Mid	Fair	Fair
23	S2-H11	Adanga_23	0.04	1.00	0.35	Mid	Fair	Fair
24	S2-H12	Adanga_24	0.01	1.00	0.09	Mid	Fair	Fair

Note: - In actual condition, the medium is designated as fair whenever the presence of the crack between source-receiver is doubtful. Out of 24 signals analysed with the suggested logic, there were only four instances of misinterpretation when the presence of a crack is not diagnosed properly. This sets the error margin of crack detection with the suggested logic as 16.7% approximately.

Figure 50 to Figure 53 (in Annexure) show the PSD estimation of these signals. Each figure has six PSDs subplots (a - f) - solid, dash-dot and dash-dash lines to show the intact, fair and crack medium respectively between source and receiver.

5.4.2 Dimensional Stone Block 2 (Arana Marble, Raj Samand)

Figure 47 shows the orientation of the sensor and hammer points to collect data from the marble stone block 2 which has front, left, and right faces with the crack line (dark black) on the left and the front corner area. Hammer (H1 - H12) and accelerometer (S1 - S3) locations are marked on these faces – *S1, H1, H8 and H9 are on the front face, S2 and H2 - H4 are on the left face, S3 and H5 - H7 are on the right face, and H10 - H12 are on the top face of the block.* Table 19 lists the data collected with this setup for the various source-receiver (hammer-accelerometer) combinations. The last two columns of Table 19 list the media property between the hammer and accelerometer location identified using the algorithm described in Table 17 and actual observation of the block. Except for two cases of the presence of the crack between the source-receiver pair which is identified as a fair medium (highlighted), all other results match with the actual situation. This gives the error margin of around 6.1% in the crack detection. The possible reason for a fair medium is explained earlier.

Figure 54 to Figure 59 (in Annexure) show the PSD estimation of these signals. Each figure has six PSDs subplots (a - f) - solid, dash-dot and dash-dash lines to show the intact, fair and crack medium respectively between source and receiver.



Figure 47: Face photos, hammer and accelerometer locations for stone block 2 (Arana marble).

Table 19: Tabulation of various data for stone block 2 (Arana marble).

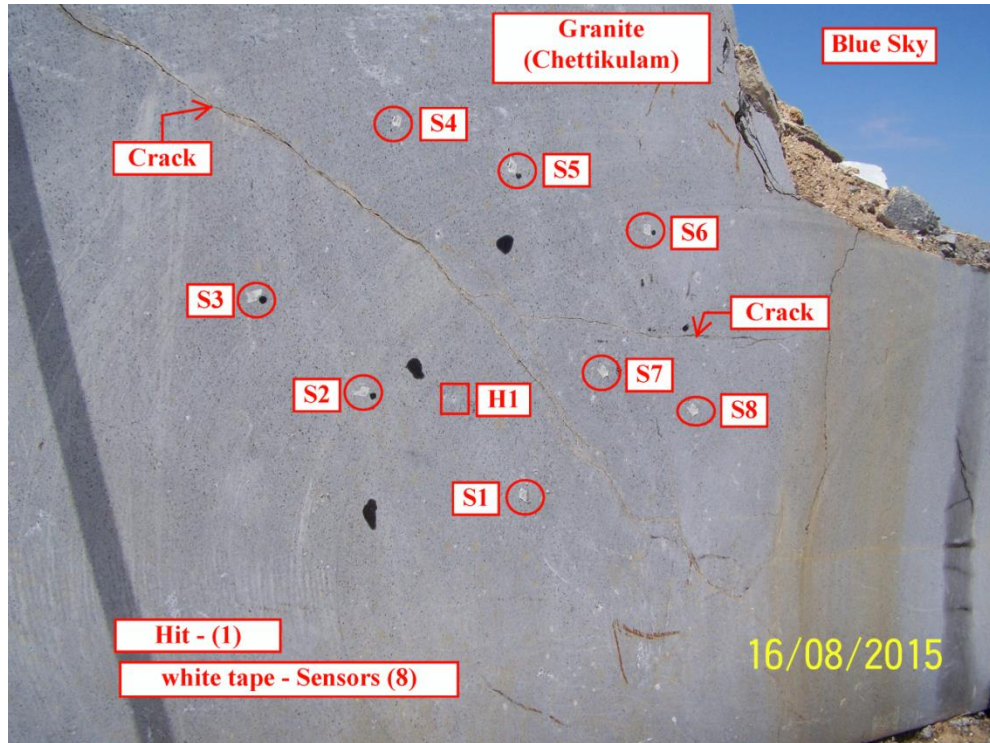
Location: Arana, Raj Samand						Trade name: Arana		
Block size: 1.1x0.7x1.4m (WxHxD)						Density: 2840 kg/m ³		
Frequency bands: Low < 2.0 kHz, Mid 2.0 – 3.0 kHz and High > 3.0 kHz								
Sl. No	Source-receiver set-up	Signal Id	Peak Amp (norm)			Freq. band with highest peak	Conclusi on	Actual condition
			Low	Mid	High			
1	S1-H1	Arana_01	1.00	0.01	0.09	Low	Crack	Crack
2	S1-H2	Arana_02	0.00	1.00	0.49	Low	Crack	Crack
3	S1-H3	Arana_03	0.07	0.02	1.00	Mid	Fair	Fair
4	S1-H4	Arana_04	0.15	1.00	0.11	Mid	Fair	Fair
5	S1-H5	Arana_05	0.00	0.06	1.00	High	Intact	Intact
6	S1-H6	Arana_06	0.09	1.00	0.85	Mid	Fair	Fair
7	S1-H7	Arana_07	0.00	0.01	1.00	High	Intact	Intact
8	S1-H8	Arana_08	0.00	0.05	1.00	Mid	Fair	Fair
9	S1-H10	Arana_09	0.00	0.17	1.00	Mid	Fair	Fair
10	S1-H11	Arana_10	0.01	0.02	1.00	Mid	Fair	Fair
11	S1-H12	Arana_11	0.01	0.10	1.00	Mid	Fair	Fair
12	S2-H1	Arana_12	1.00	0.01	0.28	Low	Crack	Crack
13	S2-H2	Arana_13	1.00	0.01	0.21	Low	Crack	Crack
14	S2-H4	Arana_14	0.00	0.02	1.00	Mid	Fair	Fair
15	S2-H5	Arana_15	0.45	1.00	0.07	Mid	Fair	Fair
16	S2-H6	Arana_16	0.00	0.00	1.00	Mid	Fair	Fair
17	S2-H7	Arana_17	0.01	0.01	1.00	Mid	Fair	Fair
18	S2-H8	Arana_18	0.00	0.16	1.00	Mid	Fair	Fair
19	S2-H9	Arana_19	0.05	1.00	0.03	Mid	Fair	Fair
20	S2-H10	Arana_20	0.00	0.28	1.00	Mid	Fair	Fair
21	S2-H11	Arana_21	0.00	0.21	1.00	Mid	Fair	Fair
22	S2-H12	Arana_22	0.00	0.22	1.00	Mid	Fair	Fair
23	S3-H1	Arana_23	0.01	1.00	0.89	Mid	<i>Fair</i>	<i>Crack</i>
24	S3-H2	Arana_24	0.00	0.75	1.00	Mid	<i>Fair</i>	<i>Crack</i>
25	S3-H3	Arana_25	0.00	1.00	0.03	Mid	Fair	Fair
26	S3-H4	Arana_26	0.00	0.39	1.00	Mid	Fair	Fair

27	S3-H5	Arana_27	0.00	0.01	1.00	Mid	Fair	Fair
28	S3-H7	Arana_28	0.02	0.33	1.00	Mid	Fair	Fair
29	S3-H8	Arana_29	0.27	1.00	0.02	Mid	Fair	Fair
30	S3-H9	Arana_30	0.00	0.01	1.00	High	Intact	Intact
31	S3-H10	Arana_31	0.08	0.11	1.00	High	Intact	Intact
32	S3-H11	Arana_32	0.00	0.06	1.00	Mid	Fair	Fair
33	S3-H12	Arana_33	0.60	1.00	0.05	Mid	Fair	Fair
<p><i>Note: - In actual condition, the medium is designated as fair whenever the presence of the crack between source-receiver is doubtful. Out of 33 signals analysed with the suggested logic, there were only two instances of misinterpretation when the presence of a crack is not diagnosed properly. This sets the error margin of crack detection with the suggested logic as 6.1% approximately.</i></p>								

5.4.3 Dimensional Stone Block 3 (Supreme Black Granite, Thirumalai)

Figure 48 shows the orientation of the sensor and hammer points to collect data from the granite stone block 3 which has a face with the crack line. It is a rock face in the granite mountain at the quarry site. The readings are taken in indirect transmission mode with the roving sensor. Hammer (H1) and accelerometer (S1 - S8) locations are marked on the face of the rock. Table 20 lists the data collected with this setup for the various source-receiver (hammer-accelerometer) combinations. The last two columns of Table 20 list the media property between the hammer and accelerometer location identified using the algorithm described in Table 17 and actual observation of the block. All results match with the actual situation.

Figure 60 to Figure 61 (in Annexure) show the PSD estimation of these signals. Each figure has six PSDs subplots (a - f) - solid, dash-dot and dash-dash lines to show the intact, fair and crack medium respectively between source and receiver.



[1] Figure 48: Face photos, hammer and accelerometer location for stone block 3 (Supreme black granite).

Table 20: Tabulation of various data for stone block 3 (Supreme black granite).

Location: Chettikulam, Thirumalai			Trade name: Supreme Black					
Block size: Rock face (Quarry site)			Density : 2840 kg/m ³					
Frequency bands: Low < 2.0 kHz, Mid 2.0 – 3.0 kHz and High > 3.0 kHz								
Sl. No	Source-receiver set-up	Signal Id	Peak Amp (norm)			Freq. band with highest peak	Conclussion	Actual condition
			Low	Mid	High			
1	H1-S1	Tml_01	0.48	0.00	1.00	High	Intact	Intact
2	H1-S2	Tml_02	0.15	0.00	1.00	High	Intact	Intact
3	H1-S3	Tml_03	0.41	0.00	1.00	High	Intact	Intact
4	H1-S4	Tml_04	1.00	0.74	0.00	Low	Crack	Crack
5	H1-S5	Tml_05	1.00	0.15	0.00	Low	Crack	Crack
6	H1-S6	Tml_06	1.00	0.00	0.41	Low	Crack	Crack
7	H1-S7	Tml_07	1.00	0.00	0.29	Low	Crack	Crack
8	H1-S8	Tml_08	1.00	0.06	0.00	Low	Crack	Crack

Note: - In actual condition, the medium is designated as fair whenever the presence of the crack between source-receiver is doubtful. Out of 8 signals analysed with the suggested logic, there were not any instances of misinterpretation.

5.4.4 Dimensional Stone Block 4 (Super White Marble, Vietnam)

Figure 49 shows the orientation of the sensor and hammer points to collect data from the marble stone block 4 with no visible cracks on it. Hammer (H1 - H11) and accelerometer (S1 - S2) locations are marked on these faces – of them S1, H1, H7 and H8 are on the front face, H2 and S2 are on the left face, H3 - H5 are on the rear face, H6 on the right face and H9 - H11 on the top face of the block. Table 21 lists the data collected with this setup for the various source-receiver (hammer-accelerometer) combinations. The last two columns of Table 21 list the media property between the hammer and accelerometer location identified using the algorithm described in Table 17 and actual observation of the block. All results match with the actual situation.

Figure 62 to Figure 65 (in Annexure) show the PSD estimation of these signals. Each figure has six PSDs subplots (a - f) - solid, dash-dot and dash-dash lines to show the intact, fair and crack medium respectively between source and receiver.



[2]

Figure 49: Face photos, hammer and accelerometer location for stone block 4 (Vietnam marble).

Table 21: Tabulation of various data for stone block 4 (Super white marble).

Location: Vietnam					Trade name: Super White			
Block size: 1.1x0.4x0.6m (WxHxD)					Density: 2960 kg/m ³			
Frequency bands: Low < 2.0 kHz, Mid 2.0 – 3.0 kHz and High > 3.0 kHz								
Sl. No	Source-receiver set-up	Signal Id	Peak Amp (norm)			Freq. band with highest peak	Conclusion	Actual condition
			Low	Mid	High			
1	S1-H1	Vietnam_01	0.03	0.05	1.00	High	Intact	Intact
2	S1-H2	Vietnam_02	0.05	1.00	0.56	Mid	Fair	Fair
3	S1-H3	Vietnam_03	0.26	0.00	1.00	High	Intact	Intact
4	S1-H4	Vietnam_04	0.00	0.00	1.00	High	Intact	Intact
5	S1-H5	Vietnam_05	0.01	1.00	0.87	Mid	Fair	Fair
6	S1-H6	Vietnam_06	0.18	1.00	0.14	Mid	Fair	Fair
7	S1-H7	Vietnam_07	0.00	1.00	0.00	Mid	Fair	Fair
8	S1-H9	Vietnam_08	0.13	0.00	1.00	High	Intact	Intact
9	S1-H10	Vietnam_09	0.00	0.02	1.00	High	Intact	Intact
10	S1-H11	Vietnam_10	1.00	0.22	0.00	Mid	Fair	Fair
11	S2-H1	Vietnam_11	0.18	0.03	1.00	High	Intact	Intact
12	S2-H3	Vietnam_12	0.00	0.06	1.00	High	Intact	Intact
13	S2-H4	Vietnam_13	0.00	0.68	1.00	High	Intact	Intact
14	S2-H5	Vietnam_14	0.00	0.00	1.00	Mid	Fair	Fair
15	S2-H6	Vietnam_15	0.00	1.00	0.02	Mid	Fair	Fair
16	S2-H7	Vietnam_16	0.00	0.10	1.00	High	Intact	Intact
17	S2-H8	Vietnam_17	0.20	1.00	0.24	Mid	Fair	Fair
18	S2-H9	Vietnam_18	0.01	0.02	1.00	High	Intact	Intact
19	S2-H10	Vietnam_19	0.12	1.00	0.04	Mid	Fair	Fair
20	S2-H11	Vietnam_20	0.01	1.00	0.56	Mid	Fair	Fair

Note: - In actual condition, the medium is designated as fair whenever the presence of the crack between source-receiver is not significant. Out of 20 signals analysed with the suggested logic, there were not any instances of misinterpretation.

Chapter 6: Conclusion and Future Work

6. Conclusions and Future Work

6.1 Contributions of Dissertation

The experimental results show that the response spectrum of the received impact signal transmitted across the dimensional stone block (marble) can be used to identify the defects independent of source spectrum provided the source signal spectrum has discernible energy distribution within the usable frequency band. Since an instrumented hammer is used in the present exercise, one has to ensure that the hammer's tip is capable of generating the maximum of the frequency range used which depends on tip material and its contact area with surface.

For the characterisation of internal defects, both parametric and nonparametric power spectral density estimation methods are applied to the responses of the transient impulse signals which passed through the stone blocks. The suitable power spectral density estimation methods to analyse the intactness of stone blocks have been identified for a handheld low power device. It is found that the estimation of power spectral densities using Periodogram with a rectangular window and autoregressive Burg methods are the suitable ones. While analysing the power spectral density estimation of these response signals, it is observed that redistribution of energy contents of the response signal depends on the intactness of the stone block. This information is used as the diagnostic signature for defect detection in the dimensional stone blocks and one prototype instrument and its firmware have been developed for data collection and defect identification.

This method has an edge over conventional impact-echo and ultrasonic methods on two counts:

1. This approach has a larger depth of investigation, and
2. This does not need a reference measurement from the similar intact material to compare.

The accuracy of the proposed method for the dimensional stone blocks is verified over a wide variety of marble and other dimensional stones, like granite and charnockites, both in-situ as well as at the gang-saw level. By analysis of a large

number of data samples of the dimensional stone blocks, it is observed that reliable signature of defects in blocks is available within 1.0 to 3.5 kHz for commonly available stone block sizes of a cubic meter or more at the gang saw.

Because of lesser computing power needed in execution, the Periodogram method is much easier to implement compared to the Burg method in a low power battery operated handheld device. One such prototype handheld model instrument is made incorporating the logic developed in this research work.

This work comprehensively describes how the impulse response of acoustic wave propagation can be used for defect characterisation in the dimensional stone blocks and lays the foundation for the measurement and analysis methods for a professional defect detection tool for the industry.

6.2 Future Work and Concluding Remarks

It is a crying need in the dimensional stone industry to have a device for commercial use in the field. If the prototype model developed under this research work is commercialised, it can be used to detect defects by a layman just by a hammer impact on the dimensional stone block and recording the signal on the opposite or adjacent face.

Further research is needed for ranging the defect, i.e., to find out the depth of defects from either surface. Rigorous field trials are needed on dimensional stone blocks to resolve the ambiguity issue when the first dominant peak lies in the middle band of spectral, i.e., 2.0 – 3.0 kHz. In our opinion, this happens when the transmission path does not occupy a significant portion of the defect under study.

With numerical simulations using finite element or boundary element method on a dimensional stone block with defects and its interaction with an incident transient signal, the impact of defects in the received signal can be analysed in various modes and possible discernible features can be seen at simulation stage. Such studies involving statistical energy analysis can increase the confidence on experimental results and or suggest some improvement in the defect detection algorithm for a better result. With further data-processing and developing a robust algorithm, it will be possible to develop a commercial device using the proposed method to identify the material defects for the dimensional stone industry.

Chapter 7: Annexures

7. Annexures

7.1 Plots of Power Spectral Density Estimation by Burg Method

7.1.1 Dimensional Stone Block 1 (Adanga Marble, Banswara)

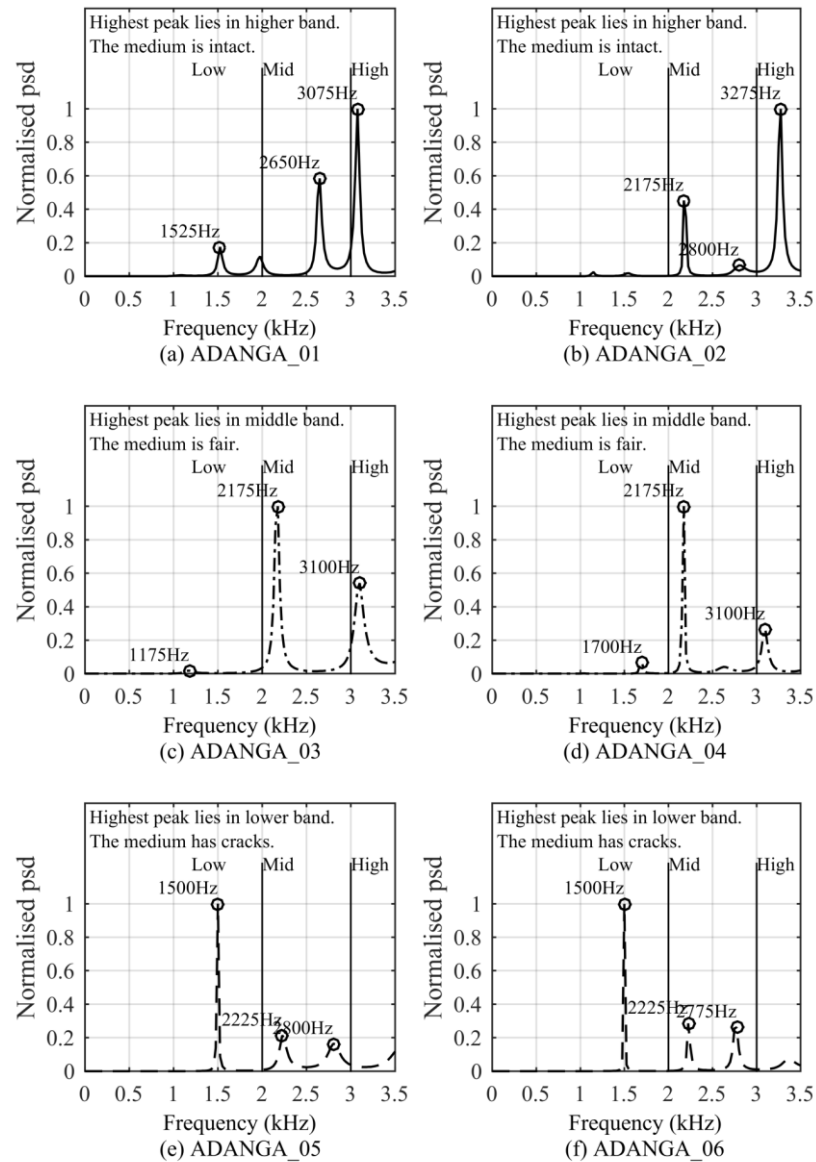


Figure 50: PSD plot showing peak locations and crack detection logic for signal 1 to 6 of marble block 1.

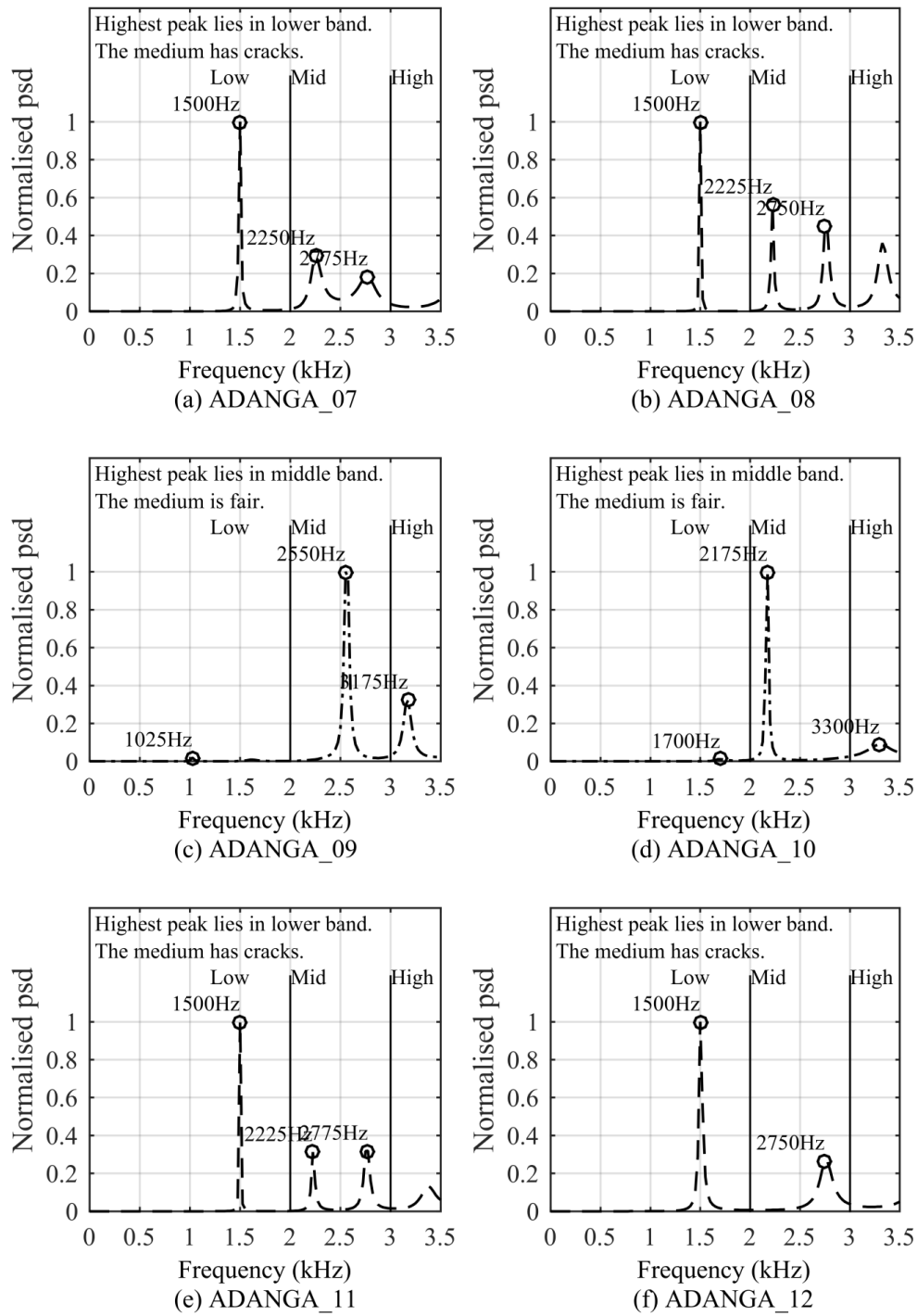


Figure 51: PSD plot showing peak locations and crack detection logic for signal 7 to 12 of marble block 1

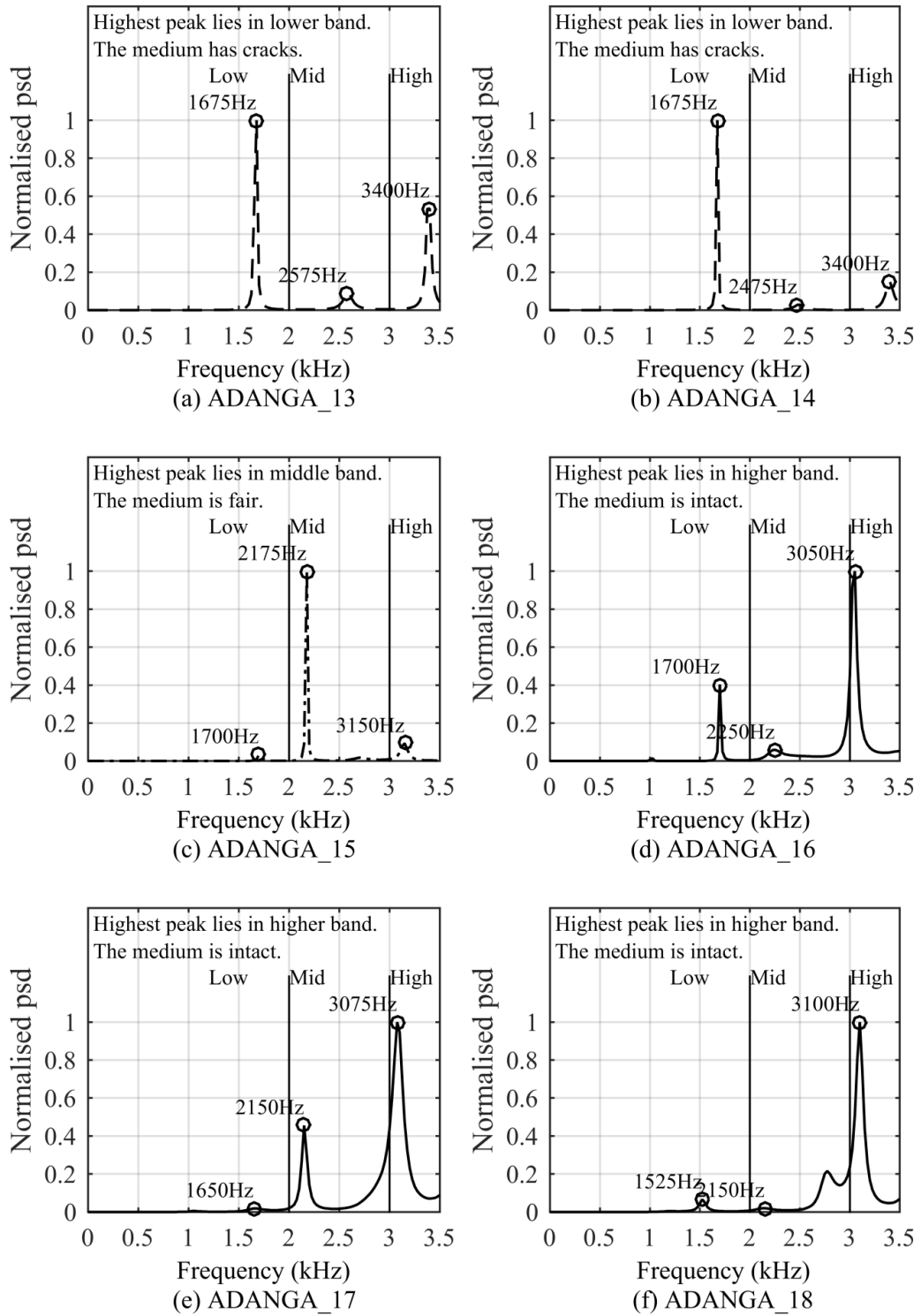


Figure 52: PSD plot showing peak locations and crack detection logic for signal 13 to 18 of marble block 1.

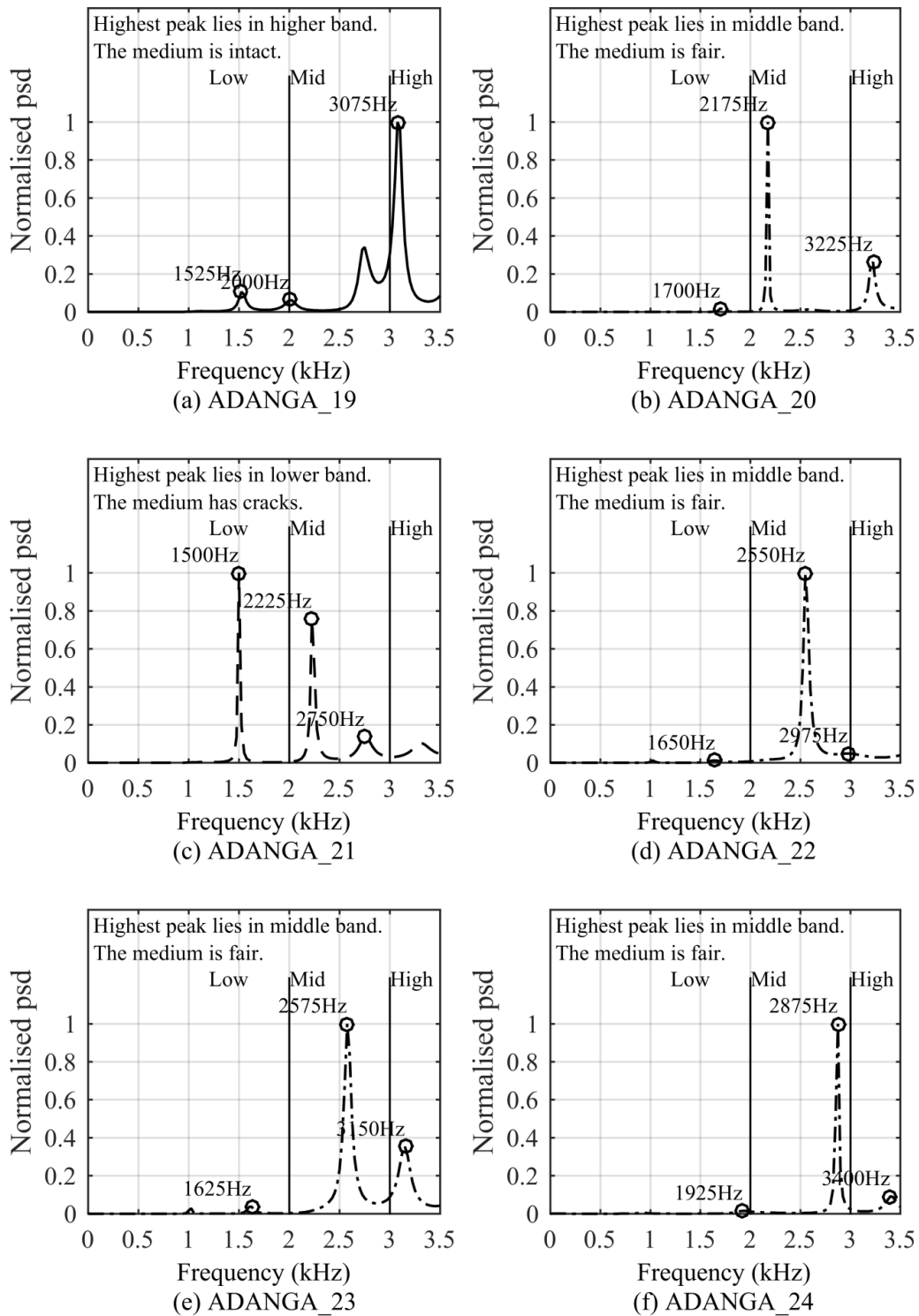


Figure 53: PSD plot showing peak locations and crack detection logic for signal 19 to 24 of marble block 1.

7.1.2 Dimensional Stone Block 2 (Arana Marble, Raj Samand)

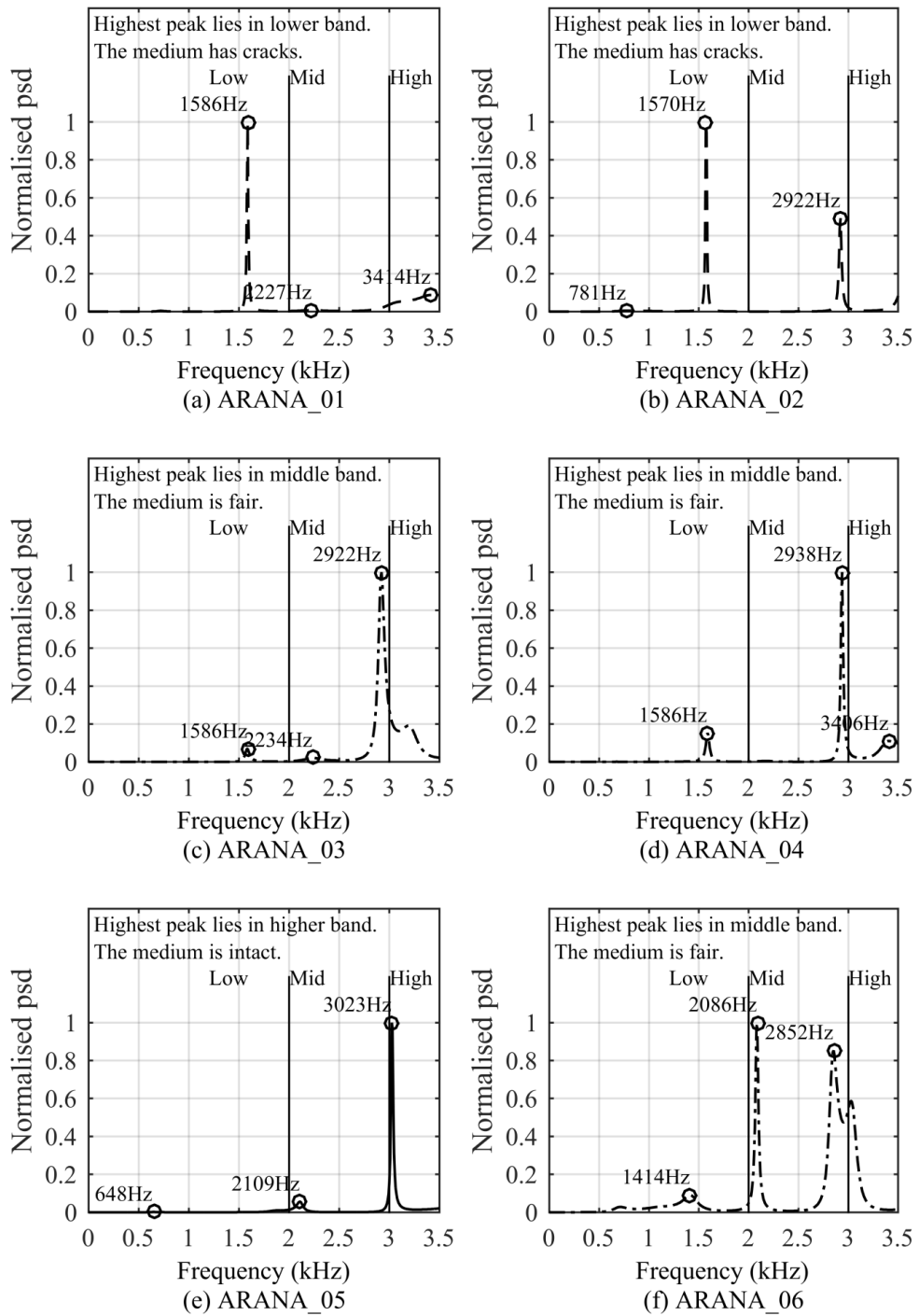


Figure 54: PSD plot showing peak locations and crack detection logic for signal 1 to 6 of marble block 2.

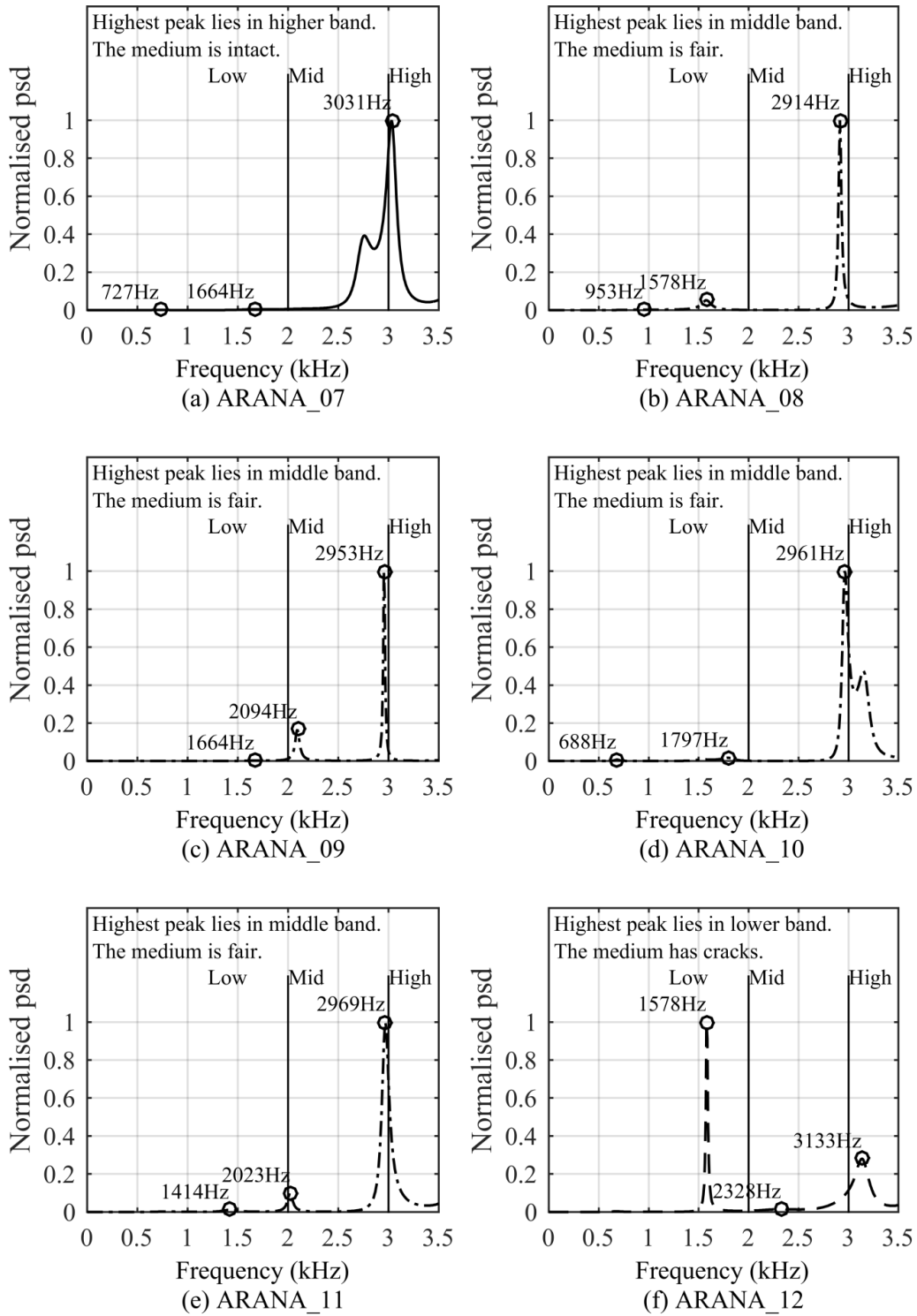


Figure 55: PSD plot showing peak locations and crack detection logic for signal 7 to 12 of marble block 2

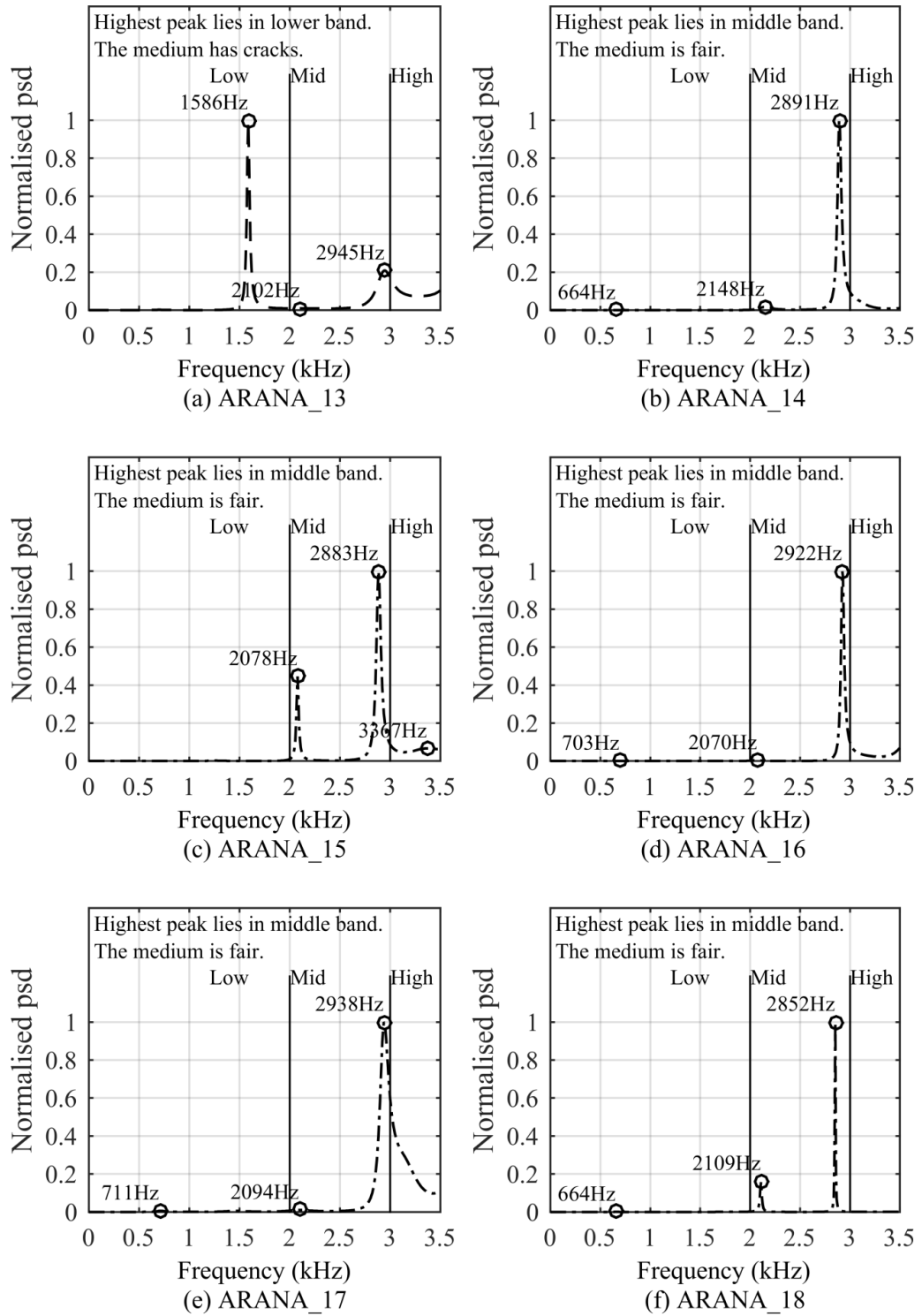


Figure 56: PSD plot showing peak locations and crack detection logic for signal 13 to 18 of marble block 2.

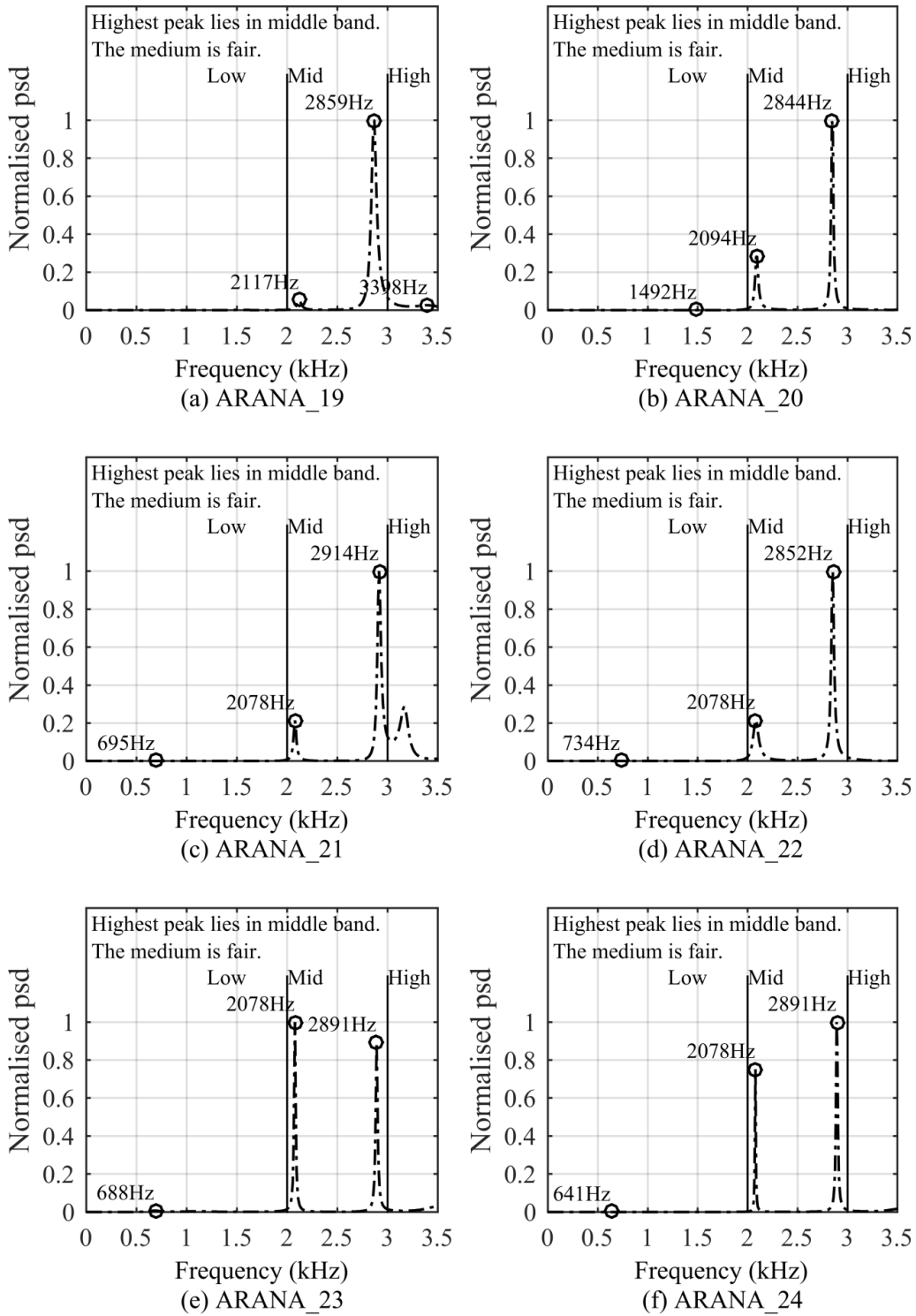


Figure 57: PSD plot showing peak locations and crack detection logic for signal 19 to 24 of marble block 2.

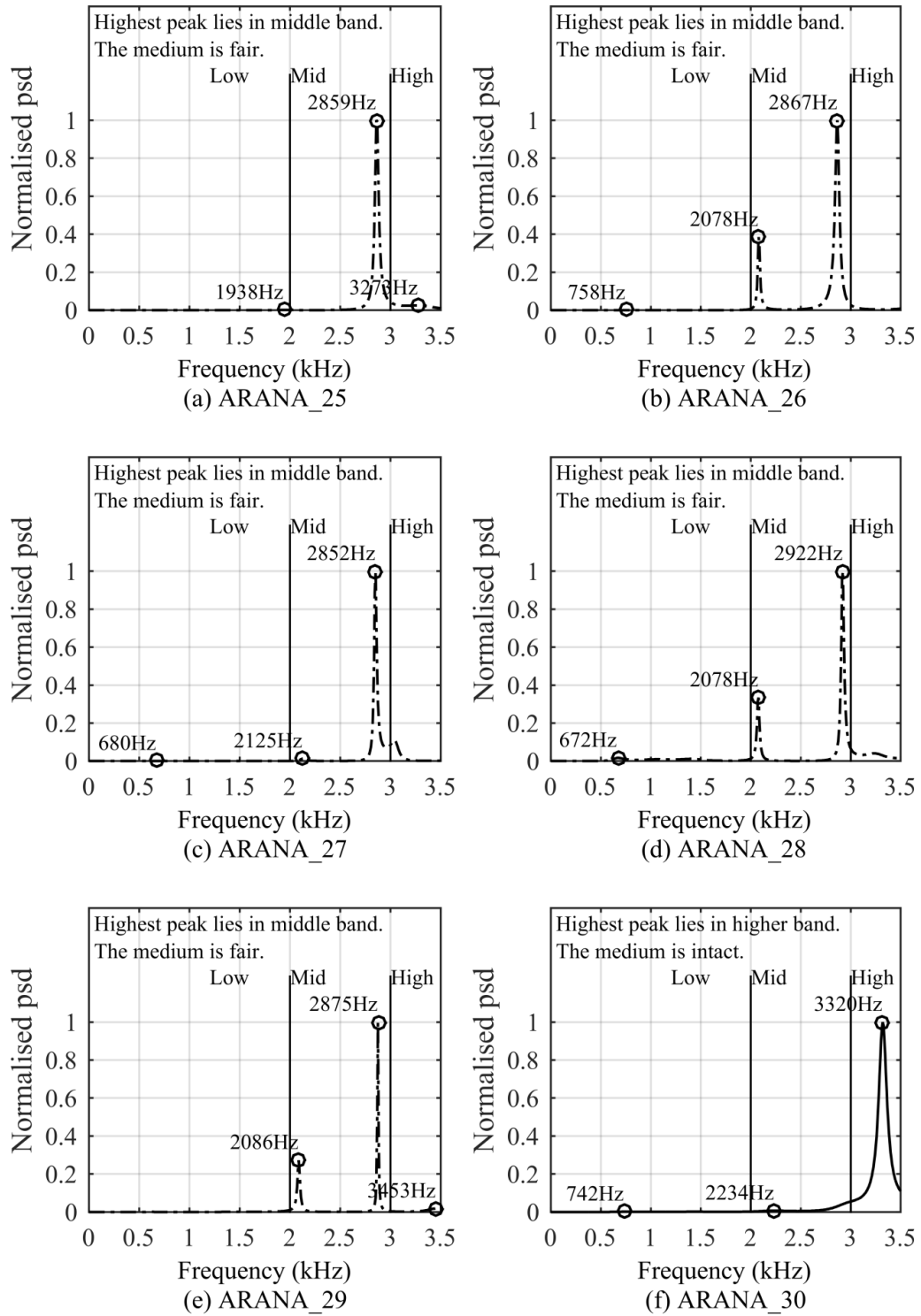


Figure 58: PSD plot showing peak locations and crack detection logic for signal 25 to 30 of marble block 2.

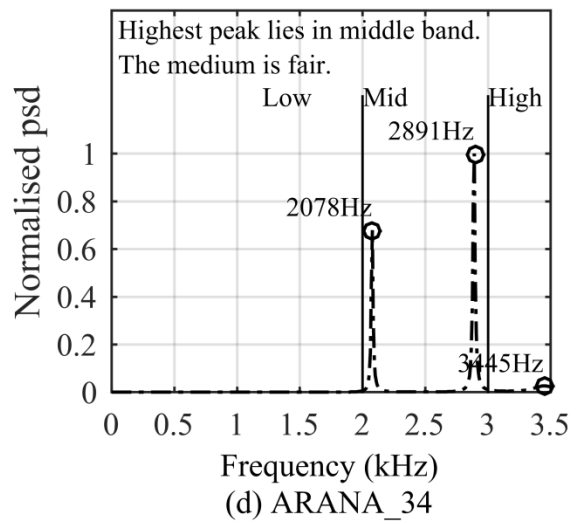
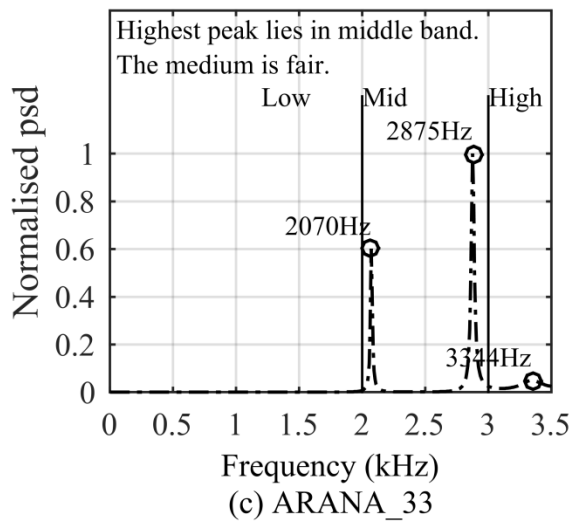
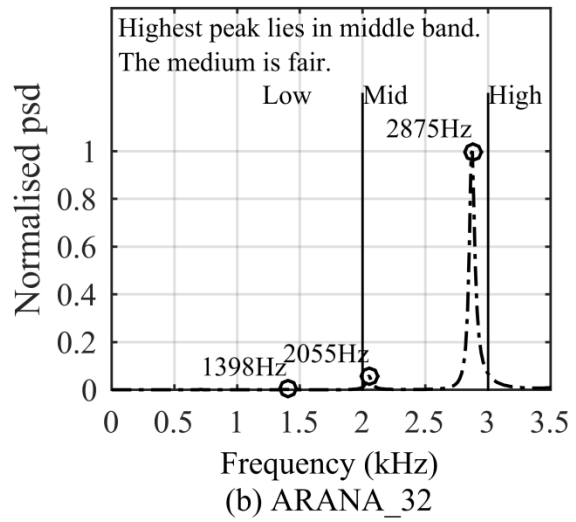
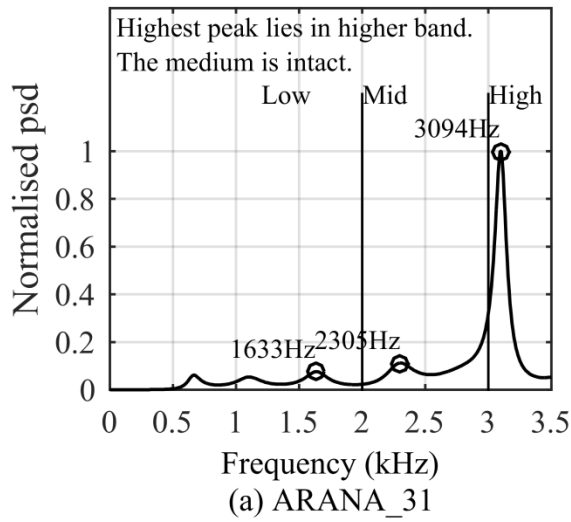


Figure 59: PSD plot showing peak locations and crack detection logic for signal 31 to 33 of marble block 2.

7.1.3 Dimensional Stone Block 3 (Supreme Black Granite, Thirumalai)

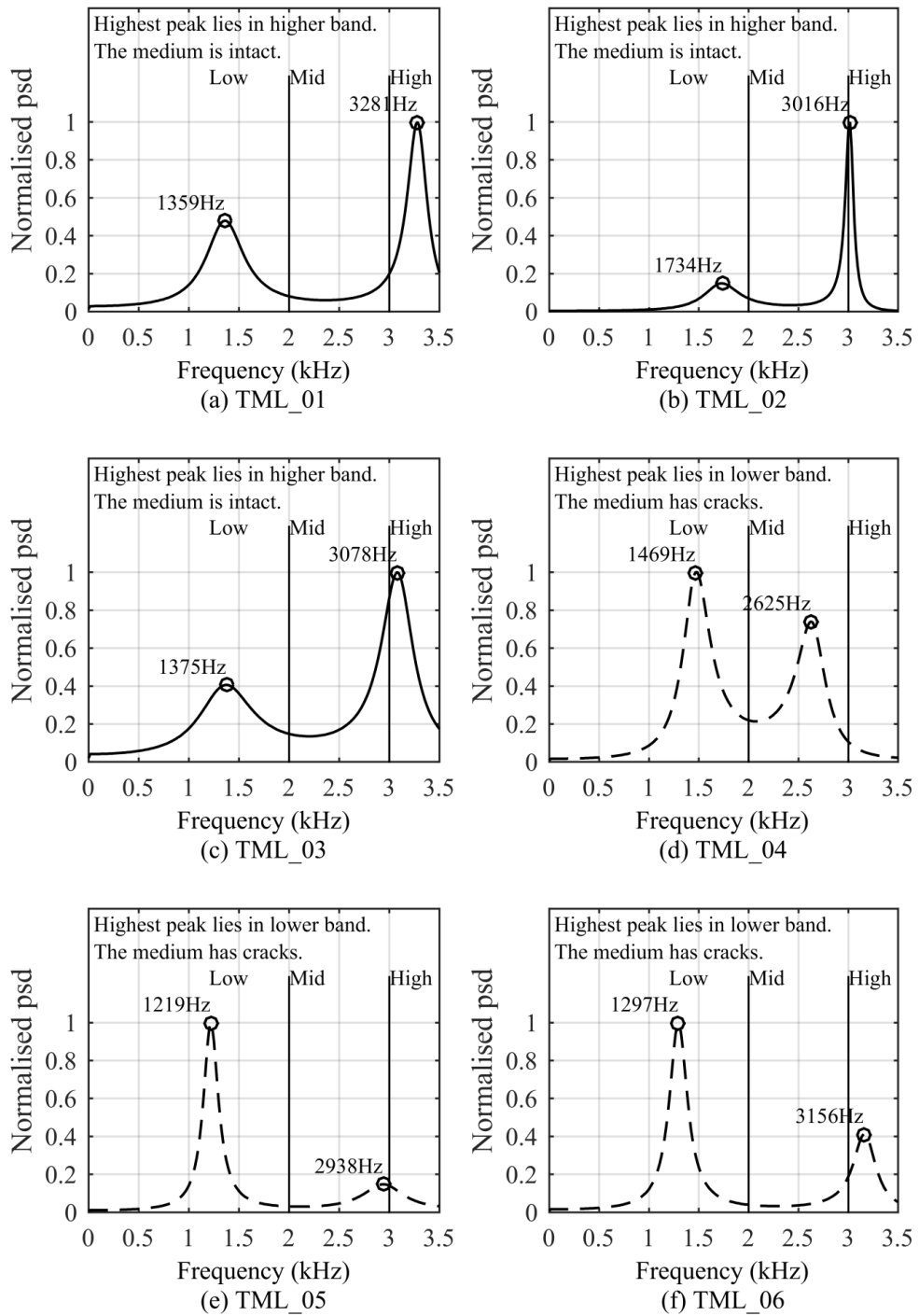


Figure 60: PSD plot showing peak locations and crack detection logic for signal 1 to 6 of stone block 3.

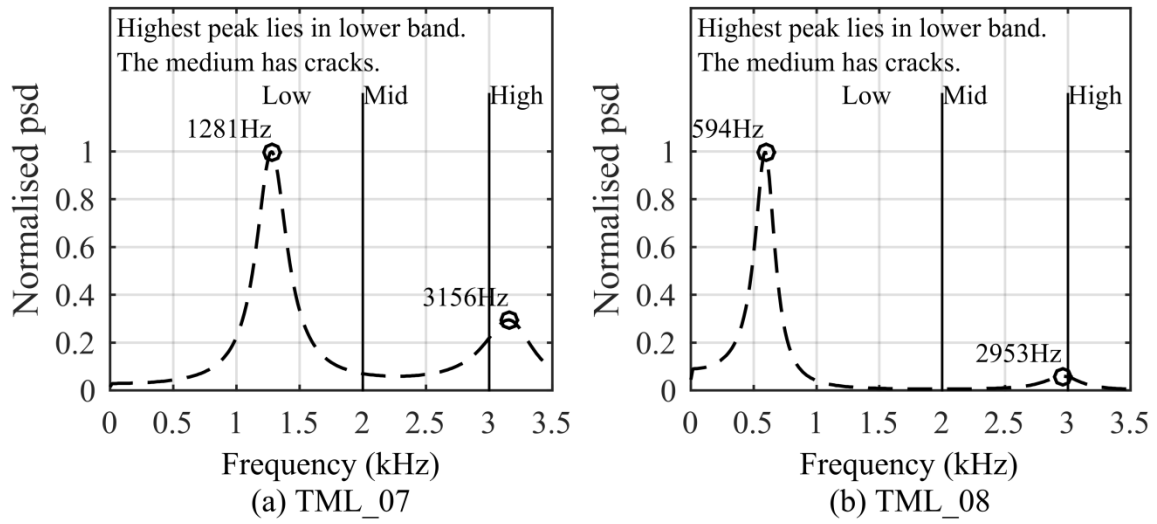


Figure 61: PSD plot showing peak locations and crack detection logic for signal 7 to 8 of stone block 3

7.1.4 Dimensional Stone Block 4 (Super White Marble, Vietnam)

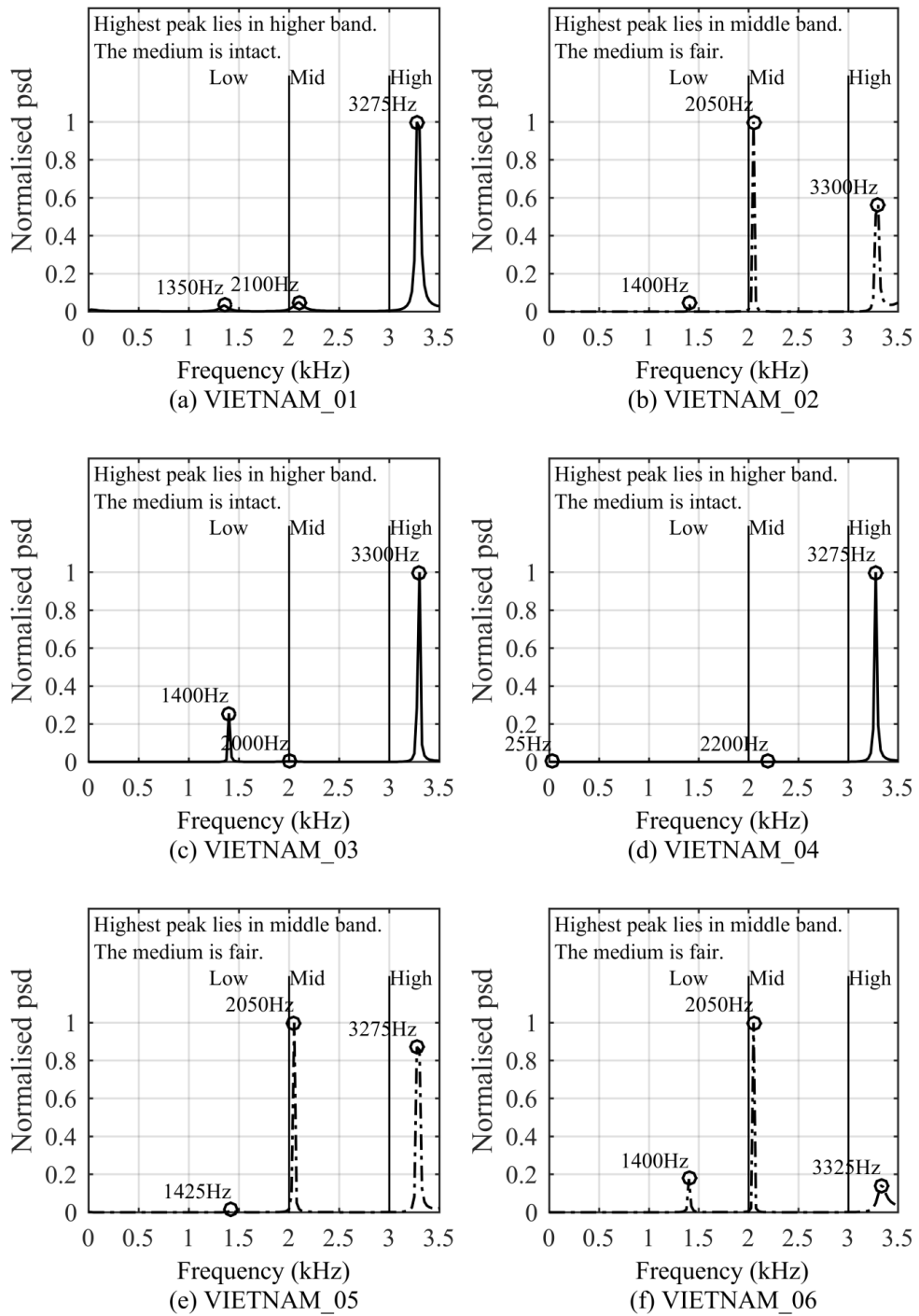


Figure 62: PSD plot showing peak locations and crack detection logic for signal 1 to 6 of stone block 4.

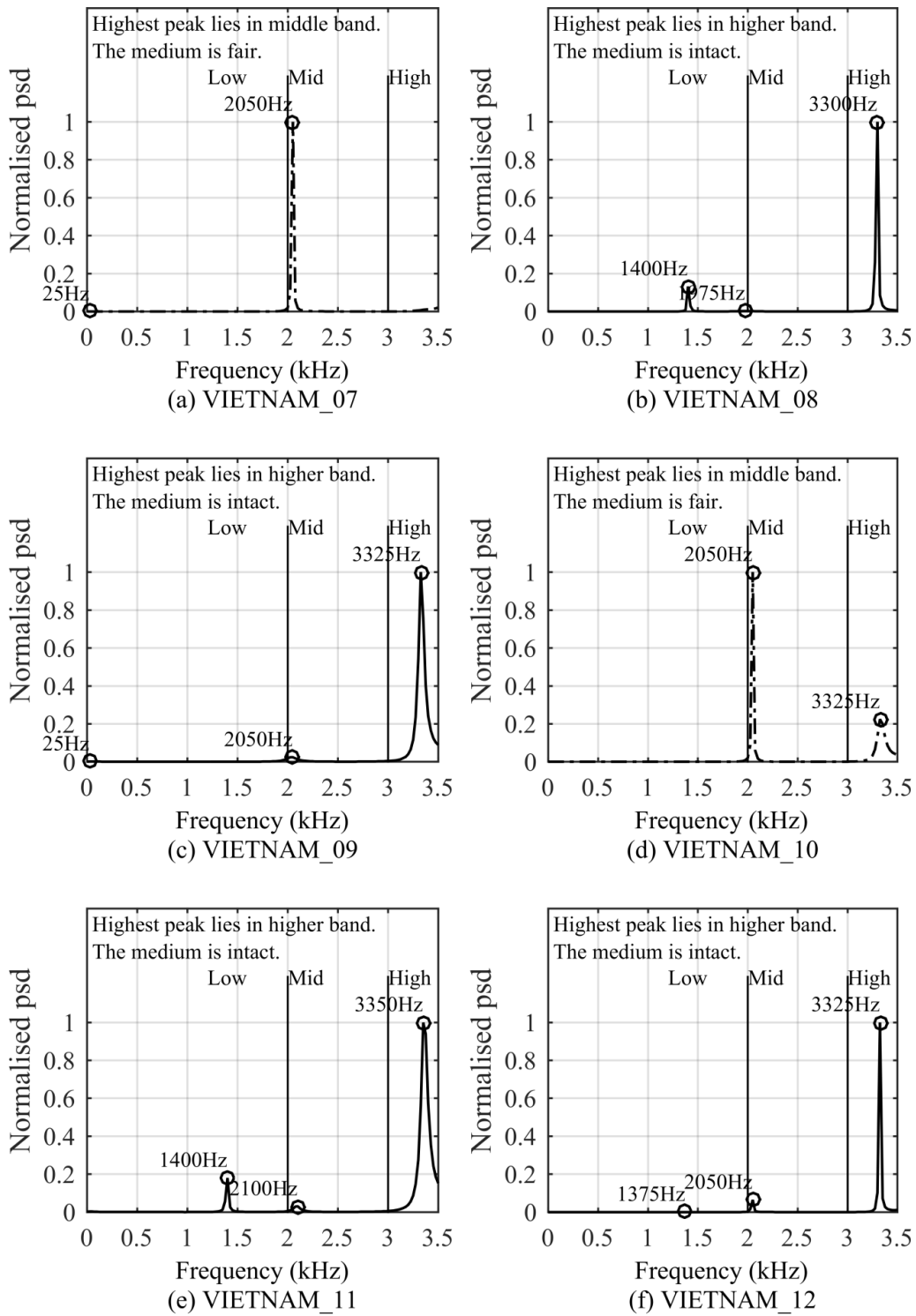


Figure 63: PSD plot showing peak locations and crack detection logic for signal 7 to 12 of stone block 4

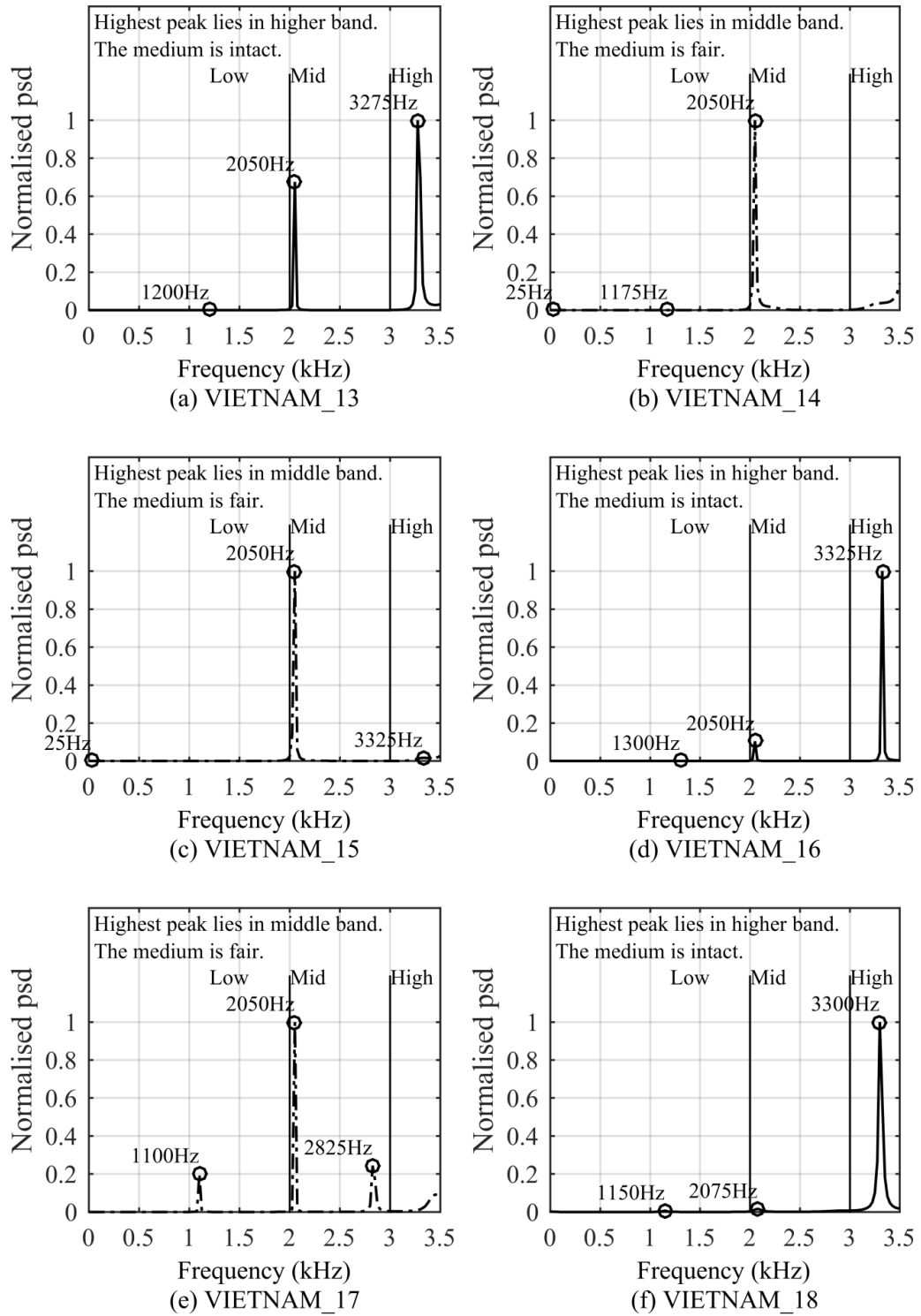


Figure 64: PSD plot showing peak locations and crack detection logic for signal 13 to 18 of stone block 4.

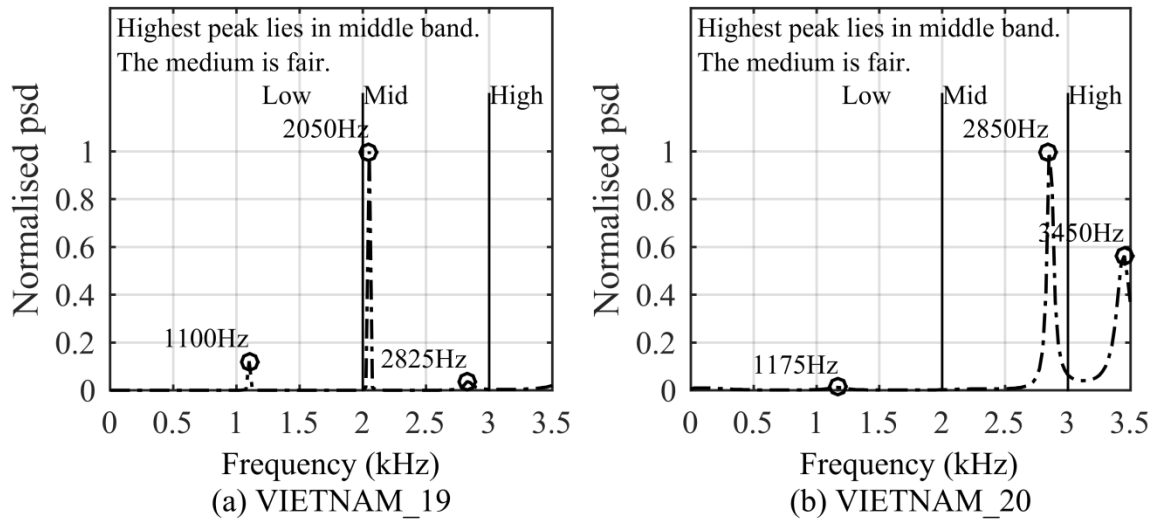


Figure 65: PSD plot showing peak locations and crack detection logic for signal 19 to 20 of stone block 4.

7.2 Mechanical Systems

7.2.1 Single Degree of Freedom System

A dynamic system can be defined as a physical entity that has an output(s), caused by input(s), and both input(s) and output(s) change with time [38].

A mass, m , is connected to a spring with stiffness, k , and viscous damper, c , as shown in Figure 66. When a dynamic force, $F(t)$ applied to the mass and the mass moves from its equilibrium position by u without any friction. The balance of applied and counteracting forces due to spring and damper on the mass is given by Newton's second law as [38]:

$$m\ddot{u} + c\dot{u} + ku = F(t) \quad (39)$$

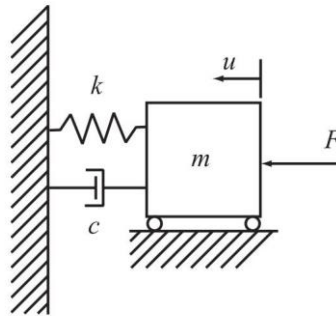


Figure 66: A mechanical system with a single degree of freedom, a mass, m , moving in one direction. The mass is connected to a spring with stiffness k and a viscous damper with damping, c [38].

7.2.1.1 Transfer Function

The transfer function of the system, $H(s)$, is calculated by applying the Laplace transform to equation (39) and given as:

$$H(s) = \frac{U(s)}{F(s)} = \frac{1/m}{s^2 + sc/m + k/m} \quad (40)$$

The equation (40) can be simplified to standard second order system equation by using the following definitions:

- $\omega_n^2 = k/m$, ω_n is the undamped natural frequency.
- $c_{cr} = 2\sqrt{km} = 2m\omega_n$, c_{cr} is the critical damping value.
- $\zeta = c / c_{cr}$, is the amount of proportional or relative damping, typically stated as a percentage of critical damping.

Rewriting equation (40), using the above substitutions:

$$H(s) = \frac{U(s)}{F(s)} = \frac{1/m}{s^2 + 2\zeta\omega_n s + \omega_n^2} \quad (41)$$

The poles of the equation (41) are given as:

$$s_{1,2} = -\zeta\omega_n \pm j\omega_n\sqrt{1-\zeta^2} = -\zeta\omega_n \pm j\omega_d \quad (42)$$

Where, $\omega_d = \omega_n\sqrt{1-\zeta^2}$, is the damped natural frequency of the system. The impulse response of the system can be written in the time domain as:

$$h(t) = Ae^{-\zeta\omega_n t} \sin(\omega_d t) \quad (43)$$

The equation (43) shows that low values of damping gives too long impulse response duration and creates higher vibrations. For a transient input pulse, the value of damping decides the duration of the response continues after the impulse excited the system [38].

7.2.1.2 Frequency Response Function

In an experimental analysis of a dynamic system, the frequency response function is calculated, which is the ratio of the spectrums of the output to the input. The equation of the frequency response can be derived from equation (41) by replacing $s = j\omega = j2\pi f$ and applying algebraic manipulation as follows [38]:

$$\begin{aligned} H(f) &= \frac{U(f)}{F(f)} = \frac{1/m}{-\omega^2 + j2\zeta\omega\omega_n + \omega_n^2} = \frac{1/m\omega^2}{\left[\left(\frac{\omega_n}{\omega}\right)^2 - 1\right] + j2\zeta\left(\frac{\omega_n}{\omega}\right)} \\ &= \frac{1/k}{1 - \left(\frac{f}{f_n}\right)^2 + j2\zeta\left(\frac{f}{f_n}\right)} \end{aligned} \quad (44)$$

The equation (44) shows that the shape of the frequency response is controlled by the ratio, ω_n/ω . When forcing frequencies, ω , is much lower than the natural frequency ($\omega_n^2 \gg \omega\omega_n \gg \omega^2$), the gain is constant, $(1/k)$ or the inverse of the stiffness with zero phase, the effect of mass and damping is minimal. At higher frequencies, ($\omega_n^2 \ll \omega\omega_n \ll \omega^2$), the gain is decreasing and has given by $1/m\omega^2$, phase is -180 degree. At resonance ($\omega = \omega_n$), i.e. when forcing and natural frequencies are same, the gain is given by $(1/k)/2\zeta$, and phase is -90 degree. The amplitude and phase plots of equations (44) are shown in Figure 67.

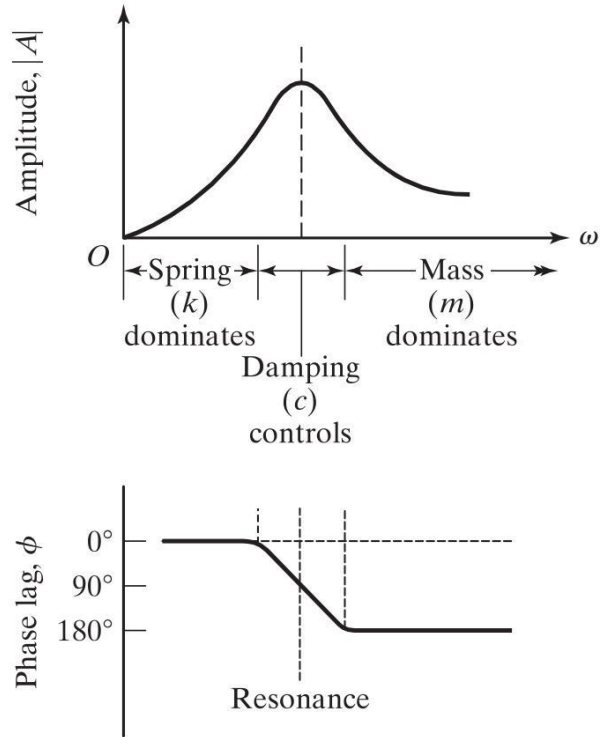


Figure 67: Frequency response function plots (Dynamic Flexibility) [80, p. 789] (a) Magnitude, (b) Phase.

Figure 68 shows the magnitude vs frequency plots for different values of damping values from 0.1 to 1.0. It shows that at the lower frequency, the magnitude is $1/k = 1.0$, whereas, at higher frequencies, it is $1/\omega^2$ with $m = 1$.

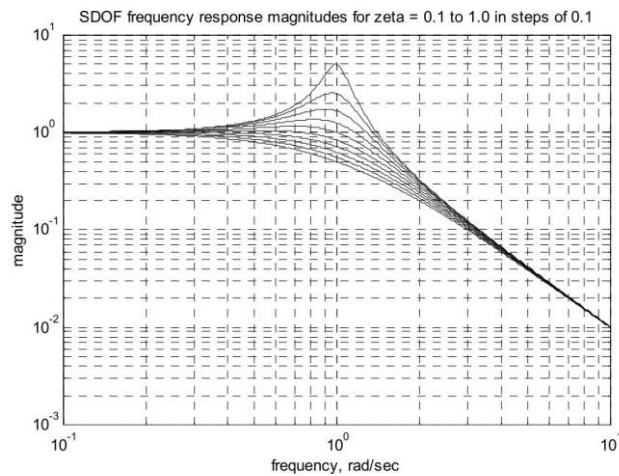


Figure 68: SDOF system, magnitude vs frequency for different damping ratios with $m = k = 1$ [81].

In the experimental model analysis, acceleration is measured instead of displacement. The frequency response function for acceleration with force is calculated from equation (44) by multiplying $(j2\pi f)^2$ [38]:

$$H_a(f) = \frac{A(f)}{F(f)} = -(2\pi f)^2 \frac{1/k}{1 - \left(\frac{f}{f_n}\right)^2 + j2\zeta \left(\frac{f}{f_n}\right)} \quad (45)$$

7.2.1.3 Determining the Natural Frequency and Damping

The physical solid system can be characterised by its natural frequencies and damping. Since the ζ is typically a small number, the magnitude at resonance will be amplified and the damped resonance frequency is given by [38]:

$$\omega_r = \omega_n \sqrt{1 - 2\zeta^2} \quad (46)$$

The half-power bandwidth or resonance bandwidth of a resonance peak is defined by [38]:

$$B_r = f_u - f_l \quad (47)$$

The lower and upper frequencies, f_l and f_u are defined, where amplitude is given by

$$|H(f_l)|^2 = |H(f_u)|^2 = \frac{1}{2} |H(f_r)|^2 \quad (48)$$

For low damping systems, the natural and damped natural frequencies are approximately same and natural frequency, f_n , the frequency where the frequency response, $|H(f)|$, has its highest amplitude. The damping factor, ζ is given as [38]:

$$\zeta = \frac{f_u^2 - f_l^2}{2f_d^2} \quad (49)$$

There will be minor variation in values of natural frequencies and damping based on selected frequency response, i.e. accelerance, mobility, or dynamic flexibility.

7.2.2 Mechanical Wave Filter

The filtering is an act of removing unwanted frequency signals from the spectrum of the signals. Technically, a filter does not remove frequencies from the input signal; it changes the relative amplitudes of the various frequency signal components and their phase relationships in the spectrum of the input signal. The change in amplitude

and phase of input signal depends on circuit components and network topology used. There are various types of filters available, e.g., low pass, high pass, bandpass, and band reject. The electrical filters are constructed using resistance, R, inductance, L, and capacitance, C elements. Every filter has a cutoff frequency(s), which defined removal of signal frequency above or below based on the type of filter. By variation of elements' values, the frequency of filtering can be changed.

The mechanical wave filters also follow the similar mathematical principle of electrical one and have identical elements to their corresponding electrical ones. An analogy can be drawn between electrical and mechanical filter characteristics and their components.

The passive electrical circuits consist of inductors, resistors, and capacitors and they have the properties of inductance, resistance, and elastance (inverse capacitance) respectively. Their mechanical counterparts are mass, stiffness and damping as shown in Table 22. The mechanical counterparts of voltage and current are a force (F) and velocity (v) respectively.

Table 22: Mechanical counterpart elements of solids to electrical elements[82].

Mechanical element	Formula (in one dimension)	Mechanical impedance	Electrical counterpart
Stiffness, k	$k = Force(F)/x$	$Z = k/j\omega$	Elastance, $1/C$, the inverse of capacitance
Mass, m	$m = F/acceleration(a)$	$Z = j\omega m$	Inductance, L
Damping, c	$c = F/velocity(v)$	$Z = c$	Resistance, R

The cutoff frequency of first order filter is given by (electrical and mechanical elements):

$$f_c = \frac{1}{2\pi} \left(\frac{1}{RC} \right) = \frac{1}{2\pi} \left(\frac{1}{\sqrt{LC}} \right) = \frac{1}{2\pi} \left(\sqrt{\frac{k}{m}} \right) \quad (50)$$

The defect changes the stiffness, mass, and damping in the solids, which impacts the filter cutoff frequency as shown by equation (50). The mass of solids has negligible effects unless defects are filled with liquid or powder. A mechanical system possesses both mass and stiffness. This translates in electrical terms to an L-C circuit,

which is, hence the mechanical system can also be treated as resonators for frequencies where inductive and capacitive impedance for a frequency match and the resonance occurs.

A low-pass filter allows the lower frequencies and attenuates higher ones. It is used for removing high-frequency noise from a signal coming from a sensor. Conversely, a high-pass filter attenuates the low frequencies and used for particular remove any DC component or low-frequency components of a signal. Band-pass filters are a combination of both, and they attenuate all frequencies below or above a given range. Lastly, a band stop filter, also called a notch filter, does the opposite of band pass, and it attenuates a selected range of frequencies. The magnitude responses of classic filters are shown in Figure 69 [83].

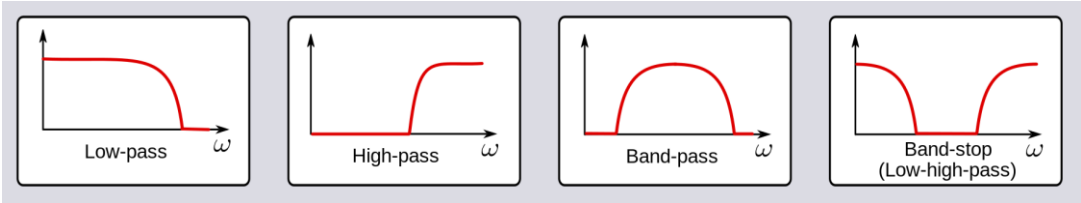


Figure 69: Typical magnitude vs frequency responses of filters of low, high, and high pass and band stop.

7.2.3 Mechanical Resonance

The resonance occurs in a mechanical system when it is forced to vibrate at a frequency nearby or one of its natural frequencies. The system has a higher amplitude of vibration when the frequency of its vibration matches to its natural frequencies than other frequencies [84]. This frequency is called resonance frequency of the system. Whenever the external forcing frequency matches to its natural frequency, the force and its response are in phase, and the response has higher amplitude compared to its neighbourhood. The anti-resonance occurs at a frequency between two resonances where the response of the system due to vibration from the lower natural frequency is out of phase with the vibration due to the higher natural frequency. The resulting vibrations then tend to cancel each other. Figure 70 shows the relation in the natural frequency, forced vibration frequency, damping, and response amplitude.

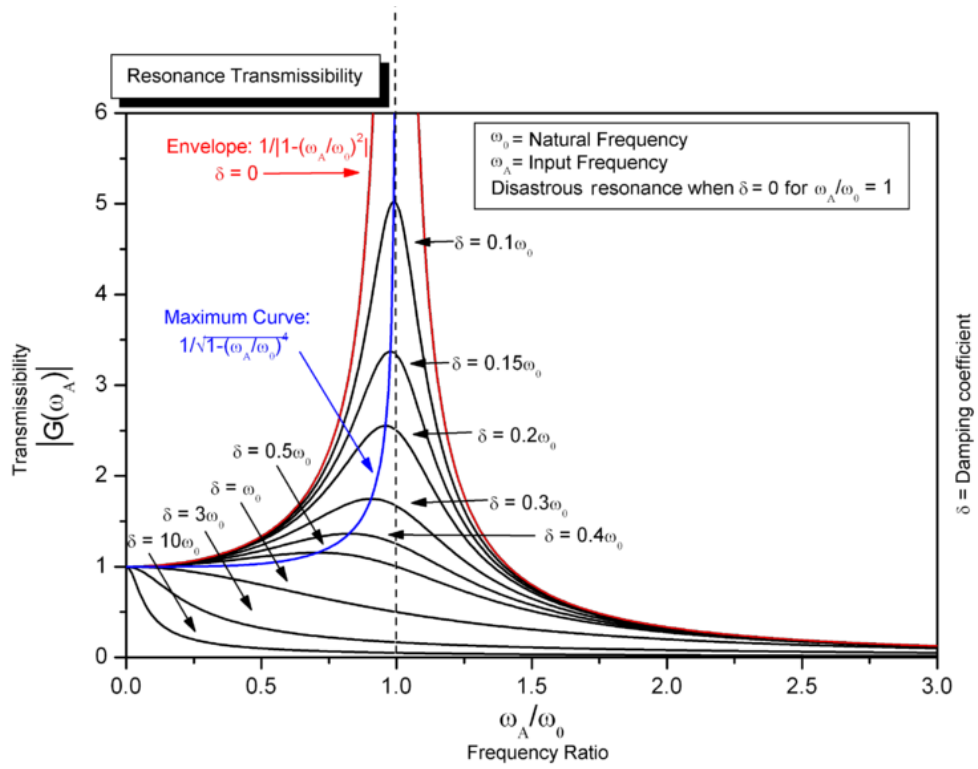


Figure 70: Mechanical resonance in a mechanical oscillatory system [84]

8. References

- [1] Wikipedia, *Stones of India - Wikipedia*. [Online] Available: <https://en.wikipedia.org/w/index.php?oldid=765463179>. Accessed on: Mar. 16 2017.
- [2] Department of Mines and Geology, “50 Years of Marble Development in Rajasthan,” Department of Mines and Geology, Rajasthan, India, Jan. 2000.
- [3] N. J. Carino, “The Impact-echo Method: An overview,” in *The Proceedings of the 2001 Structures Congress & Exposition*, 2001.
- [4] N. J. Carino, “Laboratory Study of Flaw Detection in Concrete by the Pulse-Echo Method,” *Special Publication*, vol. 82, pp. 557–580, 1984.
- [5] N. J. Carino, *Stress-Wave Methods for Flaw Detection in Concrete Structures*.
- [6] M. Sansalone, Y. Lin, N. J. Carino, D. O. Thompson, and D. E. Chimenti, “Impact-echo Response of plates Containing thin Layers and voids,” *Review of Progress in Quantitative Nondestructive Evaluation*, vol. 9, pp. 1935–1942, 1990.
- [7] V. M. Malhotra and N. J. Carino, *Handbook on Nondestructive Testing of Concrete*: CRC Press, 2004.
- [8] A. Sadri, “An Investigation of the Impact-Echo Technique,” MS Thesis, McGill University, Montreal, Quebec, Canada, 1992.
- [9] A. Bodare, *Non-destructive Test Methods of Stone and Rock*, 1996.
- [10] P. O. Moore, *Visual testing*, 3rd ed. Columbus, Ohio: American Society for Nondestructive Testing, 2010.
- [11] Industrial Applications and Chemistry Section, *Guidebook on non-destructive testing of concrete structures*. Vienna: International Atomic Energy Agency, 2002.
- [12] A. M. George, “Selecting a Nondestructive Testing Method: Visual Inspection,” *Nondestructive Examination*, 2006. [Online] Available: <http://ammtiac.alionscience.com/quarterly>.
- [13] A. A. Taddesse, “Bridge Inspection Techniques,” Oklahoma State University, 2011.
- [14] C. B. Aktas, “Determining the Thickness of Concrete Pavements using the Impact-Echo Test Method,” Middle East Technical University, 2007.
- [15] *Practice for Measuring Delaminations in Concrete Bridge Decks by Sounding*, 2012.
- [16] A. Hesse, “Using Expert Opinion to Quantify Accuracy and Reliability of Nondestructive Evaluation on Bridges,” Colorado State University, Fort Collins, Colorado, 2013.
- [17] B. D. Nicolo, C. Piga, V. Popescu, and G. Concu, “Non Invasive Acoustic Measurements for Faults Detecting in Building Materials and Structures,” in *Applied Measurement Systems*, M. Z. Haq, Ed.: InTech, 2012, pp. 259–292.
- [18] J. Arsenault and M. Chouteau, “Application of the TISAR technique to the investigations of transportation facilities and detection of utilities,” in *Geophysics*, Los Angeles, California, 2002.
- [19] C. Cheng and M. Sansalone, “The Impact-echo response of concrete plates containing delaminations numerical experimental and field studies,” *Materials and Structures*, vol. 26, pp. 274–275, 1993.

- [20] C. Hsiao, C.-c. Cheng, T. Liou, and Y. Juang, “Detecting flaws in concrete blocks using the impact-echo method,” *NDT and E International*, vol. 41, no. 2, pp. 98–107, 2008.
- [21] N. J. Carino, “Stress Wave Propagation Methods,” in *Handbook on Nondestructive Testing of Concrete*, V. M. Malhotra and N. J. Carino, Eds.: CRC Press, 2004, 14.1–14.34.
- [22] N. J. Carino, “Impact Echo: The Fundamentals,” in *International Symposium Non-Destructive Testing in Civil Engineering (NDT-CE)*, 2015.
- [23] Krautkramer J. and Krautkramer H., *Ultrasonic Testing Fundamentals*. New York: Springer-Verlag, 1969.
- [24] P. S. Piper, K. B. Le Bron, H. van Rooyen, O. D. Goldbach, and B. Clifford, “The application of acoustic techniques for identifying rock-related hazards in gold and platinum mines,” Groundwork Consulting (Pty) Ltd June, Jan. 2002.
- [25] B. M. Das and G. V. Ramana, *Principles of Soil Dynamics*: Cengage Learning, 2011.
- [26] *ASTM C597-16, Standard Test Method for Pulse Velocity Through Concrete*. West Conshohocken, PA: ASTM International, 2016.
- [27] A. H. Onur, S. Bakrac, and D. Karakus, *Ultrasonic Waves in Mining Application*: InTech, 2012.
- [28] A. Gibson, “A Time Domain Method for Accurate Non-Destructive Determination of Concrete Pavement Thickness,” Master of Science, Drexel University, 2001.
- [29] *Practice for Ultrasonic Pulse-Echo Straight-Beam Contact Testing*, 2015.
- [30] M. Sansalone and N. J. Carino, “Impact-echo: a method for flaw detection in concrete using transient stress waves,” NBSIR 86-3452, National Bureau of Standards (NTIS PB 87-104444/AS), Sep. 1986.
- [31] G. G. Clemena, “Use of the Impact-Echo Method in Nondestructive Measurements of the Thickness of New Concrete Pavements,” Virginia Transportation Research Council, Jan. 1995.
- [32] Geovision Geophysical Services, *Impact echo method*. [Online] Available: <http://www.geovision.com/impactecho.php>. Accessed on: Jul. 09 2017.
- [33] C. Colla and R. Lausch, “Influence of source frequency on impact-echo data quality for testing concrete structures,” *NDT & E International*, vol. 36, no. 4, pp. 203–213, 2003.
- [34] D. C. Abramo, “Impact-echo modeling and imaging techniques,” Masters of Science, Northeastern University, Boston, Massachusetts, 2011.
- [35] Federal Highway Administration, *Nondestructive Evaluation (NDE) Web Manual: Impact Echo*. [Online] Available: https://fhwaapps.fhwa.dot.gov/ndep/DisplayTechnology.aspx?tech_id=13. Accessed on: Mar. 06 2017.
- [36] *Practice for Evaluating the Condition of Concrete Plates Using the Impulse-Response Method*, 2016.
- [37] V. M. Malhotra, “Chapter 28: Nondestructive Tests,” in *ASTM special technical publication*, 169D, *Significance of tests and properties of concrete & concrete-making materials*, J. F. Lamond and J. H. Pielert, Eds., Philadelphia, PA: ASTM, 2006, 314-336.
- [38] A. Brandt, *Noise and Vibration Analysis: Signal Analysis and Experimental Procedures*: John Wiley & Sons, Ltd, 2011.

- [39] J. T. Broch, *Mechanical Vibration and Shock Measurements*: K. Larsen & Son A/S DK-2860, 1984.
- [40] *Spectral Estimation*. [Online] Available: http://sepehri.info/afshin/projects/ADSP/SpectralEstimation/spectral_estimation.htm. Accessed on: Apr. 26 2017.
- [41] T. Al-ani, F. Cazettes, S. Palfi, and J.-P. Lefaucheur, "Automatic removal of high-amplitude stimulus artefact from neuronal signal recorded in the subthalamic nucleus," *Journal of neuroscience methods*, vol. 198, no. 1, pp. 135–146, <http://www.sciencedirect.com/science/article/pii/S0165027011001701>, 2011.
- [42] M. D. Ortigueira and J. M. Tribolet, "Global versus local minimization in least-squares AR spectral estimation," *Signal Processing*, vol. 7, no. 3, pp. 267–281, <http://www.sciencedirect.com/science/article/pii/0165168484900045>, 1984.
- [43] D. G. Manolakis, V. K. Ingle and S. M. Kogon, *Statistical and Adaptive Signal Processing*, Artech House Press, Ch.1, Ch.9, 2005.
- [44] J. G. Proakis, D. G. Manolakis, *Digital Signal Processing*, Prentice Hall, 3rd Ed., Chp.12, p.925–956, 1996.
- [45] *Periodogram power spectral density estimate - MATLAB periodogram - MathWorks India*. [Online] Available: <http://in.mathworks.com/help/signal/ref/periodogram.html>. Accessed on: Apr. 26 2017.
- [46] P. M. Djuric and Kay S. M., "Spectrum Estimation and Modeling," in *Digital Signal Processing Handbook*, Vijay K. Madisett and Douglas B. Williams, Eds., Boca Raton: CRC Press LLC, 1999.
- [47] *Parametric Methods - MATLAB & Simulink - MathWorks India*. [Online] Available: <https://in.mathworks.com/help/signal/ug/parametric-methods.html>. Accessed on: Apr. 27 2017.
- [48] Marple, S. Lawrence, *Digital Spectral Analysis*. Englewood Cliffs, NJ: Prentice Hall, Section 12.3.3, 1987.
- [49] Mohammadi, Gelareh and Shoushtari, Parisa and Ardekani, Behnam Molaei and Shamsollahi, Mohammad B, "Person identification by using AR model for EEG signals," *Proc. World Academy of Science, Engineering and Technology*, vol. 11, no. 2, 281–285, 2006.
- [50] H, Akaike, "A new look at the statistical model identification," *IEEE Trans. on Automatic Control*, vol.19, pp. 716-723, Dec. 1974.
- [51] E. Parzen, "Some recent advances in time series modeling," *IEEE Trans. on Automatic Control*, vol. 19, pp. 723-730, Dec. 1974.
- [52] J. Rissanen, "Modelling by shortest data description," *Automatica*, vol.14, pp.465-471, 1978.
- [53] G.M. Jenkins, and D. G. Watts, *Spectral Analysis and Its Applications*, Holden-Day, San Francisco, 1968.
- [54] S. M. Kay, *Modern Spectral Estimation*, Ch.7, Prentice-Hall, Englewood-Cliffs N.J., 1988.
- [55] Daniele Zonta, "Structural damage detection and localization by using vibrational measurements," Ph.D., Bologna, Gennaio, 2000.
- [56] A. Mal, S. Banerjee, and F. Ricci, "An automated damage identification technique based on vibration and wave propagation data," *PubMed*, vol. 365, no. 1851, p. 2014, 2007.

- [57] Yong Lu and Feng Gao, "A novel time-domain auto-regressive model for structural damage diagnosis," *Journal of Sound and Vibration*, no. 283, pp. 1031–1049, www.elsevier.com/locate/jsvi, 2005.
- [58] *MATLAB 2015b*. Natick, Massachusetts, United States: The MathWorks, Inc.
- [59] D. R. Hanson, "Rock stability analysis using acoustic spectroscopy," University of Michigan, Jan. 1985.
- [60] O. Dossing, "Structural Testing: Part I : Mechanical Mobility Measurements," Bruel & Kjar, 1988.
- [61] A. C. Jording, "Damage Detection in Metamorphic Stone Blocks Utilizing Impact-echo Testing and Modal Analysis," University of Nebraska Lincoln, 2012.
- [62] PCB Piezotronics, *Model 086C03 ICP Impact Hammer Installation and Operating Manual*. [Online] Available: https://www.pcb.com/contentstore/docs/PCB_Corporate/Vibration/Products/Manuals/086C03.pdf. Accessed on: Jul. 09 2017.
- [63] *Goodyear Ball Pein Hammer With Fiber Glass Handle, GY10565*. [Online] Available: http://www.amazon.in/Goodyear-Hammer-Fiber-Glass-Handle/dp/B01BSRKWRO/ref=sr_1_4?ie=UTF8&qid=1489238113&sr=8-4&keywords=ball+pein+hammer. Accessed on: Mar. 11 2017.
- [64] Guy Kulwanoski and Jeff Schnellinger, *The Principles of Piezoelectric Accelerometers*. [Online] Available: <http://www.sensormag.com/sensors/acceleration-vibration/the-principles-piezoelectric-accelerometers-1022>. Accessed on: Apr. 03 2017.
- [65] PCB Piezotronics, *Model 352C03 General purpose, ceramic shear, ICP Accelerometer Installation and Operating Manual*. [Online] Available: https://www.pcb.com/contentstore/docs/PCB_Corporate/Vibration/Products/Manuals/352C03.pdf. Accessed on: Jul. 09 2017.
- [66] Endevco Corporation, *Piezoelectric accelerometer: Model 2224C*. [Online] Available: https://buy.endevco.com/amfile/file/download/file_id/1882/product_id/1822/. Accessed on: Jul. 09 2017.
- [67] Meggitt Sensing Systems, *Accelerometer mounting and installation techniques*. Accessed on: Jun. 23 2017.
- [68] National Instruments, *NI USB-9234 User Guide and Specifications*. [Online] Available: <http://www.ni.com/pdf/manuals/372307a.pdf>. Accessed on: Jul. 09 2017.
- [69] ST Microsystems, *STM32L151VD-X - Ultra-low-power ARM Cortex-M3 MCU with 384 Kbytes Flash, 32 MHz CPU, LCD, USB, 2xOp-amp - STMicroelectronics*. [Online] Available: http://www.st.com/content/st_com/en/products/microcontrollers/stm32-32-bit-arm-cortex-mcus/stm3211-series/stm321151-152/stm321151vd-x.html. Accessed on: Mar. 27 2017.
- [70] Microchip, *MCP6L91 - Amplifiers and Linear - Linear Op Amps*. [Online] Available: <http://www.microchip.com/wwwproducts/en/MCP6L91>. Accessed on: Mar. 27 2017.
- [71] Winbond, *Winbond - Serial NOR Flash*. [Online] Available: http://www.winbond.com/hq/product/code-storage-flash-memory/serial-nor-flash/?__locale=en&partNo=W25Q64FV. Accessed on: Mar. 27 2017.
- [72] Maximum Integrated, *DS3231S#T&R Maxim Integrated | Integrated Circuits (ICs) | DigiKey*. [Online] Available: <http://www.digikey.com/product->

- detail/en/maxim-integrated/DS3231S-T-R/DS3231S-T-RCT-ND/4895454.
Accessed on: Mar. 27 2017.
- [73] Microchip, *TCN75A - Thermal Management - Temperature Sensors*. [Online] Available: <http://www.microchip.com/wwwproducts/en/tcn75a>. Accessed on: Mar. 27 2017.
- [74] DisplayTech, *64128Q / 128x64 Dot Matrix LCDs - View Our COG Graphic Display Modules Now!* [Online] Available: <http://www.displaytech-us.com/128x64-graphic-lcd-displays-q>. Accessed on: Mar. 27 2017.
- [75] *MCP73811 - Battery Management and Fuel Gauges - Battery Management and Fuel Gauges - Battery Chargers*. [Online] Available: <http://www.microchip.com/wwwproducts/en/mcp73811>. Accessed on: Mar. 27 2017.
- [76] Microchip, *MCP1825 - Power Management - Linear Regulators*. [Online] Available: <http://www.microchip.com/wwwproducts/en/mcp1825>. Accessed on: Mar. 27 2017.
- [77] *Standard Test Method for Measuring the P-Wave Speed and the Thickness of Concrete Plates Using the Impact-Echo Method*, 2004.
- [78] *Stone Defects Description - Alliance Minerals*. [Online] Available: <http://alliance-minerals.com/2013/12/stone-defects-description/>. Accessed on: Mar. 16 2017.
- [79] M. Prasad, P. Jha, S. G. Modani, and M. Singh, “Immunity of the source signature of a transient signal in flaw characterization in spectral domain,” *International Journal of Engineering Technology, Management and Applied Sciences*, vol. 5, no. 5, pp. 709–717, 2017.
- [80] S. S. Rao, *Mechanical vibrations*, 4th ed. Delhi: Dorling Kindersley, 2004.
- [81] M. R. Hatch, *Vibration Simulation Using MATLAB and ANSYS*: Chapman & Hall/CRC, 2001.
- [82] Wikipedia, *Mechanical filter - Wikipedia*. [Online] Available: <https://en.wikipedia.org/w/index.php?oldid=756968015>. Accessed on: Mar. 05 2017.
- [83] Robert Lacoste, *Analog Filter Essentials*. [Online] Available: <http://circuitcellar.com/cc-blog/analog-filter-essentials/>. Accessed on: Mar. 05 2017.
- [84] Wikipedia, *Mechanical resonance - Wikipedia*. [Online] Available: <https://en.wikipedia.org/w/index.php?oldid=775031449>. Accessed on: May 03 2017.

List of Publications

International and National Conferences

1. M. Prasad, P. C. Jha, S. G. Modani, M. Singh, “Development of an analyser for flaw characterisation in dimensional stone blocks using transient signals”, In 3rd International Conference on Research Trends in Engineering, Applied Science and Management (ICRTEISM-2017), May 28th, 2017.
2. M. Prasad, P. C. Jha, S. G. Modani, M. Singh, “Immunity of the source signature of a transient signal in flaw characterisation in spectral domain”, In 3rd International Conference on Research Trends in Engineering, Applied Science and Management (ICRTEISM-2017), May 28th, 2017.
3. M. Prasad, P. C. Jha, S. G. Modani, M. Singh, “Power spectral density estimation of dimensional stone blocks by parametric and nonparametric methods”, In International Conference on Recent Innovations in Signal-processing and Embedded-systems (RISE-2017), Oct. 27-29, 2017, *Accepted*.
4. M. Prasad, P. C. Jha, S. G. Modani, M. Singh, “Defect characterization of dimensional stone blocks using power spectral density estimation by Burg method”, In International Conference on Recent Innovations in Signal-processing and Embedded-systems (RISE-2017), Oct. 27-29, 2017, *Accepted*.

International Journals

5. M. Prasad, P. C. Jha, S. G. Modani, M. Singh, A. Singh, “Use of impulse response spectrum of a hammer's impact in flaw characterization in dimensional stone blocks”, In Sadhana, Academy Proceedings in Engineering Sciences, Springer, Communicated.

6.

Brief CV



Mahabir Prasad received the B. E. (Electrical Engineering) from Government Engineering College, Kota (currently known as University College of Engineering), Rajasthan in 1990 and M. S. (Electrical Engineering) from Indian Institute of Technology Madras in 1994. He is currently pursuing Ph.D. degree in Electronics and Communication Engineering at Malaviya National Institute of Technology, Jaipur. His areas of interest include nondestructive testing of materials, instrumentation, transducers and product development. He has served at different levels in the product development industries worldwide since 1993 and has professional experience of 24 years, which includes product development, team management and head of divisions.